IMAGING AND CHARACTERIZATION FROM THE EARTH'S CRUST TO OCEAN INFERRED FROM AUTOMATIC VELOCITY ANALYSIS AND ROCK PHYSICS APPROACHES

チャンマリー, チョン

https://doi.org/10.15017/2534445

出版情報：Kyushu University, 2019, 博士（工学）, 課程博士
バージョン：
権利関係：

IMAGING AND CHARACTERIZATION FROM THE EARTH'S CRUST TO OCEAN INFERRED FROM AUTOMATIC VELOCITY ANALYSIS AND ROCK PHYSICS APPROACHES

CHANMALY CHHUN

2019

IMAGING AND CHARACTERIZATION FROM THE EARTH'S CRUST TO OCEAN INFERRED FROM AUTOMATIC VELOCITY ANALYSIS AND ROCK PHYSICS APPROACHES

by

CHANMALY CHHUN

A dissertation submitted in partial fulfillment of requirements

for the degree of

Doctoral Engineering

Examination Committee:

Prof. Takeshi Tsuji (Chairman)

Prof. Koichiro Watanabe

Prof. Tomoaki Utsunomiya

九州大学

KYUSHU UNIVERSITY

Department of Earth Resources Engineering

Graduate School of Engineering

Kyushu University

Japan

June 2019

DEPARTMENT OF EARTH RESOURCES ENGINEERING
GRADUATE SCHOOL OF ENGINEERING
KYUSHU UNIVERSITY
Fukuoka, Japan

CERTIFICATE

The undersigned hereby certify that they have read and recommended to the Graduate School of Engineering for the acceptance of this thesis entitled, ‘‘**Imaging and characterization from the earth’s crust to ocean inferred from automatic velocity analysis and rock physics approaches**” by **Chanmaly Chhun** in partial fulfilment of the requirements for the degree of Doctor of Engineering.

Dated: August, 2019

Thesis Supervisor:

_____

Prof. Takeshi Tsuji, D.Sc.

Examining Committee:

_____

Prof. Koichiro Watanabe, D.Sc.

_____

Prof. Tomoaki Utsunomiya, Dr. Eng.

Abstract

Implementing and integrating innovative techniques such as automatic seismic velocity analysis, pre-stack waveform inversion and rock physics could break through exploration technical challenges in term of deep water and complex hydrocarbon systems in the plate convergent margin. Automatic velocity analysis in seismic data processing provided accurate and high-resolution P-wave velocity (*Vp*) structure compared to the conventional velocity analysis based on manual picking which can induce human errors, arbitrary interpretation and large uncertainty. Rock physic model allowed us to translate *Vp* into fluid saturation and pore pressure. These methodologies enhanced an exploration technique to quantify hydrate and gas resources in more accurate and high resolution, and provided insights to understand hydrate and gas formation processes, pore pressure mechanism, sedimentary processes and geo-hazards in the subsurface. Because of high-resolution velocity structure via automatic analysis, I further applied this technique to investigate and elucidate oceanographic processes resulting to thermohaline fine structure in the Kuroshio Current. This dissertation covers five chapters, and the main content in each chapter are given below:

Chapter 1 introduced the research objectives, background, and motivation. In this study, 3D seismic reflection and well data were mainly used. The integrated approach via automatic velocity analysis, pre-stack waveform inversion and rock physics were briefly described in this chapter.

In Chapter 2, the gas hydrate and free gas system in the forearc basin of the plate convergent margin was interpreted based on the seismic velocity model derived from automatic velocity analysis and rock physics models. The Kumano Forearc Basin in the Nankai Trough area, Japan,

has been known to be in complex and dynamics deformation process due to the intensive tectonism in the Nankai subduction margin. A high-resolution seismic velocity analysis to the 3D seismic data via automatic velocity picking algorithm was performed. As a result, the accurate and high-resolution *Vp* structure was obtained, which we could interpret, delineate, and quantify widespread hydrate and gas distribution in the deep water sediments. Then spatial gas hydrate and free gas saturation were converted from this high-resolution seismic velocity integrating with borehole data via rock physics approach. As a result, saturation of gas hydrate ranges from 0% to 45% in the pore volume, and highly concentrated around the outer ridge where lateral faults are densely developed. Whereas free gas saturation ranges from 0% to 20% in the pore volume, and the gas reservoir is widely distributed below the hydrate layer and highly concentrated above ridge structure. These results demonstrate that main reason for widely distributed hydrate and gas accumulation is due to dynamics gas source enrichment in the accretionary prism underlying the basin. These gases migrated upward through the complicated structures (i.e., fault, fracture, and chimney) to form widespread gas hydrate and free gas in the shallow subsurface.

In Chapter 3, pore pressure prediction was performed in the Kumano Forearc Basin. Excess pore pressure decreases effective stress and induces reservoir instability and fault reactivation; therefore, subsequent geo-hazards could occur such as submarine landslides and earthquake. In addition, pore pressure information is important for guiding the drilling program of hydrocarbon exploration/production. Pore pressure is commonly predicted from seismic velocity. However, *Vp* is influenced both by pore pressure buildup and fluid saturation, and it is difficult to separate their effects. Therefore, I used simultaneous pre-stack waveform inversion to obtain a high-resolution S-wave velocity (*Vs*) profile. Using *Vs* information, I could separately estimate high pore pressure and gas saturation effects within this basin. High pore pressure can be determined from deviating

normal compaction trend. In this study, the ratio of *Vp* and *Vs* was used to construct the normal compaction trend, although only *Vp* is commonly used for the construction of the trend. As a result, the pore pressure in the most part of forearc basin sediments is predicted as hydrostatic condition. Therefore, compressional stress and dynamic behaviors in the accretionary prism do not influence to increase in pore pressure in the overlying Kumano Forearc Basin. Based on the relationship between *Vp/Vs* and *Vp*; furthermore, I developed a method to classify (i) hydrate, (ii) gas and (iii) over pressure area.

In Chapter 4, because of cutting-edge technique via automatic velocity analysis, I applied this technique to the time-lapse multichannel seismic reflection data in the water column of the Kuroshio Current aiming to elucidate the oceanographic processes causing the thermohaline fine structures in the ocean. All reflection profiles and sound speed in the Kuroshio Current area directly derived from advanced seismic velocity processing presented a whole view of different thermohaline features variation through time and space. Sound speed profiles varied concurrently, and seismic images presented turbulent mixing, presence of internal waves, thermohaline staircases, warm/cold water vortex, and the features of deep water mass boundaries across the Kuroshio Current. The automatic sound speed analysis with the time-lapse seismic data revealed numerous ocean processes through the entire water column with high spatiotemporal resolution. Therefore, mapping time-lapse sound speed profiles in the Kuroshio Current without relying on discrete data is a great interest of probing time-variant oceanographic processes over a large-scale ocean current as well as importance for ocean-climate research.

Chapter 5 summarized the key results and findings of this research. In this study, the combining approaches via automatic velocity analysis, pre-stack waveform inversion and rock physics can provide effective and automated methods for delineating and quantifying widespread

hydrate and gas distribution. All results demonstrated and allowed us to better understand geological mechanism and processes controlling hydrate and gas occurrence in the subduction zone. The automatic velocity technique was further applied to reveal spatiotemporal reflectivity and characteristics of fine structure in the seawater of the Kuroshio Current and probe oceanographic processes influencing on ocean currents and climate systems. All approaches studied in this thesis will offer the potential solutions and advanced exploration systems for geo-resources in other plate convergent margins and environmental problem.

Table of Contents

List of Figures

List of Tables

Chapter 1

Introduction

1.1 Research objectives

In this dissertation, the combined approach of automatic velocity analysis, pre-stack waveform inversion, and rock physics model aims in:

a). revealing the widely distributed hydrate and gas reservoir in the deep water environment in the plate convergent margin, and elucidate the complex geological and formation processes and their controlling factors mainly due to intensive tectonic movement in the subduction margin.

b). quantifying the pore pressure distribution in order to understand their deformation processes and geo-hazards (i.e submarine landslide) and information for drilling programs in the foreseeable development and production of extracting natural energy resources.

c). revealing the sound speed and seismic images of thermohaline fine structure in the Ocean using automatic sound speed analysis.

1.2 Research background and motivation

Kumano forearc basin is located on a portion of the Nankai Trough where the Philippine Sea plate is subducting beneath the Japanese islands. This region lies on the seismogenic portion of a plate boundary fault or megathrust within a subduction zone which causes great earthquakes in every ~150 years (Figure 1.1). This area draws a lot of attention where a series of borehole drillings and seismic surveys have been operated. Seismic reflections show widespread of the bottom-simulating reflectors (BSRs) in the Kumano forearc basin (Figure 1.2). This basin is in deep water environment and passed through the complex sedimentation and intensive tectonic history, which provide the technical challenges in terms of complex structure, stratigraphy, unconventional resources, variable sedimentation, diagenesis, and unloading due to basin uplift and configuration change (Saffer et al., 2009; Expedition 314 Scientists, 2009a; Tsuji et al., 2014; Moore et al., 2015). Many researches have been conducted to quantify and delineate hydrocarbon accumulations in this basin. To improve mapping of hydrate and gas concentration and pore pressure distribution with more accuracy and high resolution and better understand their connection to formation and geological processes in this basin of plate convergent margin, the combined approach was developed via automatic velocity analysis, pre-stack waveform inversion, and rock physics. This integrated technique provides a wide ranging of analytical tools, more sophisticated, faster and effectiveness to overcome all above-mentioned technical challenges.

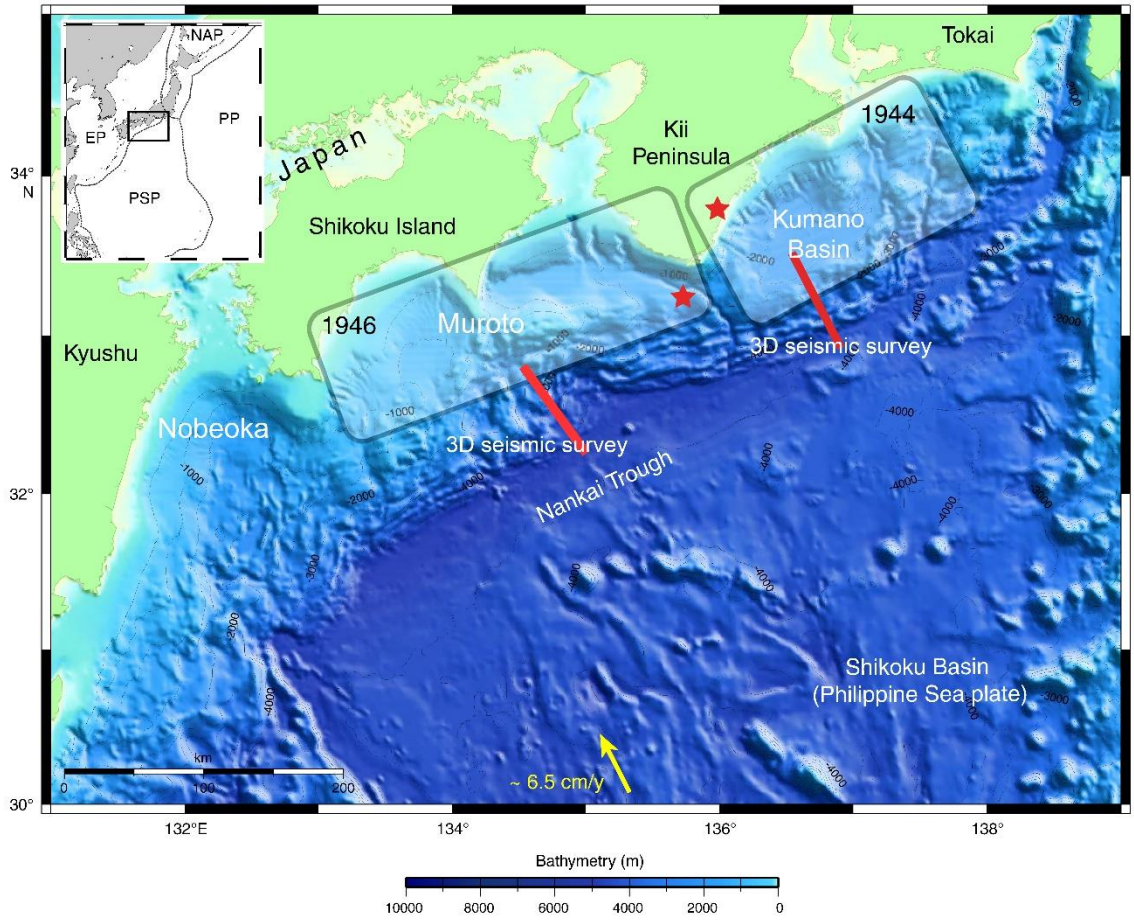

Figure 1. 1. Bathymetric map of Nankai Trough region, southwestern Japan which is the locus of the Phillipine Sea plate (PSP) beneath the Japan islands (modified from Tobin et al. 2009). Red boxes represent the 3D seismic survey in this study areas (one within Kumano forearc basin and another one within ocean column, off the Muroto transect). Yellow arrow is the convergent direction of PSP and Japan. Red stars represent epicenter locations of earthquake. EP: Eurasian Plate, PP: Pacific plate, NAP: North American plate

Automatic seismic velocity analysis is the main part of this dissertation. It is also a main part of the cutting-edge seismic data processing technique (Fomel, 2009). It is based on the normal move-out velocity analysis for determining true velocities computed from seismic data. Then these computed velocities will be used to correct and align in the traces of common-mid point (CMP) gathers before stacking. Conventionally, this method is based on manual picking which induces

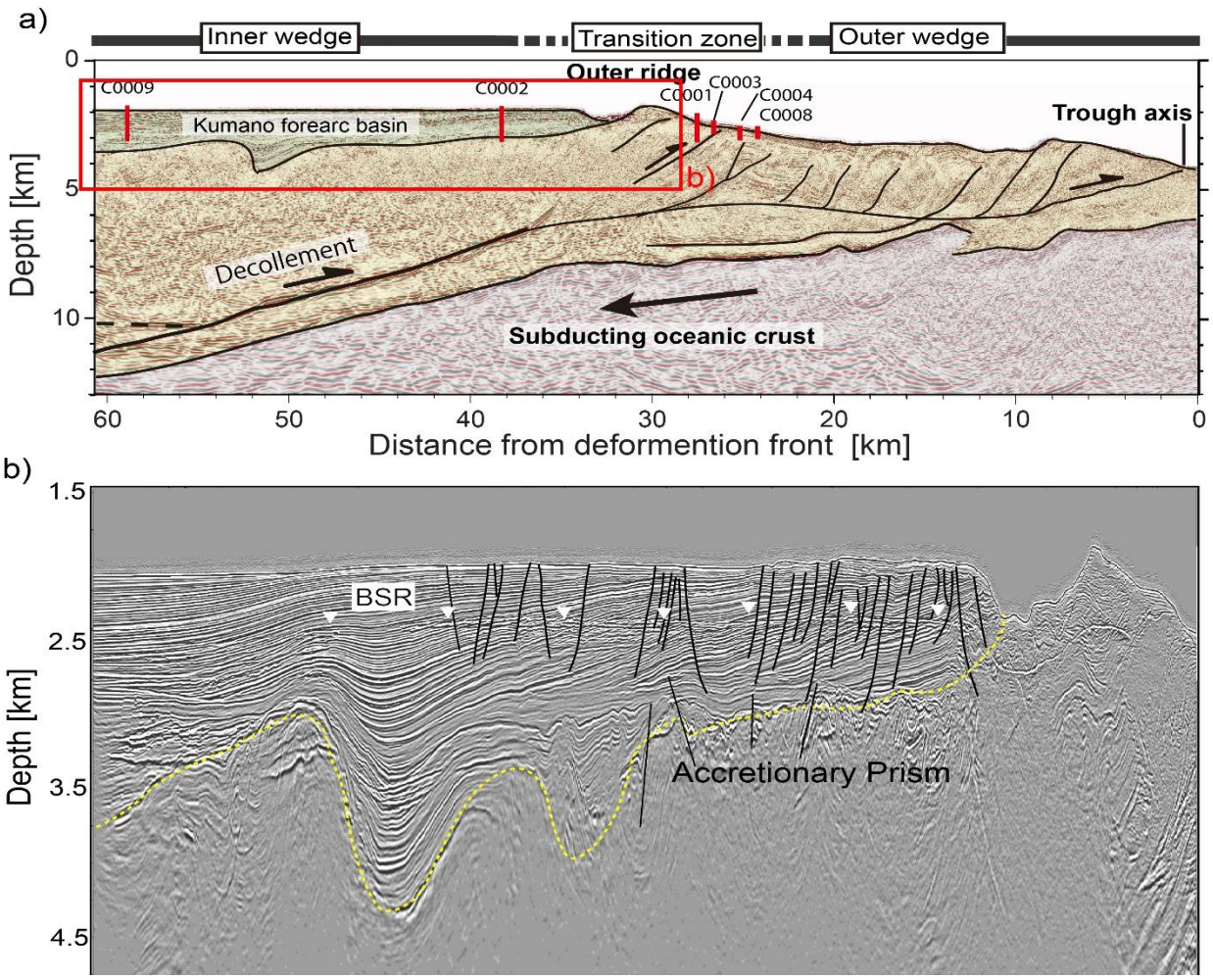

Figure 1. 2 a). The evolution stage of the deformation within the Nankai Trough and the structural cross section across the Nankai accretionary prism along the Kumano and Muroto transects (from Tsuji et al., 2015). Red box in a) is for the enlarged section in b), b). The enlarged section of red box in a). is the interval of interest in this dissertation within the Kumano Forearc basin, which represents the structure, accretionary prism beneath, and the continuous and strong amplitude marked as a bottom-simulating reflectors (BSRs) or a base of hydrate layer

error, uncertainty and time consuming process for velocity analysis. To avoid these problems, the automatic velocity analysis was developed (Fomel, 2009) which can provide high resolution and accurate seismic velocity structure (Chhun et al., 2018). This method is based on an optimal velocity trajectory solving by the eikonal equation with a finite difference algorithm (Fomel, 2009). Rock physics approach is used to turn qualitative to be quantitative domain (Tsuji et al., 2014; Jia et al., 2017; Chhun et al., 2018) in which I can use and transform high resolution seismic interval velocities into saturation and pore pressure. Additionally, seismic inversion is a technique to inverse rock physics which can derive various elastic and mechanical physical properties such as P-wave velocity (*Vp*), shear-wave velocity (*Vs*), *Vp/Vs*, P-wave impedance (*Zp*), S-wave impedance (*Zs*), and density (*Dn*) in this study (Hampson et al., 2005).

Because of innovative and effective automatic velocity analysis, I applied this technique to study thermohaline fine structure in the Ocean. Kuroshio Ocean current has been attracted the most attention from various researcher due to its characteristics of reflectivity and fine structure within the ocean column (Figure 1.3). The warm water lies above cold water in the Kuroshio Current causing double diffusive process, then this process produces thermohaline fine structure which can be mapped on seismic reflection. The ocean current and climate system are strongly influenced by the physical oceanographic processes (Sheen et al., 2012). Therefore, the imaging of the internal structure in the ocean over the large scale is a great of interest and promising tool to investigate ocean-climate system compared to traditional and conventional technique using discrete measurements.

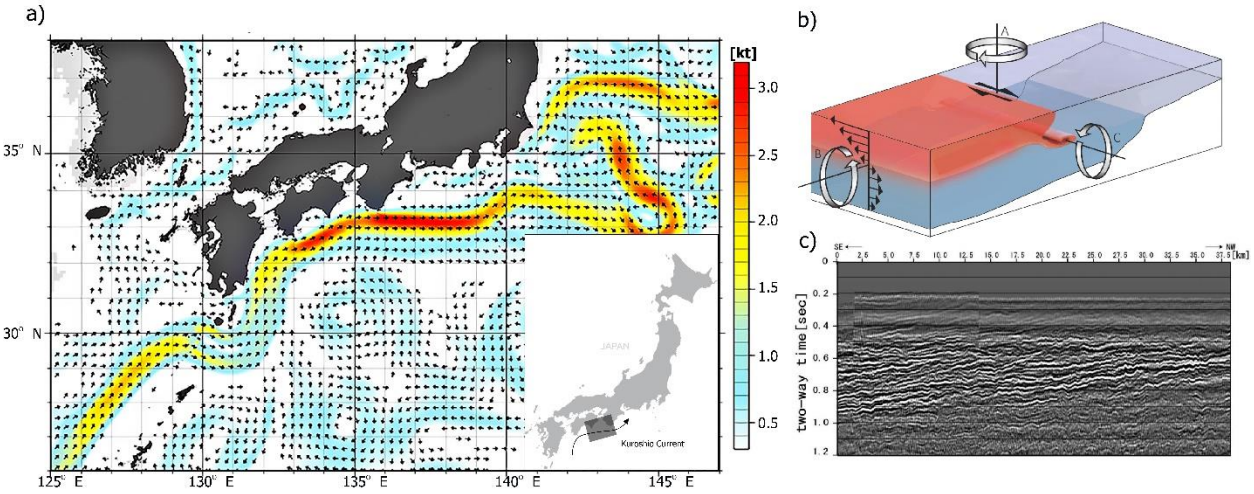

Figure 1. 3 a) surface flow map in the Kuroshio Current by 10-day mean 50m currents for 21-30 June, 1999 (unit: 1 knot ≈ 0.5 m / s, which is described as kt) (https://www.data.jma.go.jp/gmd/kaiyou/data/db/kaikyo/jun/current_HQ.html?areano=2), b) An idealized model of mixing processes between warm water (Red) and cold water (blue) creates thermohaline fine structure in the ocean (Sheen et al., 2012), c). Example of ocean thermohaline fine structure on seismic profile around the axis of Kuroshio Current off the Kii peninsula (Minato et al., 2009)

1.3 Chapter description

This dissertation consists of three main topics: high resolution velocity structure and saturation model (Chapter 2), pore pressure distribution and fluid separation effects (Chapter 3), and time-lapse study of ocean thermohaline fine structure (Chapter 4).

In *Chapter 2,* I focused on using the method of automated seismic velocity analysis to reveal never-before-seen methane hydrates and gases distributed widely in the Nankai trough, compared to previous researches. This method relied on an optimum velocity picking algorithm solving by the eikonal equation with a finite difference method. In contrast to seismic inversion, this

automatic technique resulted in a high resolution and accurate velocity structure without dependency on logging data. Moving to the next step, this high resolution velocity was converted to hydrate and gas saturation using rock physics approaches. Integration of automatic velocity analysis and rock physics approaches advanced effective and accurate resource quantification, which was beneficial for exploration techniques as well as minimizing uncertainties and risks related to upstream oil and gas activities. On the other hand, these techniques can be considered a potential solution for hydrocarbon gas quantification in the deep water reservoirs and, additionally applicable to other plate convergent margins. *The contents of this chapter was published in Marine and Petroleum geology (Chhun et al., 2018).*

In *Chapter 3,* I describe about the prediction of geo-pressure in the Kumano forearc basin. Abnormal pore pressure can be determined from deviating normal compaction trend via the velocity-to-pore pressure transform with the nearby calibration wells. Consequently, the pore pressure distribution can be quantified with the above high resolution and accurate seismic interval velocities *(Vp)* in the entire basin. However, *Vp* alone can be changed by high pore pressure and gas saturation, and these two factors can give abnormal seismic response and abnormal compacted formation. Therefore, I used the sophisticated technique of simultaneous seismic inversion to obtain high resolution shear-wave velocity *(Vs).* As a result, I can separately discuss high pore pressure and gas saturation effects, and geopressure generation mechanism related to the complex basin architecture and evolution overlying the accretionary prism in the Nankai subduction zone.

In *Chapter 4,* I applied the technique of automated velocity analysis to the time-lapse seismic reflection in order to study spatio-temporal oceanographic processes in the Kuroshio Current, Japan. As a result, this method visualized sound speed profiles of fine-scale thermohaline structure developed at interleaving or diapycnal mixing processes of different water masses in the Kuroshio

Current. All seismic images inferred from automatic velocity analysis presented thermohaline fine structure variation through time and space. The sound-speed and seismic images display turbulent mixing, the presence of internal waves, thermohaline staircases, warm and cold water vortex, and the features of deep water mass boundaries. This study is a great interest of probing oceanographic processes with their space-time resolution over large-scale ocean current as well as investigation of ocean-climate relations. *This study is submitted to Exploration Geophysics (under revision).*

In *Chapter 5,* I summarized the thesis content. The combination of automatic velocity analysis, seismic inversion and rock physics provide the insights of automatic and innovative technique to better characterize resources and structure in the earth's crust, and the time-variant internal fine structure in the ocean current useful for ocean-climate investigation.

1.4 References

Cerchiari, A., Fukuchi, R., Gao, B., Hsiung, K.H., Jaeger, D., Kaneki, S., Keller, J., Kimura, G., Kuo, S.T., Lymer, G., Maison, T., Motohashi, G., Regalla, C., Singleton, D., Yabe, S., 2018. IODP workshop: Core-Log Seismic Investigation at Sea - Integrating legacy data to address outstanding research questions in the Nankai Trough Seismogenic Zone Experiment. Sci. Drill. 24, 93–107. https://doi.org/10.5194/sd-24-93-2018

Chhun, C., Kioka, A., Jia, J., Tsuji, T., 2018. Characterization of hydrate and gas reservoirs in plate convergent margin by applying rock physics to high-resolution seismic velocity model. Mar. Pet. Geol. 92, 719–732. https://doi.org/10.1016/j.marpetgeo.2017.12.002

Expedition 315 Scientists, 2009. Expedition 315 Site C0002. In: Kinoshita, M., Tobin, H., Ashi, J., Kimura, G., Lallemant, S., Screaton, E.J., Curewitz, D., Masago, H., Moe, K.T., the Expedition 314/315/316 Scientists (Eds.), Proceedings of the Integrated Ocean Drilling Program, 314/315/316. Integrated Ocean Drilling Program Management International, Inc., pp. 1–76.

Fomel, S., 2009. Velocity analysis using AB semblance. Geophys. Prospect. 57, 311–321. https://doi.org/10.1111/j.1365-2478.2008.00741.x

Hampson, D.P., Russell, B.H., Bankhead, B., 2005. Simultaneous inversion of pre-stack seismic data 1633–1637. https://doi.org/10.1190/1.2148008

Ito, T., Komatsu, Y., Fujii, T., Suzuki, K., Egawa, K., Nakatsuka, Y., Konno, Y., Yoneda, J., Jin, Y., Kida, M., Nagao, J., Minagawa, H., 2015. Lithological features of hydrate-bearing sediments and their relationship with gas hydrate saturation in the eastern Nankai Trough, Japan. Mar. Pet. Geol. 66, 368–378. https://doi.org/10.1016/j.marpetgeo.2015.02.022

Jia, J., Tsuji, T., Matsuoka, T., 2017. Gas hydrate saturation and distribution in the Kumano Forearc Basin of the Nankai Trough. Explor. Geophys. 48, 137–150. https://doi.org/10.1071/EG15127

Minato, S., Tsuji, T., Noguchi, T., Shiraishi, K., Matsuoka, T., Fukao, Y., and Moore, G., 2009.

Estimation of detailed temperature distribution of sea water using seismic oceanography, Butsuri-tansa, 62, 509-520 (Japanese with English abstract). https://doi.org/10.3124/segj.62.509

Moore, G.F., Boston, B.B., Strasser, M., Underwood, M.B., Ratliff, R.A., 2015. Evolution of tectono-sedimentary systems in the Kumano basin, Nankai Trough forearc. Mar. Pet. Geol.

67, 604–616. http://dx.doi.org/10.1016/j.marpetgeo.2015.05.032.

Saffer, D., McNeill, L., Araki, E., Byrne, T., Eguchi, N., Toczko, S., Takahashi, K., the Expedition 319 Scientists, 2009. NanTroSEIZE Stage 2: NanTroSEIZE Riser/riserless Observatory. Integrated Ocean Drilling Program Expedition 319 Preliminary Report. pp. 1–83.

Sheen, K.L., White, N.J., Caulfield, C.P., Hobbs, R.W., 2012. Seismic imaging of a large horizontal vortex at abyssal depths beneath the Sub-Antarctic Front. Nat. Geosci. 5, 542–546. https://doi.org/10.1038/ngeo1502

Tobin, H., Kinoshita, M., Ashi, J., Lallemant, S., Kimura, G., Screaton, E., Thu, M.K., Masago, H., Curewitz, D., Expeditions, I., Party, S., 2009. First Drilling Program of the Nankai Trough Seismogenic Zone Experiment. https://doi.org/10.2204/iodp.sd.8.01.2009

Tsuji, T., Kamei, R., Pratt, R.G., 2014. Pore pressure distribution of a mega-splay fault system in the Nankai trough subduction zone: Insight into up-dip extent of the seismogenic zone. Earth Planet. Sci. Lett. 396, 165–178. https://doi.org/10.1016/j.epsl.2014.04.011

Chapter 2

Characterization of hydrate and gas reservoirs in plate convergent margin by applying rock physics to high-resolution seismic velocity model

Abstract

Gas hydrates are widely distributed in the Kumano forearc basin, which is located above accretionary prism in the Nankai margin off the Kii peninsula, Japan. Bottom-Simulating Reflector (BSR) at the base of gas hydrate stability zone has been imaged as a strong acoustic impedance contrast on the reflection seismic profiles. In order to better define the accumulations of gas hydrates and free gases, a high-resolution seismic velocity analysis to 3D seismic data using a method of conventional semblance spectra via automatic velocity picking algorithm were

performed. The results revealed that gas hydrate-bearing sediments above the BSR and free gas-bearing sediments below the BSR are characterized by P-wave velocities of 1,900-2,500 m/s and 1,000-1,800 m/s, respectively. Then, the velocity model was converted into gas hydrate and free gas saturation using rock physics approaches. The results indicated that saturation of gas hydrates ranges from 0% to 45% in the pore space, and highly concentrated around the outer ridge where faults are densely developed. Additionally, concentrations of free gas ranging from 0% to 20% in the pore space are widely distributed below BSRs and are considerably high above ridge structure generated by displacement of large fault splayed from the deep plate boundary décollement. Based on these results, it is suggested that the gas hydrates concentrated due to the free gas influx which migrated upward through the steeply dipping strata and faults (or fractures) cutting through the basin. The accumulations of gas and/or hydrates are further controlled by fault movements in the accretionary prism beneath the forearc basin. Therefore, these factors generated by intensive tectonic movements in the plate subduction zone control the distribution and saturation pattern of gas hydrate and free gas formations.

Keywords: Gas hydrate saturation; Free gas saturation; Automatic velocity analysis; Rock physics; Nankai Trough; Forearc basin; Fault activity

2.1 Introduction

Gas Hydrate is crystalline solids like ice bonding both water and gas molecules. In gas hydrate, mainly methane is trapped within water molecules forming as a rigid lattice cages. They occur in the permafrost region and deep water sediments where are high pressure and low temperature condition (Kvenvolden, 1993; Sloan and Koh, 2007). Significant amount of hydrocarbon clogged in the hydrate phase represents the unconventional and potential energy resources (Milkov, 2004). One cubic foot of gas hydrate approximately yields 163 cubic feet of gas (Hardage and Roberts, 2006). The gas hydrates contribute to global climate change and potential drilling hazards (Ruppel and Kessler, 2017; Kretschmer et al., 2015; Hovland et al., 2001). Furthermore, the destabilized gas hydrate seepage in marine sediments could cause geologic hazards such as submarine slumps and induced earthquakes (Xu and Germanovich, 2006; Kvenvolden, 1993; Sloan and Koh, 2007; Waite et al., 2009). Therefore, characterization of hydrocarbon reservoirs is also crucial to predict future climate change and geohazards.

The methane hydrate is widely distributed in the forearc basin of the plate convergent margins. Kumano forearc basin is located to the southeast of the Kii Peninsula, Japan, overlying the accretionary prism in the Nankai Trough where the Philippine Sea plate is subducting beneath the Japanese islands (Figure 2.1). Various seismic profiles show that the BSRs are widespread in this region (Ashi et al., 2002; Baba and Yamada, 2004; Matsumoto et al., 2004; Uchida et al., 2004; Jia et al., 2016). Seismic characteristics of BSR are recognized as a continuous strong reflection event with negative polarity. The presence of a BSR thus allows us to define the boundary between high velocity gas hydrate-bearing sediments and the underlying low velocity

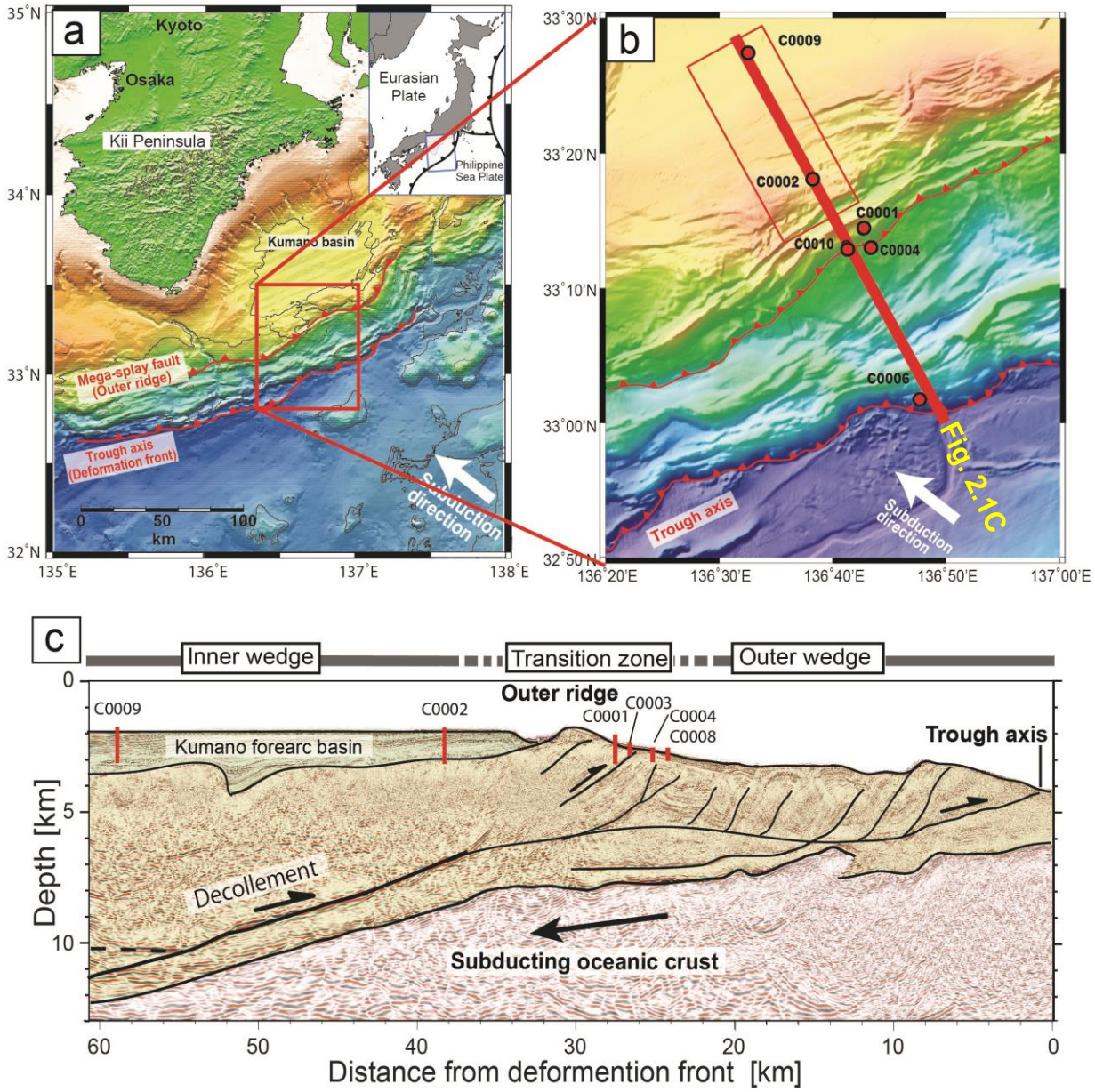

Figure 2.1 (a) The Kumano forearc basin of the Nankai Trough area. (b) An enlarged map around 3D seismic data area (Expedition 319 Scientists, 2010). Red rectangle indicates our study area (or northern part of 3D seismic area). (c) Seismic reflection profile and interpretation of the fault system in the Nankai accretionary prism (Tsuji et al., 2015). The profile location is shown in panel (b)

free gas-bearing sediments (Shipley et al., 1979; Hyndman and Spence, 1992; Vargas-Cordero et al., 2010). The estimation of total methane amount contained in gas hydrate-bearing sediments in the eastern Nankai Trough has been quantified to be 40 trillion cubic feet (Fujii et al., 2008).

There have been numerous studies on hydrate-bearing sediments in the Kumano forearc basin using several methods. For example, Miyakawa et al. (2014) studied gas hydrate saturation at Site C0002, IODP Expeditions 314 and 315, in the Kumano forearc basin of the Nankai Trough by applying Archie's equations (Archie, 1942) and a three-phase Biot-type equation on logging data; Taladay and Moore (2015) studied concentrated gas hydrate deposits in the Kumano forearc basin using the seismic attributes; Jia et al. (2016) studied gas hydrate distribution in the same region using acoustic impedance inversion for post-stack seismic data. In this study, I implemented a high-resolution seismic velocity analysis using an algorithm of automatic optimum velocity picking to effectively map gas hydrate distribution as well as gas reservoirs underneath hydrate layers in the Kumano forearc basin. With the high-resolution P-wave velocity model from the automatic seismic velocity determination, the spatially high concentration and distribution of hydrate and gas reservoirs in the Kumano forearc basin are well-defined. Many studies quantified gas hydrate saturation from acoustic impedance and water-filled porosity relations (Lu and McMechan, 2002; Wang et al., 2011); however, result from this 3D seismic velocity model can give benefits to connect this empirical relation to the P-wave seismic velocity instead of acoustic impedance inversion heavily relying on many well data. As a result, I can elucidate formation processes of hydrocarbon gas formation, accumulations and their stratigraphic, structural and tectonic control in the Kumano forearc basin of Nankai accretionary prism.

2.2 Data

2.2.1 Seismic data

Studied 3D multichannel seismic reflection data were acquired in the Nankai Trough in 2006. The coverage area is approximately 600 km^2, which is in the southern part of the Kumano forearc basin (Figure 2.1b). The 3D data acquisition geometry consists of two array source deployments, each with 28 air guns at 37.5 m shot interval. Whereas, four cables with spacing 150 m apart, each 4500 m long with 360 receiver groups at a 12.5 m gap are conducted (Moore et al., 2009). The total recording time for each shot is 12 s. The 3D seismic data volume contains inlines of 2135-2745 and crosslines of 3380-7852, and time-sampling interval of 4 ms. The vertical resolution of the seismic data was about 5–10 m for the interval of the Kumano forearc basin sequence (Moore et al., 2009). To better characterize the spatial distribution and concentration of hydrocarbon gas accumulation, common-midpoint (CMP) gathers of the data are processed with the high-resolution seismic velocity analysis using automatic picking optimum velocity algorithm (see Section "3.1 Automatic seismic velocity analysis"). Then, the resulting P-wave velocity model is obtained with high resolution, which obviously distinguishes velocities of hydrate- and gas-bearing sediments from surrounding unconsolidated sediments.

The BSRs are extensively distributed within the Kumano forearc basin sediments (Ashi et al., 2002; Baba and Yamada, 2004; Tsuji et al., 2009). Here, I analysed the 3D seismic data from crosslines of 5888-7845 and inlines of 2164-2720, which located in the southern part of the Kumano forearc basin (red rectangle in Figure 2.1b). The seafloor depth in the study area is

approximately 2,000 m. In the Kumano forearc basin, the sediments are deposited and deformed, and dipping landward which are cut by many normal faults. Numerous mud volcanoes in the Kumano forearc basin in the Nankai subduction margin have been found (Pape et al., 2014; Kuramoto et al., 2001; Morita et al., 2004), and Jia et al. (2016) identified mud volcano within the 3D seismic area. Moreover, gas sources ejecting from submarine mud volcanoes in the Nankai accretionary margin are dominantly thermogenic, and derived from old accreted sediment deeper than 2000 mbsf (meters below seafloor) (Pape et al., 2014). Therefore, 3D seismic data volume was used to characterize the spatial distribution of hydrate and gas reservoirs where no well is penetrated, and it will be crucial to predict future exploration wells for the target reservoirs.

2.2.2 Well Log data

The Kumano forearc basin was investigated by IODP drilling campaigns (Saffer et al., 2009; Expedition 314 Scientists, 2009a; Expedition 319 scientists, 2010; Strasser et al., 2014). Two drilling sites (C0002 and C0009) penetrated in the thick sediments of the basin with the total depth of 1,401 mbsf and 1,604 mbsf, respectively (Figure 2.1b). The IODP Expedition 314 provided a suite of logging while drilling (LWD) logs, including caliper, near bit resistivity, density, gamma ray, sonic, density porosity, and neutron porosity log. Therefore, the logging data were crucially used for the *in situ* measurement of gas hydrate quantification in this study.

The site C0009 at the landward side of the Kumano forearc basin penetrated in gas zones, yet there is unavailable data for gas hydrate zone, whereas the site C0002 penetrated both in gas hydrate and free gas zones. The site C0002 is located near the trenchward (south-east) side of the

Kumano basin close to the outer ridge (Figure 2.1). The variations of mineral composition were acquired with X-ray Diffraction (XRD) analysis of the core samples (Strasser et al., 2014). These two wells were correlated and represent four main lithological units in the forearc basin. The four units of lithology are divided: Unit I (0~130 m LWD depth below seafloor (LSF)) is interpreted to be slope basin deposits, Units II (130-830 m LSF) and III (830-940 m LSF) are interpreted as thick basin fill dominated by repeating turbidite deposits. Unit III is a homogenous clay-rich interval of mudstone, overlying the top of the older accretionary prism section being as basement to the basin at 936m LSF. Unit IV (936-1401 m LSF) corresponds to the accretionary prism imaged on the seismic profiles (Expedition 314 Scientists, 2009a; Expedition 319 scientists, 2010).

2.3 Methods

I used pre-stack seismic data to obtain P-wave velocity model, then combined with logging data in order to convert velocity into hydrate and gas saturation. First, I applied automatic seismic velocity picking analysis (Fomel et al., 2013) to the pre-stack seismic data and produced the high-resolution velocity model. Second, hydrate saturation was estimated in a borehole (IODP Site C0002) in the southern Kumano forearc basin. Three methods were tested for hydrate saturation estimation using density, P-wave velocity, resistivity logs, and geologic information. They are rock physics approaches with two models (pore-filling model and matrix-supporting hydrate), and the Archie's (1942) method using resistivity log. Lastly, by using Archie's law, spatial hydrate saturation was estimated within the 3D seismic volume from obtained P-wave velocity based on log-derived relationship between P-wave velocity and porosity. Whereas spatial gas saturation

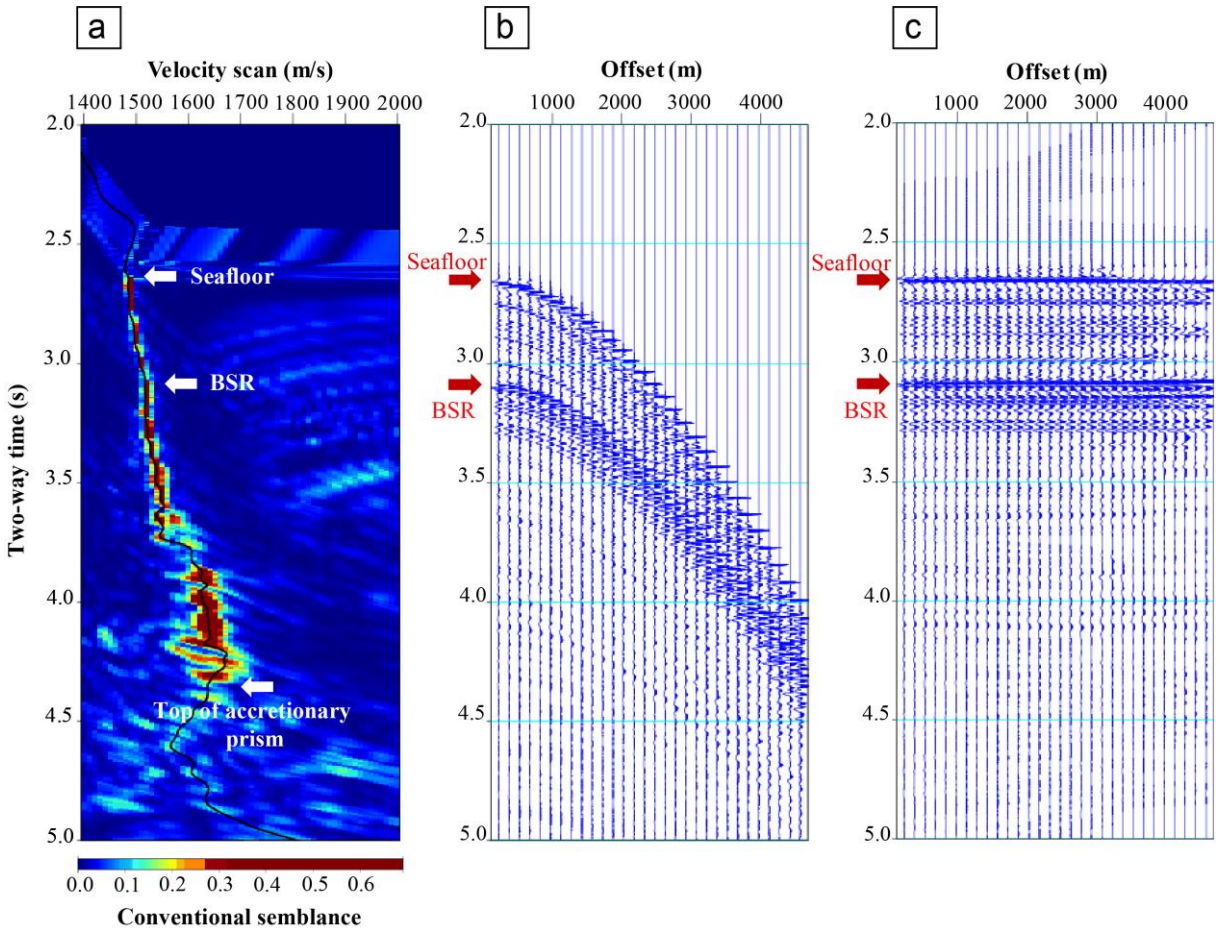

Figure 2.2 NMO-based velocity analysis. (a) Conventional semblance map via automatic velocity picks. (b) CMP gathers. (c) NMO-corrected CMP gathers

within the 3D seismic volume was estimated based on pore-filling model using only P-wave velocity as a single parameter to calculate porosity and saturation profile. The details of each method are described as the following sections.

2.3.1 Automatic seismic velocity analysis

To delineate spatial hydrocarbon gas accumulations in the Kumano forearc basin, I performed the automatic seismic velocity analysis using 3D seismic data on the part of multichannel reflection seismic lines located offshore Kumano forearc basin. Automatic seismic

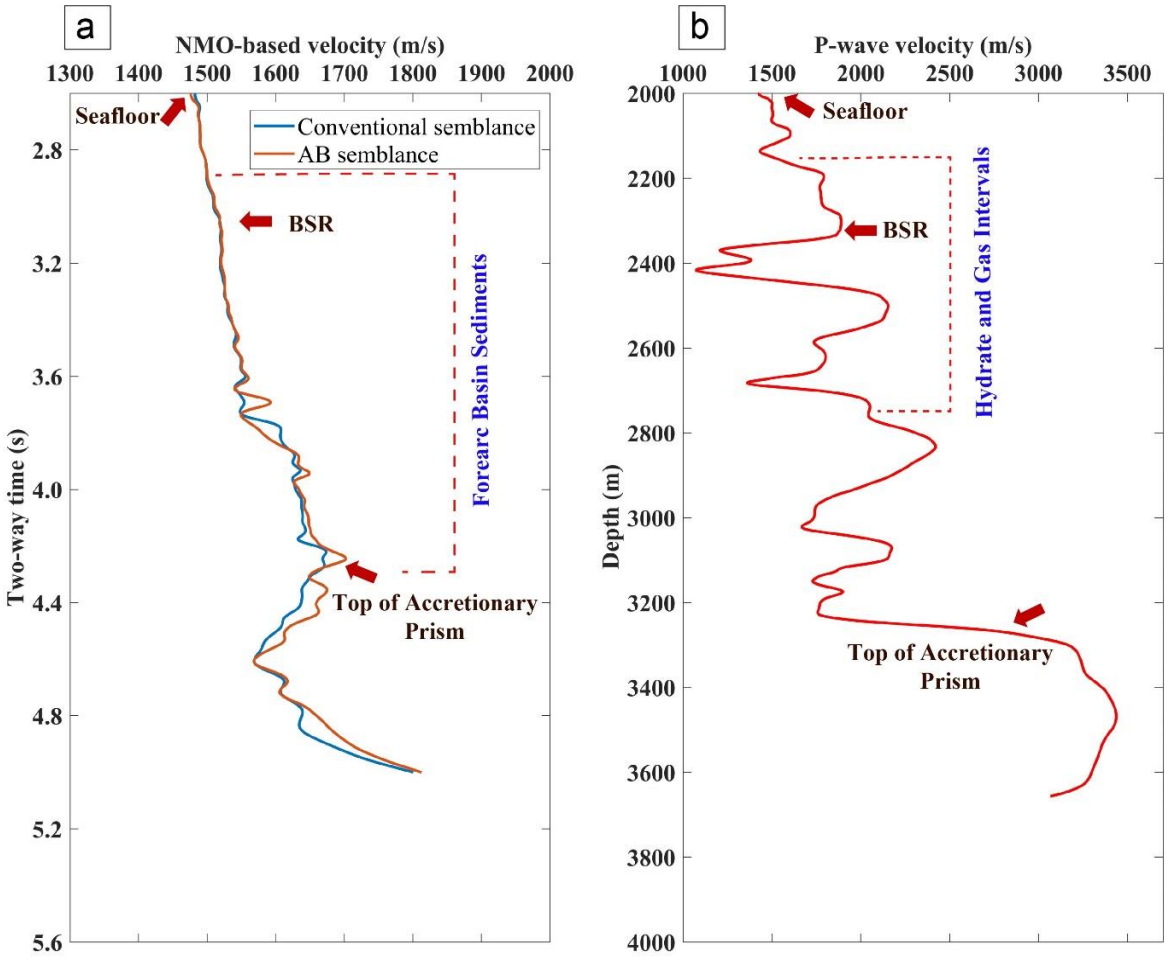

Figure 2.3 (a) NMO-based velocity (m/s) comparison between conventional and AB semblance via automatic velocity picking algorithm. (b) P-wave velocity (m/s) converted from NMO-based velocity using conventional semblance

velocity analysis computes and automatically picks stacking or root mean square (RMS) velocities from all CMP gathers of the input pre-stack 3D seismic volume. This methodology is based on an optimal velocity trajectory solving by the eikonal equation with a finite difference algorithm (Fomel, 2009). In the automatic seismic velocity picking processing workflow, I first input seismic CMP gathers to compute the conventional scanning semblance map by applying normal-moveout (NMO) based velocity analysis. I then automatically carry out interactive picking of different

reflection horizons using the velocity step in 10 m/s to pick optimum velocities with the help of shaping regularization (Fomel, 2009). The pick velocities represent vertical average (RMS) values (Figure 2.2a) of the true (interval) velocities. Computed velocities were used for NMO correction to flatten the traces of CMP gathers before stacking. All the events have been aligned and corrected demonstrating the effectiveness of velocity estimation from autopicking algorithm (Figure 2.2c). In order to make interpretation and identify gas hydrate- and free gas-bearing sediments, the NMO (or RMS) velocity was converted into interval velocity by Dix's equation (Dix, 1955). To prevent the stretching effect, lateral and vertical smoothing length were not used for data smoothening.

The seismic data for the Kumano forearc basin was high signal/noise ratio, hence I could accurately estimate seismic velocity using velocity spectrum (Figure 2.2a). The application of automatically picking velocity algorithm is effective and refrained from time consuming process, the false errors and larger velocity uncertainties caused by manual picking (Fomel and Landa, 2014) (Figure 2.2). Resulting velocity scanning map was obtained in high resolution. Owing to a less dip slope of strata (about 5 degree) and geologic structures in the Kumano sediments are incomplex, the dip-moveout (DMO) velocity analysis is not exerted in this studied area.

In accordance to seismic velocity analysis, I also evaluate the uncertainty by comparing conventional and AB semblance (=amplitude-versus-offset (avo) semblance) defined as a correlation with a trend of CMP gathers in the velocity analysis (Fomel, 2009) (Figure 2.3). Velocity analysis attribute via AB semblance is significantly applicable in the presence of strong amplitude variations and polarity reversals. The velocity estimation from AB semblance will strengthen results of hydrate amount calculation. However, the both semblances provide the same results of RMS velocity map. I assess that the uncertainty of estimated velocity between these two semblances ranges 0 to 30 m/s in the hydrate and gas intervals of Kumano forearc basin (Figure

2.3a). This can imply a more accurate result of seismic velocity estimation via either conventional or AB semblance spectrum, which were later used in hydrate and gas quantification. Underlying accretionary prism as indicated in the Figure 2.2a, the velocity estimation result is no longer accurate, mainly due to steeply dipping strata and heterogeneous structures.

2.3.2 Gas hydrate saturation from logging data at site C0002

To estimate gas hydrate saturation on logging data at site C0002, the following methods were implemented: (1) rock physics models, and (2) Archie's equations.

2.3.3 Gas hydrate saturation from sonic log based on rock physics models

I first applied theoretical rock physics models to predict the gas hydrate volume at IODP Well C0002A. The model here is applicable to the high porosity marine sediments where elastic wave velocities are related to porosity, effective pressure, mineralogy, elastic properties of the pore filling materials such as water, gas, and gas hydrate (Ecker et al., 2000; Helgerud et al., 1999). Two rock physics models for gas hydrate saturation were used: A) a pore-filling model considering that hydrate is floating in the pore fluids, and alter the elastic properties of pore fluids without affecting the frame; B) a matrix-supporting model considering that hydrate is part of the dry sediment frame, therefore altering the elasticity of the solid phase (Ecker et al., 2000; Helgerud et al., 1999; Jia et al., 2016). Input parameters for these rock physics models were obtained and

Table 2.1. Elastic moduli of each material (Ecker et al., 2000; Jia et al., 2016).

Material	K (GPa)	G (GPa)	Density (g/cm^3)
Clay	20.9	6.85	2.58
Quartz	36.0	45.0	2.65
Feldspar	37.5	15.0	2.62
Calcite	76.8	32.0	2.71
48%clay+28%Quartz+18%Feldspar+6%Calcite	29.5	15.8	2.61
Pure hydrate	5.6	2.4	0.9
Brine	2.5	0.0	1.032
Methane	0.1	0.0	0.235

calculated from geologic information (Table 1). The P-wave velocity from sonic log and porosity derived from density (Figure 2.4) were translated to the saturation profile of gas hydrates.

Model A: Pore filling model

The bulk modulus and shear modulus of the solid phase (K_m and G_m, respectively) can be calculated from the moduli of individual mineral constituents (K_i and G_i) using Hill's average:

$$K_m = \frac{1}{2}\left[\sum_{i=1}^{m} f_i K_i + \left(\sum_{i=1}^{m} \frac{f_i}{K_i}\right)^{-1}\right]; \quad (1)$$

$$G_m = \frac{1}{2}\left[\sum_{i=1}^{m} f_i G_i + \left(\sum_{i=1}^{m} \frac{f_i}{G_i}\right)^{-1}\right]; \quad (2)$$

where f_i is the volume fraction of the i-th component in the mineral phase, each mineral constituent is shown in the Table 1.

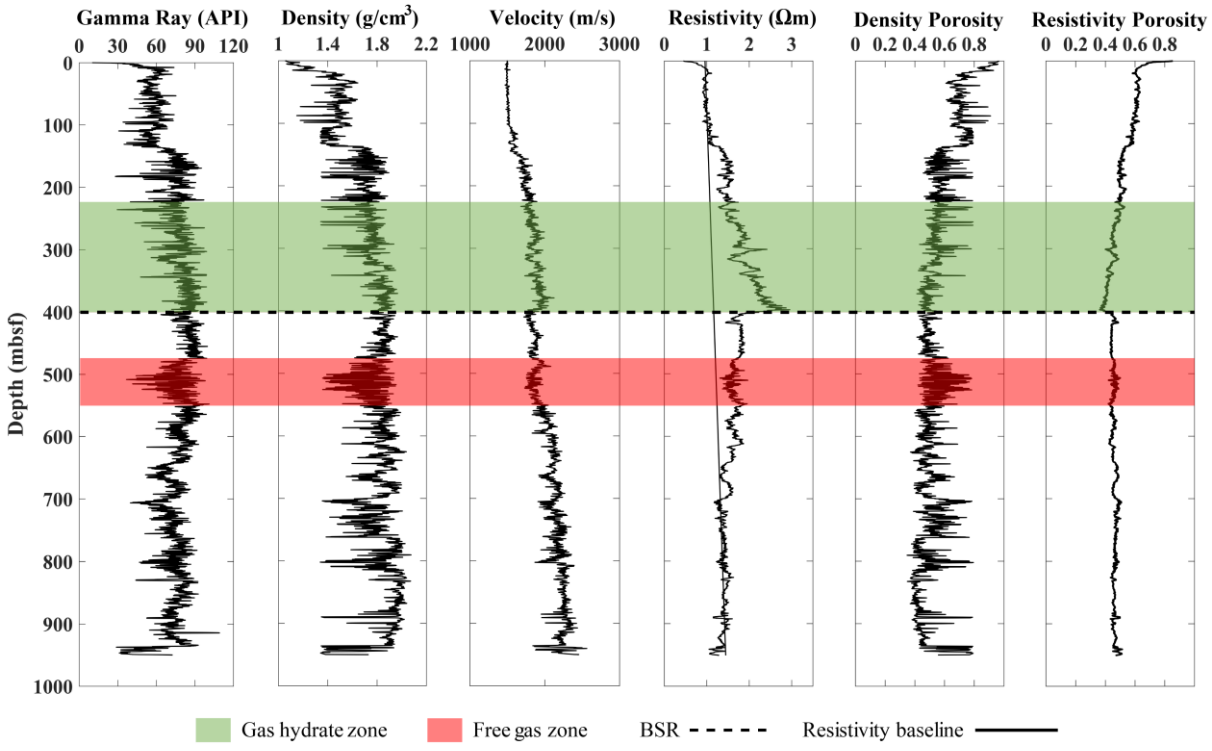

Figure 2.4 Logging data at IODP Site C0002. The gas hydrate and free gas zones are identified by green and red, respectively

The bulk and shear moduli of the dry frame of sediment without gas hydrate (K_{dry} and G_{dry}, respectively) can be obtained from the modified Hashin-Shtrikman-Hertz Mindlin theory (Dvorkin et al., 1999):

$$K_{dry} = \left[\frac{\emptyset/\emptyset_C}{K_{HM} + \frac{4}{3}G_{HM}} + \frac{1 - \emptyset/\emptyset_C}{K + \frac{4}{3}G_{HM}}\right]^{-1} - \frac{4}{3}G_{HM}; \quad \emptyset < \emptyset_C; \ (3)$$

$$G_{dry} = \left[\frac{\emptyset/\emptyset_C}{G_{HM} + Z} + \frac{1 - \emptyset/\emptyset_C}{G + Z}\right]^{-1} - Z; \quad \emptyset < \emptyset_C; \ (4)$$

$$K_{dry} = \left[\frac{(1-\emptyset)/(1-\emptyset_C)}{K_{HM}+\frac{4}{3}G_{HM}} + \frac{(\emptyset-\emptyset_C)/(1-\emptyset_C)}{\frac{4}{3}G_{HM}}\right]^{-1} - \frac{4}{3}G_{HM}; \quad \emptyset \geq \emptyset_C; (5)$$

$$G_{dry} = \left[\frac{(1-\emptyset)/(1-\emptyset_C)}{G_{HM}+Z} + \frac{(\emptyset-\emptyset_C)/(1-\emptyset_C)}{Z}\right]^{-1} - Z; \quad \emptyset \geq \emptyset_C; \ (6)$$

$$Z = \frac{G_{HM}}{6}\left[\frac{9K_{HM}+8G_{HM}}{K_{HM}+2G_{HM}}\right]; \ (7)$$

where $\emptyset$ is sediment porosity; $\emptyset_C$ is the critical porosity (0.36-0.40 according to Nur et al. (1998), $\emptyset_C = 0.36$ is used in the calculation), and K_{HM} and G_{HM} are calculated from the Hertz-Mindlin theory as:

$$K_{HM} = \left[\frac{{G_m}^2 n^2 (1-\emptyset_C)^2}{18\pi^2(1-v)^2}P\right]^{\frac{1}{3}}; (8)$$

$$G_{HM} = \frac{5-4v}{5(2-v)}\left[\frac{3{G_m}^2 n^2 (1-\emptyset_C)^2}{2\pi^2(1-v)^2}P\right]^{\frac{1}{3}}; (9)$$

$$v = \frac{3K_m - 2G_m}{6K_m + 2G_m}; (10)$$

where v is the Poisson's ratio of the solid phase calculated from K_m and G_m ; n is the average number of contacts per grain taken as 8.5 (Murphy, 1982); P is the effective pressure:

$$P = (\rho_b - \rho_w)gD; \ (11)$$

where ρ_b and ρ_w are the bulk and brine density respectively; g is gravity acceleration; and D is depth below seafloor. Then, saturated bulk modulus can be expressed as:

$$K_{sat} = K_{dry} + \frac{\left(1 - \frac{K_{dry}}{K_m}\right)^2}{\emptyset\left(\frac{S_h}{K_h} + \frac{1 - S_h}{K_w}\right) + \frac{1 - \emptyset}{K_m} - \frac{K_{dry}}{{K_m}^2}}; (12)$$

where S_h is gas hydrate saturation, which is a part of pore space, and K_h and K_w are bulk moduli of hydrate and pore water, respectively (Table 1). The saturated shear modulus G_{sat} is equal to the dry frame G_{dry} (Equation 6).

P-wave velocity of gas hydrate-bearing sediments V_p can be obtained by the following equation (Helgerud et al., 1999):

$$V_p = \sqrt{\frac{K_{sat} + \frac{4}{3}G_{sat}}{\rho_{sat}}}; (13)$$

where ρ_{sat} is the bulk density of saturated sediments, and can be calculated $\rho_{sat} = (1 - \emptyset)\rho_s + \emptyset\rho_f$ where $\rho_s = \sum_{i=1}^{m} f_i \rho_{si}$ is the bulk density of the solid phase from the value of each mineral density ρ_{si} in the Table 1, and ρ_f is the density of the pore fluid.

Model B: Matrix-supporting model

In this model, the gas hydrate is the part of solid frame, which has two effects: reducing porosity and the solid bulk and shear moduli change. The reduced porosity $\emptyset_r$ can be calculated:

$$\emptyset_r = \emptyset S_w = \emptyset(1 - S_h); (14)$$

where $\emptyset$ is the sediment porosity, and S_w and S_h are the water saturation and hydrate saturation of the pore space, respectively. Therefore the bulk and shear moduli of the solid phase are now a combination of the sediment solid and the hydrate which can be calculated from the Hill average equations (1) and (2), and f_h is the volume fraction of hydrate in the solid phase:

$$f_h = \frac{\emptyset S_h}{1 - \emptyset(1 - S_h)}; (15)$$

Then, the dry and saturated moduli can be determined using equations (3)–(13).

2.3.4 Gas hydrate saturation from resistivity log based on Archie's equations

Gas hydrate can be identified by abnormally high resistivity on logging data (Figure 2.4). Gas hydrate saturation can be expressed as a function of the ratio of water-saturated formation resistivity R_o to the measured resistivity R_t (Lu and McMechan, 2002):

$$S_h = 1 - \left(\frac{R_o}{R_t}\right)^{\frac{1}{n}}; (16)$$

where n is the saturation exponent in which hydrated clastic sediment $n = 1.9386$, (Peason et al., 1983). The resistivity of the formation fully saturated with water R_o is determined by:

$$R_o = 5.1285 \times 10^{-4} Z + 0.9592; (17)$$

where Z is the depth below the seafloor in meters. Equation (17) illustrates the baseline of the near bit resistivity shown in the Figure 2.4 fitted from well logging using the top (0-138 mbsf) and bottom (641.5-950.7 mbsf) of the dataset.

2.4 Spatial hydrate saturation from 3D seismic velocity

Jia et al., (2016) used an empirical method based on Archie's equations to estimate gas hydrate saturation via acoustic impedance. The use of Archie's (1942) equation for porosity profile determined from resistivity log is more effective than the one determined from density, neutron, and sonic log (Collett and Ladd, 2000), because resistivity log is less sensitive to the enlarged borehole condition. Therefore, it gives more accuracy for quantification of gas hydrate amount from water-filled porosity determined by Archie's equation from resistivity log (Collett and Ladd, 2000; Lu and McMechan, 2002).

From the 3D seismic velocity result, I linked this empirical method based on Archie's equations to high-P wave velocity of hydrates in order to obtain the spatial gas hydrate saturation. First of all, I determined water-filled porosity in the sediments by Archie's equation as follows:

$$\emptyset_w = \left(\alpha \frac{R_w}{R_t}\right)^{\frac{1}{\beta}}; (18)$$

where $\emptyset_w$ is the water-filled porosity in the sediments, α and β are environment-dependent empirical constants in which $\alpha = 1$ and $\beta = 2.4$ at studied IODP sites (Expedition 314 Scientists,

2009b), and R_w is the pore water resistivity, which is mainly a function of the seawater temperature and can be expressed:

$$R_w = \frac{1}{2.8 + 0.1T}; (19)$$

where T is formation temperature determined by considering seafloor temperature, and geothermal gradient based on coring data at site C0002 in the Nankai accretionary prism (Expedition 314 Scientists, 2009b; Expedition 315 Scientists, 2009).

Then, a relationship between P-wave velocity and water-filled porosity derived from Archie's equation was established (Figure 2.5). Logging data from Well C0002A were divided into three zones: a gas hydrate zone, a free gas zone and a water saturated zone. Only the zones of gas hydrate and water saturation were taken into account for the purpose of this work. I used a least squares fitting between the velocity and water saturated data in the following form:

$$\emptyset_w = \emptyset_{w\infty} + (\emptyset_{wi} - \emptyset_{w\infty}) \times \mathrm{e}^{\left(-a(V_p - V_{pi})\right)}; (20)$$

where $\emptyset_w$ is water-filled porosity, $\emptyset_{w\infty}$ is the porosity-velocity relationship at sufficiently deep depth, $\emptyset_{wi}$ is an "initial" water-filled porosity which is constrained by logging data, V_p is P-wave velocity, and V_{pi} is an "initial" P-wave velocity constrained by logging data, and a is a coefficient of exponential function.

For the water-saturated zone:

$$\emptyset_w = 0.45067 + (0.63 - 0.45067) \times e^{\left(-0.00349 \times (V_p - 1483)\right)}; (21)$$

The fitting curve of the water saturated zone shows the average difference between fitting and logging values 0.007 and standard deviation 0.014.

For the gas hydrate zone:

$$\emptyset_w = 0.32810 + (0.53 - 0.32810) \times e^{(-0.00331 \times (V_p - 1700))}; (22)$$

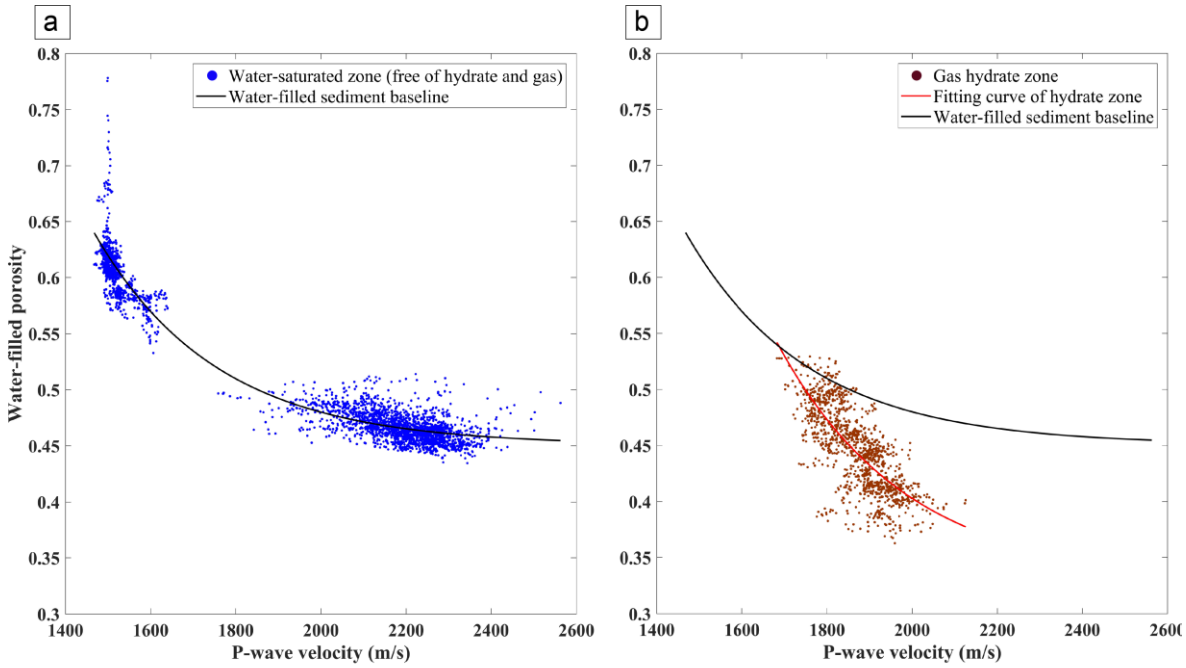

Figure 2.5 Relationship between water-filled porosity estimated from resistivity log and P-wave velocity derived from sonic log at IODP Site C0002 for (a) water-saturated zone using equation (21) and (b) gas hydrate zone using equation (22)

Average difference between fitting and logging values in the gas hydrates zone is 0.012 and standard deviation is 0.015. Water-filled porosity of gas hydrate zone is determined by Equation 22 (Figure 2.5b) presenting porosities of gas hydrates are under the full-water saturated porosity baseline from Equation 21 (Figure 2.5a). All the porosities of gas hydrates below the baseline of original porosities are indicated the hydrated areas have reduced original pore filling space in the sediments (Figure 2.5b). Gas hydrate saturation (S_h) can then be estimated by using the equation as follows:

$$S_h = 1 - \left(\frac{R_o {\emptyset_w}^{\beta}}{\alpha R_w}\right)^{\frac{1}{n}}; \quad (23)$$

The empirical relations of water-filled porosity and interval velocity from logging data (Figure 2.5b) were applied in the 3D seismic velocity model to calculate the spatial hydrate saturation. From Equation 23, I could predict spatially water-filled porosities of gas hydrate zones from 3D high velocity of hydrate zones (Equation 22). Within the hydrate area of interest, the background resistivity R_o determined from Equation 17 which is a function of depth Z, whereas the pore water resistivity R_w was calculated from Equation 19 which is a function of formation temperature. The resistivity R_w was assumed that it was not laterally variable along the hydrate region. Consequently, I am able to obtain the spatial hydrate saturation from the 3D seismic velocity model using abovementioned equations.

2.5 Spatial gas saturation from 3D seismic velocity

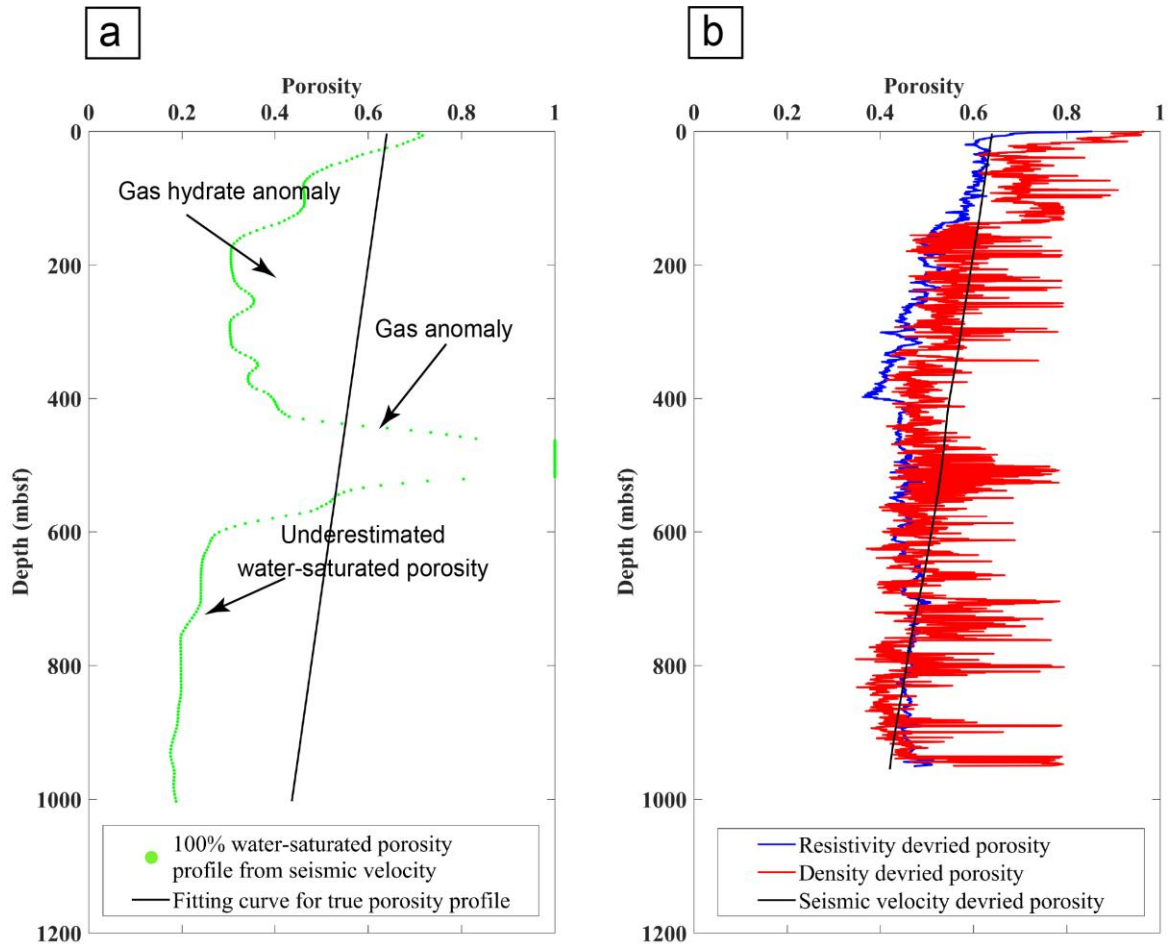

Figure 2.6 (a) Porosity profile determined from seismic velocity at Site C0002 assuming 100% water saturated sediments. (b) Comparison of porosity profiles derived from logs and seismic velocity

Seismic velocity of gas-charged sediments are dominantly slower than velocity in water column by 1000m/s different from velocity of gas-bearing sediments identified from logging data, therefore I cannot apply the same method using the empirical relationship between P-wave velocity and water-filled porosity to estimate spatial gas saturation. The amount of free gas saturation can only be determined from the seismic interval velocity obtained from the studied 3D seismic data.

I can calculate the porosity and saturation profile uniquely using a single parameter, interval velocity V_p. Vertical porosity profiles determined from interval velocity using rock physics model (see Section "Pore filling model") are under the assumption that sediments are 100% saturated by water (Ecker et al., 2000). Such porosity profile has anomalies where gas hydrate and free gas are present in terms of underestimated porosity in the hydrate sediments, and overestimated porosity in the gas-charged sediments (Green curve in Figure 2.6a). To calculate the true porosity profile (Black curve in Figure 2.6a) in the anomalous hydrocarbon zones, I fit the first order polynomial to the two parts of overlying gas hydrate and underlying free gas region (Ecker et al., 2000). I also validate this result with the porosity profiles from logging data of density-derived porosity and resistivity-derived porosity from Well C0002A (Figure 2.6b). At last, I have only one unknown parameter (i.e., saturation), which I can calculate directly from the seismic interval velocity using the rock physics model.

2.6 Results and interpretations

2.6.1 High resolution P-wave velocity

The P-wave velocity model obtained from automated seismic velocity analysis exhibits the anomalous zones of high and low velocities. The P-wave velocity of hydrate sediments above BSR at timeslice 3.0 s TWT ranges from 1900 – 2500 m/s (Figure 2.7a). The velocities of gas hydrate area are relatively high near the outer ridge of the basin. The gas reservoir beneath BSR at timeslice 3.2 s TWT is widely distributed with the P-wave velocity of 1000 – 1800 m/s (Figure 2.7b). This P-wave velocity is dominantly slower than the sound wave velocity traveling in overlying water column.

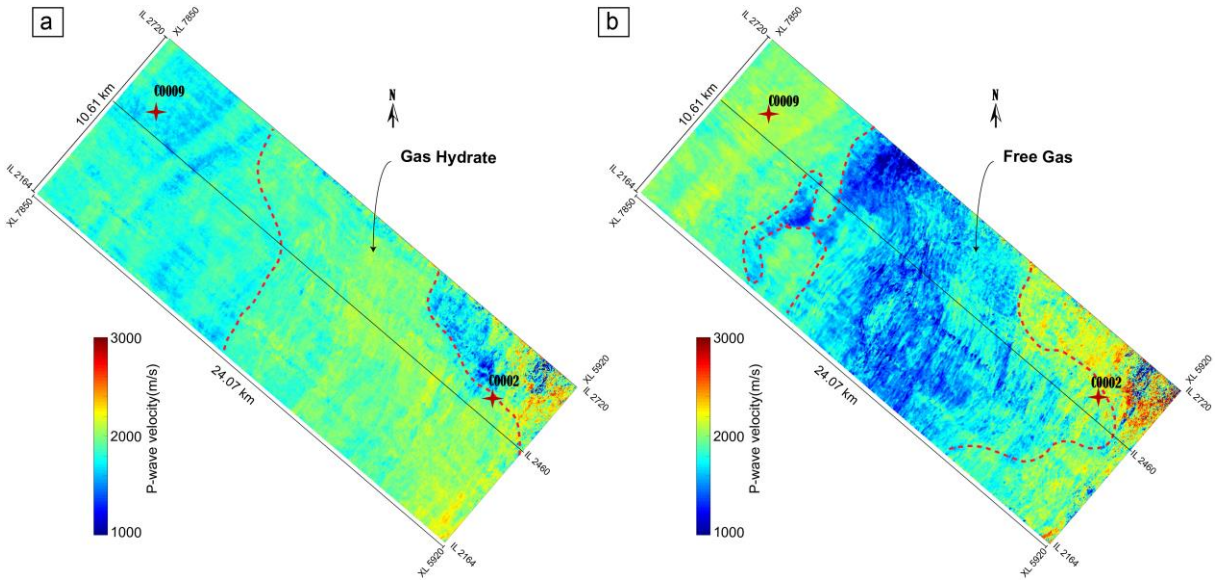

Figure 2.7 Timeslices of high-resolution P-wave velocity for (a) gas hydrate accumulated horizon at 3.0 s TWT above BSR and (b) free gas accumulated horizon at 3.2 s TWT below BSR. The red dashed lines are boundaries of velocity anomaly indicating gas hydrate and free gas

2.6.2 Seismic profiles

The post-stacked seismic profiles using high-resolution seismic interval velocity derived from automatic velocity analysis (Figure 2.8a) allow us to define the following anomalous features:

- The strong continuous amplitude event which is marked as the BSR presenting a reverse polarity compared to seafloor reflector (Figure 2.8a). Landward dipping reflectors near the outer ridge of the basin is correspondent to sediments being deformed and piled up to form an accretionary complex (Figure 2.8). Strong amplitude reflector of BSR is evident at around 3.1s TWT corresponding to 400 mbsf and it extends approximately 15 km from outer ridge

to landward side. It is noted that a strong continuous BSR clearly appears along the trenchward side of the forearc basin in the accretionary complex across the faulting system.

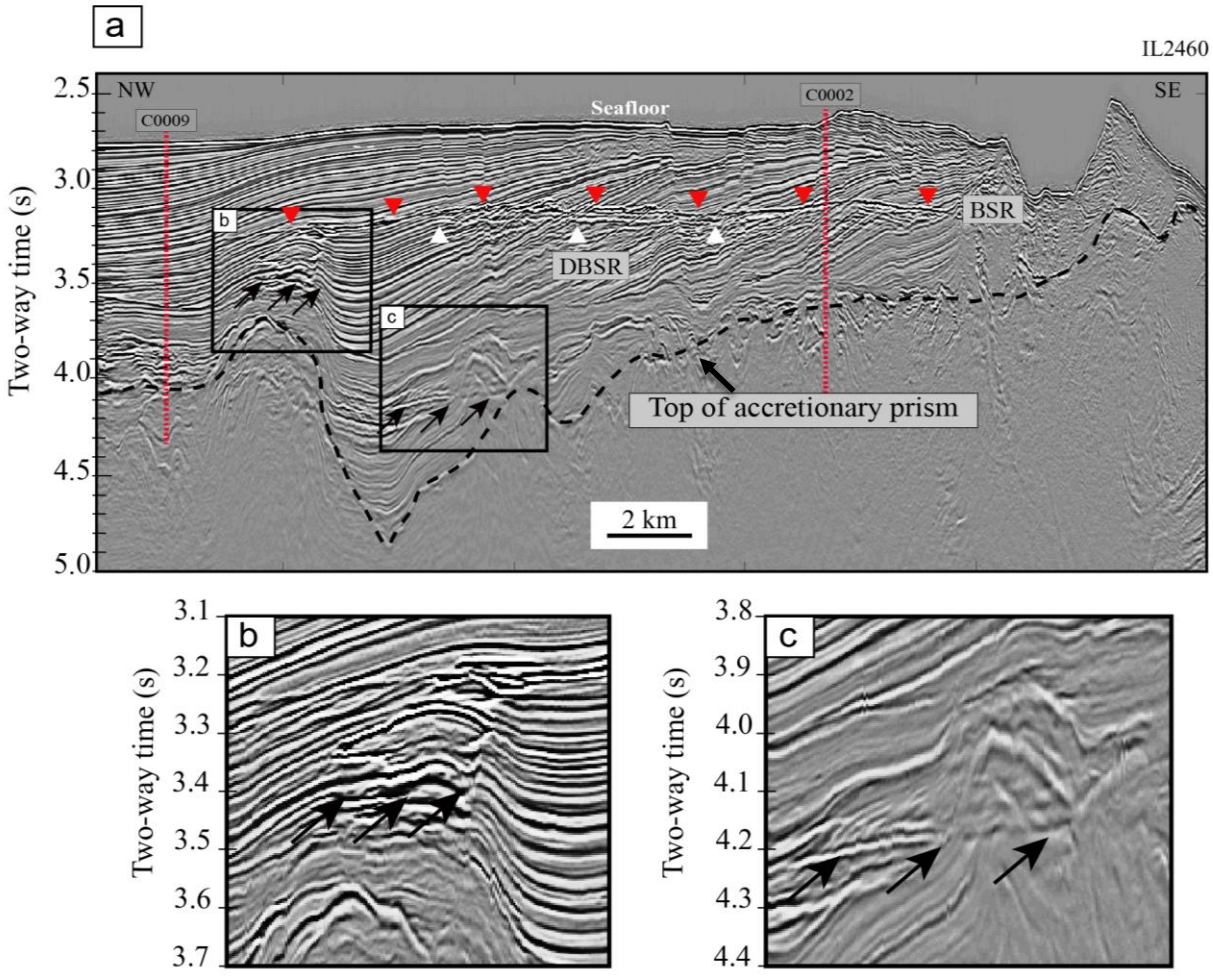

Figure 2.8 a). Seismic profile (IL2460) showing BSR (red arrowheads), double BSRs (DBSR; white arrowheads), well locations (C0009 and C0002; red lines), and flattened reflectors (black arrows). The flattened reflectors can be clearly imaged on the enlarged profiles of panels (b) and (c)

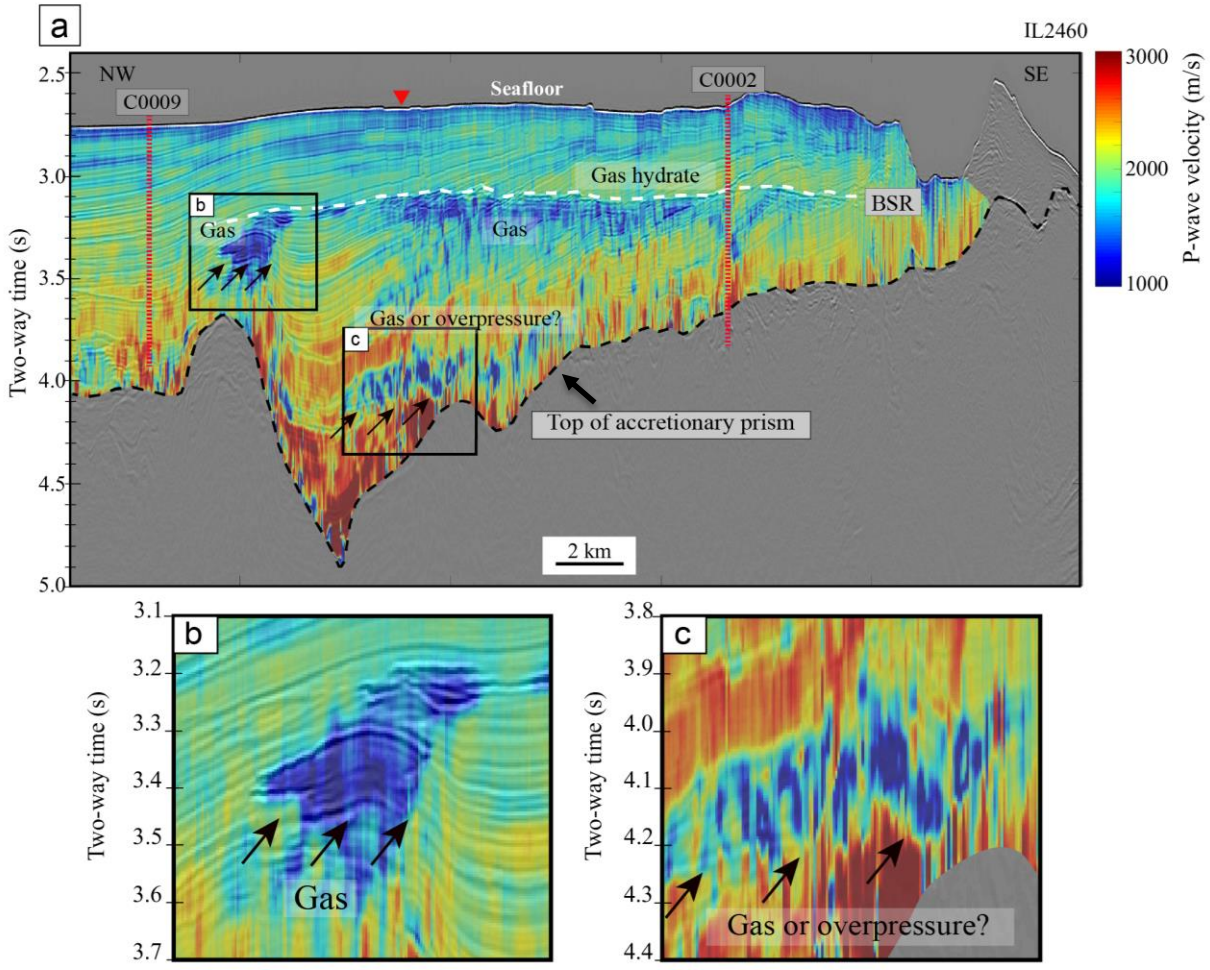

Figure 2.9 (a) Seismic velocity on IL2460 profile illustrating gas hydrate (high velocity above BSR) and gas accumulation (low velocity beneath BSR). The gas accumulation zones are clearly imaged on the enlarged profile of panels (b) and (c). Black arrows represent the base layer of gas reservoirs. Red arrowhead indicates the location of velocity shown in Fig. 2.2, Fig. 2.3.

- The BSR in some parts displays a double continuous reflection pattern (Figures 2.8a). This feature clearly appears on the profile by considering high-resolution velocity. This represents

variation in temperature and pressure when the base of gas hydrate stability field (BGHS) is in inequilibrium state (Taladay and Moore, 2015).

- The seismic profile displays two zones of flattened reflectors resulting from strong acoustic impedance contrasts which are indicators of gas-charged sediments (Figures 2.8b and 2.8c). One of the flattened reflective surfaces extending laterally are observed above the ridge topography (Figure 2.8b) correspondent to the low velocity which was interpreted as a gas reservoir (Figure 2.9b). This reservoir developed beneath the BSR extends 2 km in the horizontal direction and about 400 m in the vertical direction, and the reservoir is in an anticline structure above the ridge topography of accretionary prism (Tsuji et al., 2015). Another one is at the base of the forearc basin. It is also interpreted as a gas reservoir layer confined in the mud layer observed in a place of about 1.0 s TWT deeper than BSR depth (Figures 2.8c and 2.9c).

2.6.3 Comparison of gas hydrate saturations from all different models at Site C0002

Gas hydrate saturations from all methods show comparable patterns. The result of gas hydrate from pore-filling model shows that the trend of saturation value is higher than those from matrix-supporting model and Archie's equation model (Figure 2.10). Gas hydrate saturation estimated from Archie's equation model using the resistivity-based porosity is relatively consistent to the one from matrix-supporting model. Furthermore, saturation of gas hydrates calculated by using effective medium models including pore-filling model and matrix-supporting model, and

Archie's equation model is 0.34, 0.24 and 0.22 on average, respectively. Porosity from density log (Figure 2.4) was filtered to reduce effects caused by locally washout holes. The result from Archie's equation model (Figure 2.10) is more reliable than rock physics model using density-derived porosity because resistivity logs are insensitive to borehole conditions (Lu et McMechan, 2002;

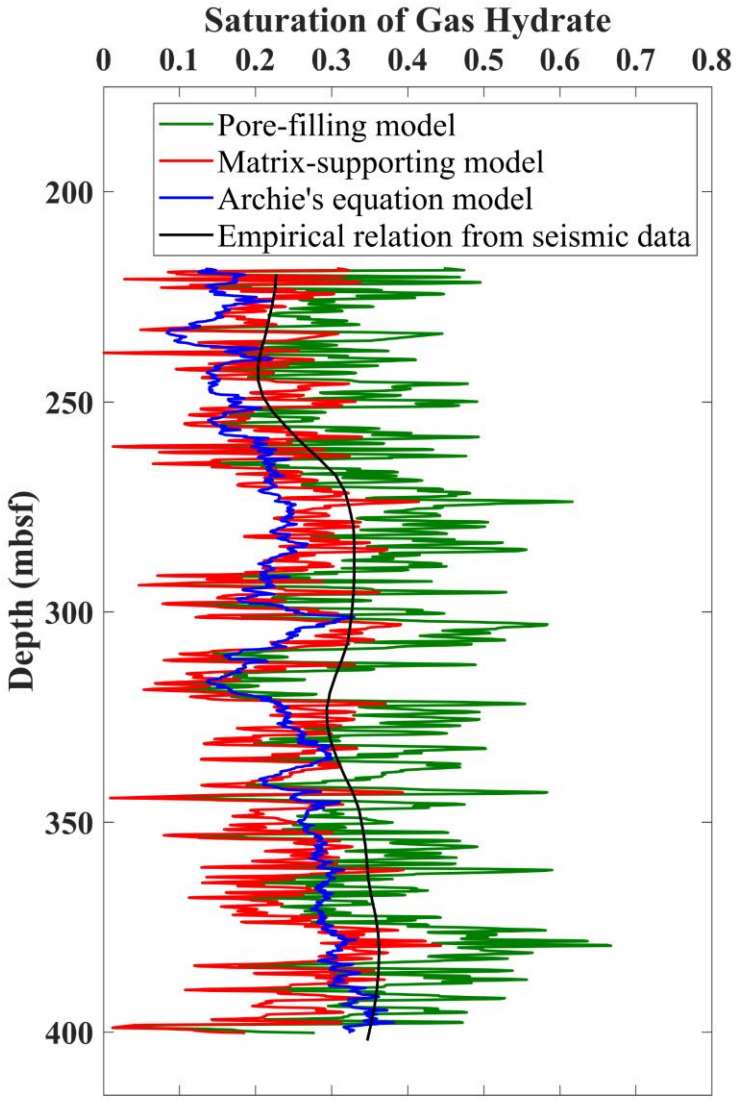

Figure 2.10 Estimations of gas hydrate saturation from pore-filling model, matrix-supporting model, Archie's equation model by using borehole logs from IODP Site C0002, and empirical relation by using seismic data

Collett and Ladd, 2000). Therefore, the consistent value of saturation from matrix-supporting model and Archie's equation model indicates that the most probable gas hydrates are attached to the mineral grains (i.e., matrix-supporting model), not floating in the pore space (Jia et al, 2016).

Thus, the empirical relationship between P-wave seismic velocity model and water-filled porosity from Archie's equations was employed for estimation of spatial gas hydrate distribution in the research area. I also validate the gas hydrate saturation profile derived from 3D seismic velocity model (i.e., empirical relation) by comparing with the saturation from logging data at the Well C0002A. The saturation from seismic velocity (0.29 on average) relatively agrees with Archie's equation model, and the trend of its saturation can be correlative to Archie's equation model (Figure 2.10).

2.6.4 Spatial gas hydrate and free gas saturation in the 3D seismic data

I used an empirical method based on Archie's equations to estimate spatial gas hydrate saturation from 3D seismic interval velocity. The results of gas hydrate saturation indicate the high variability across the study area. The spatial gas hydrate saturation above BSR at timeslice 3.0 s TWT is ranging from 0-45% in the pore space (Figure 2.11a). The high concentrations of gas hydrate are attached to the bounding fault around the rim of outer ridge and decreased toward to the landward side of the basin (Figure 2.11a).

The gas accumulation is widespread in the basin while the concentration decreases toward the trenchward outer ridge (Figures 2.9a and 2.11b), and other gas reservoirs are highly concentrated in the anticline structure above the ridge topography in the landward side (Figure 9b),

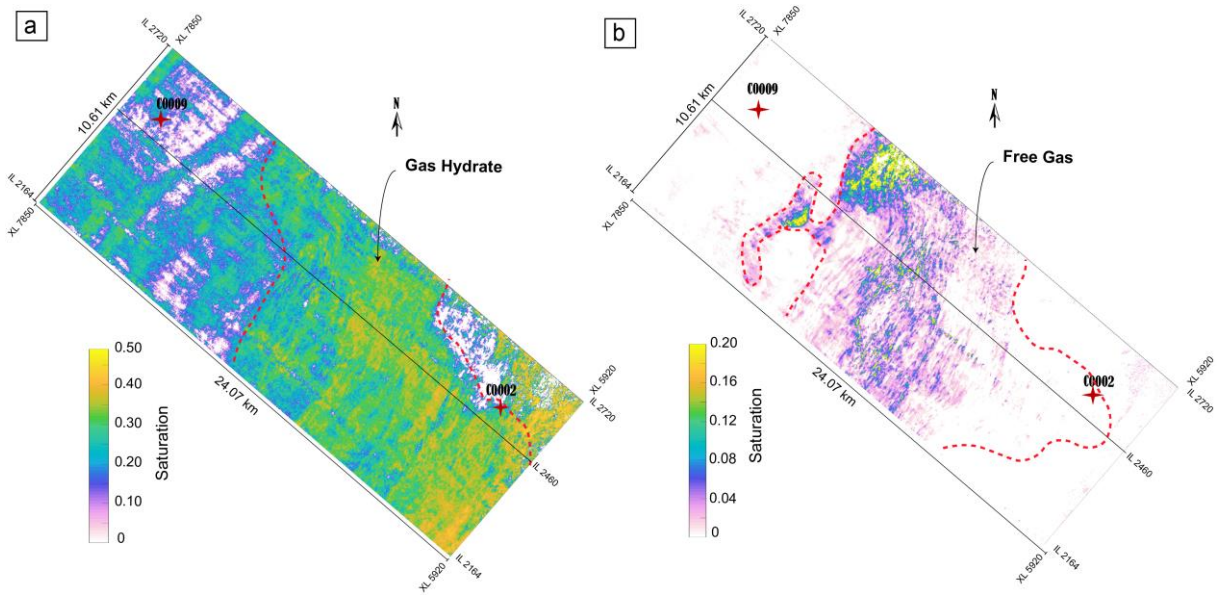

Figure 2.11 Timeslices of 3D hydrate and free gas saturation. (a) Gas hydrate saturation along the horizon of 3.0 s TWT above BSR. (b) Free gas saturation along the horizon of 3.2 s TWT below BSR. Red dashed lines indicate the boundary of spatial gas hydrate and free gas accumulation zones. Same red dashed lines are in Figure 7

and in the bottom part of the basin (Figure 2.9c). The free gas saturation beneath BSR at timeslice 3.2 s TWT from rock physics approaches based on pore-filling model is 0-20% in the pore space (Figure 2.11b). However, the local zones of spatial gas saturation calculated from pore-filling model, where I used only seismic interval velocity as a single parameter to determine porosity and saturation profile without additional well control, give abnormally high values greater than 20% in the pore space where velocities of free gas-bearing sediments is extraordinarily low as approximately as 1000 m/s (Figure 2.11b).

The drilling sites C0002 and C0009 penetrated in Kumano sediments did not encounter overpressure zones (Moore et al., 2011; Saffer et al., 2013), although the deposits occurring in the Kumano forearc basin were formed with high sedimentation rate. Furthermore, Saffer et al. (2013) certified that the permeabilities in the lower basin estimated from permeability-porosity

relationships through laboratory test on core samples at Site C0009 is lower than $10^{-16}m^2$ which can indicate the possibility of overpressure generation (Toki et al., 2012; Dugan and Sheahan, 2012). On the other hand, excess pore fluid pressure released from mega splay faults (Tsuji et al., 2014b) migrated upward through numerous fractures and confined above the ridge topography (Figure 2.9b) and in the bottom part of basin (Figure 2.9c), which can be trapped high pore fluid pressure therein. Therefore, gas saturated content and overpressured pore fluid contributed to decrease in seismic velocity of sediments in the studied area. If the gas reservoir zone is in overpressure conditions, the gas saturation estimated in this study could be considered as maximum value.

2.7 Discussion

2.7.1 Hydrate and gas reservoirs in forearc basin

The seismic velocity model indicates strong lateral variations. In the Kumano forearc basin, the stratified sediments are associated to turbidites. Logging data at Site C0002 indicate that the gas hydrate-bearing zones (218.1-400.4 m LSF) and potential gas-bearing zones (481.6-547.1 m LSF) occur within the sandy horizons of the turbidite deposits (Expedition 314 Scientists, 2009). The Kumano turbidite sediments are composed of alternating beds of sand and mud facies as indicated in serrated Gamma Ray (GR) log (Figure 2.4) representing sand facies with low GR trend, and mud facies with high GR trend. Detailed studies for lithofacies, sedimentary facies, hydrate and gas occurrences in the Nankai Trough are compiled in papers and IODP expedition reports (Moore et al., 2015; Ito et al., 2015). Gas migrated through permeable sand layers and accumulated as hydrate and free gas reservoirs in the basin. Gas can occur in the mud facies if time

is promising for gas migration and accumulation through low permeable layers (Baba and Yamada, 2004). The highly concentrated hydrate reservoir developed near the outer ridge, and gas reservoirs are widely dispersed beneath BSR (Figure 2.9a) above the ridge topography (Figure 2.9b) and the portion of 1.0 s TWT deeper than BSR trapped in the mud layer at the bottom part of the basin (Figure 2.9c). These observations suggest a porosity variation, and sedimentary facies control in the Kumano hydrocarbon gas reservoirs in the Nankai accretionary prism.

Moreover, gas hydrates with high P-wave velocity are present around the rim of the outer ridge in the forearc basin (Figure 2.9a), which can be related to the change in rock properties due to the different compaction of marine sediments in the Nankai accretionary prism due to faulting in accretionary complex or associated to the uplift of the outer ridge (Loreto et al., 2007). An opposite trend was observed in which the free gas distribution is pervasive below the BSR (Figure 9a), and above the ridge topography (Figure 2.9b). Low P-wave velocity of gas reservoir developed just above the ridge topography considered as a structural trap for the accumulation of fluids in the pore space (Figure 2.9c). The widely distributed hydrate and gas reservoirs with the abnormally high and low P-wave velocities could imply their high concentration (Figure 9a). Based on saturation estimations, the trend of spatial hydrate saturation distribution above BSR is comparable to Jia et al. (2016) which used acoustic impedance inversion for hydrate saturation estimation, yet the estimate of spatial gas hydrate saturation ranging from 0% to 45% in the pore volume is higher than Jia et al. (2016) whose spatial gas hydrate saturation is less than 35% in the pore volume. Because seismic velocity analysis has higher resolution and less assumption compared with acoustic impedance inversion of Jia et al. (2016), I can well-delineate spatial gas hydrate and free gas distribution and concentration. Furthermore, I obtained spatial free gas saturation ranging from 0% to 20% in the pore volume. Nevertheless, without *in situ* measurement, the estimation of gas

hydrate and free gas saturation is influenced by several assumptions (Vargas-Cordero et al, 2010). Because of such assumptions, the saturations estimated in this study may include errors.

Gas hydrate morphology is classified into three models: pore filling, load-bearing (or matrix-supporting), and cementing (Waite et al., 2009). Based on the hydrate saturation results (Figures 2.10 and 2.11), I assumed that hydrate morphology is most likely attached to mineral grains, not floating in the pore space (Jia et al., 2016). This causes porosity reduction and contributes to mechanical stability of sediment frame (Waite et al., 2009). The result from seismic data shows gas hydrate saturation of 29% on average (Figure 10) with spatially reaching up to 45% in the pore space (Figure 2.11). This estimation can support an assumption that most probable gas hydrate in this study area are matrix-supporting, because when hydrate saturation in the pore space exceeds 25%-40%, pore-filling hydrate naturally transforms into matrix-supporting hydrate which treats hydrate as load-bearing (Waite et al., 2009). Furthermore, Jin et al. (2016) studied the hydrate morphology of natural gas hydrate-bearing sediments in the eastern Nankai trough. They conducted their experiment of hydrated samples under hydrostatic pressurized conditions that prevent dissociation of gas hydrates in sediments, and they investigated that the hydrate morphology of natural gas hydrate sediments in their studied area demonstrated a load-bearing morphology type.

The BSR distribution I identified in this study displays a double continuous reflection pattern (Figure 2.8a). This phenomenon is correspondent to the non-equilibrium condition for BSR development associated with changes in temperature and pressure or fluid transport due to the tectonic uplift of the accretionary prism (Foucher et al., 2002; Jia et al., 2016). This process can lead to the co-existence of free gas and gas hydrates caused by (1) gas flux migration upward through the permeable pathway, (2) changes in pressure and temperature across faults and then

penetrate partially in the hydrate stability zone (Miyakawa et al., 2014, Dev and McMechan 2010), or (3) recycling of gas hydrates due to their preexisting gas hydrate dissociation when the BGHS moves upward or downward due to tectonic uplift or subsidence (Baba and Yamada, 2004).

2.7.2 Fluid flows, hydrocarbon gas accumulation, and traps

In situ biogenic methane gas and deep thermogenic gas are two primary sources for gas hydrates (Ruppel and Kessler, 2017). In the Nankai Trough area, the total organic carbon (TOC) was measured around 0.5%, which is classified as too low for *in situ* biogenic methane gas generation and expulsion (Waseda and Uchida, 2004); however, the mixing of biogenic and thermogenic methane gas also occurred in the Nankai Trough area (Hammerschmidt et al., 2014). The fluid flows in the Nankai accretionary prism are active through the faults generated by plate subduction. It was implied that the thermal cracking of organic matter generated gas at depth and expelled gas to migrate upward (Pape et al, 2014; Waseda and Uchida, 2004).

A dense development of normal faults is seen due to the intensive tectonic movements near the outer ridge, and many faults cut across the basin in the studied seismic profile (Figure 2.12). The development of fractures or faults around the outer ridge could be caused by oblique plate convergence (Martin et al., 2010; Tsuji et al., 2011; 2014b). Seismic evidences using a waveform tomography velocity model integrated with rock physics theory (Tsuji et al., 2014a) revealed pore pressure distribution of a plate boundary décollement in the Nankai subduction zone. The strike-slip faults close to the outer ridge released excess pore fluids trapped underneath the plate boundary

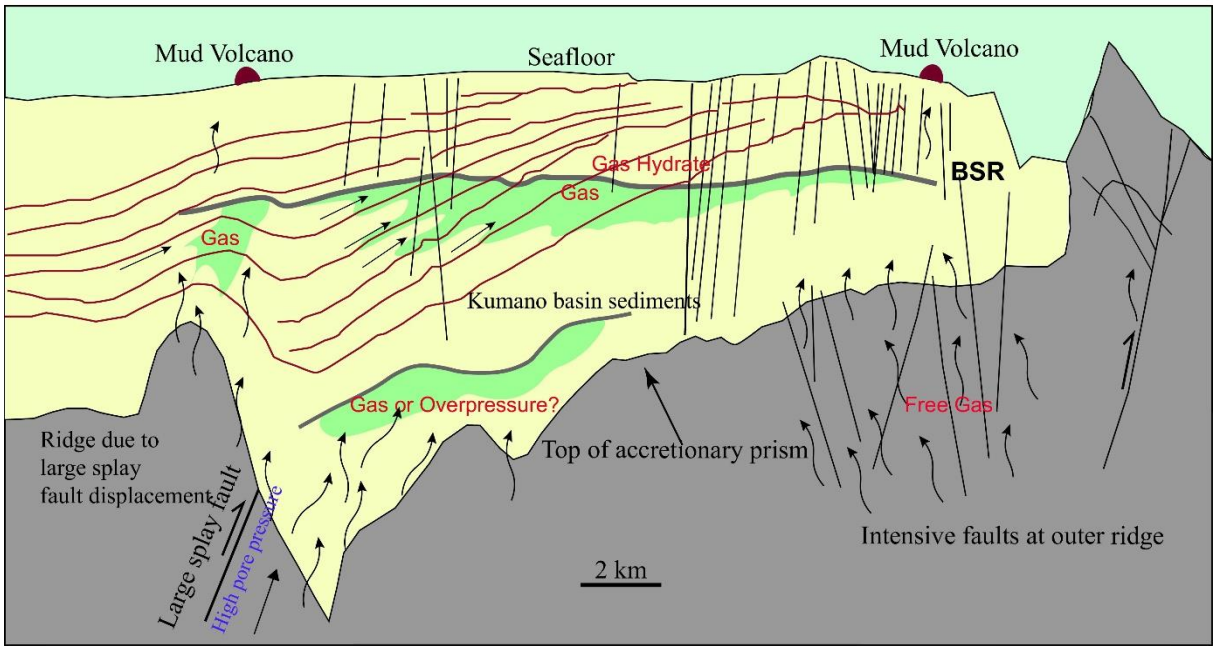

Figure 2.12 Schematic model of hydrocarbon gas migration processes and formation in the Kumano forearc basin on profile of IL 2460

décollement. This high pore fluid pressure in the underlying accretionary prism contributed to occurrence of fluid expulsion, which further encouraged free gas to migrate upward through fractures or cracks and steeply dipping strata in the shallow formation where temperature and pressure are favourable to gas hydrate formation. The gas hydrate distribution is furthermore assumed to be an impermeable layer that can act as a stratigraphic trap for the free gas.

Ridge topography (Figure 2.8a) is caused by displacement of a huge reverse fault branching from a plate boundary décollement in the depth about 10 km (Ramirez et al., 2015; Tsuji et al., 2015). Since the gas reservoir develops above this ridge topography located on large faults diverging from the deep plate boundary fault (Tsuji et al., 2015), it is considered that free gas was supplied along the large faults, and free gas was confined by anticline structure (Figure 2.9b).

Furthermore, low-velocity distribution of hydrate and gas reservoirs (Figure 2.9b and 2.9c) just overlying the large splay faults (Figure 2.12) also implied that the high pore pressure fluid in deep strata along huge branch faults from the plate interface which were being enriched in fluid through to move upward (Tsuji et al., 2015). Therefore, the intensive tectonic movements in the plate convergent margin had strongly influenced on hydrate and gas distribution and accumulation in the forearc basin.

2.8 Conclusions

From the velocity model, the gas hydrate and free gas portions are extensively accumulated in the Kumano forearc basin. Based on the results, I can summarize the main findings as follows:

- The resulting velocity model from automatic picking algorithm produces the high resolution profile which allows us to better delineate the gas hydrate and free gas accumulation. The result is useful to qualitatively assess hydrate and free gas resources in the forearc basin of deep-water environment.
- Gas hydrate-bearing sediments above the BSR and free gas-bearing sediments below the BSR are characterized by P-wave velocities of 1,900 – 2,500 m/s, and 1,000 – 1,800 m/s, respectively. The distribution of gas hydrate saturation is spatially ranging from 0-45% in the pore space along the basin. Gas hydrates are highly concentrated near the outer ridge where faults are densely developed due to fault activities within the accretionary prism. The distribution of gas saturation is spatially ranging from 0-20% widespread below BSR, and highly concentrated above the ridge topography. The gas saturation above the ridge could be

higher because the gas reservoir velocity is slower than water velocity. Another factor reducing velocity of the gas reservoir above the ridge is due to overpressured pore fluid within the Kumano sediments and gas supply from the underlying accretionary prism.

- The free gas zones are widespread below the BSR, confined in the anticline structure above ridge topography, and in the mud layer at the deeper part of the basin. Sand and mud facies in the Kumano turbidite sediments are one of the controlling factors for hydrocarbon gas transport and accumulations through the permeable sand layers.
- Gas sources for hydrate and gas reservoir development and distribution in the Kumano forearc basin resulted from excess pore fluid pressure discharging methane gas along large faults from deep strata of the Nankai accretionary sediments, and methane gas migrated upward along numerous faults, fractures and steeply dipping strata. Therefore, faulting and tectonic activities within the underlying accretionary prism in the Nankai subduction zone are another controlling factor for hydrate and gas reservoir distribution in the Kumano forearc basin.

2.9 References

Archie, G.E., 1942, The electrical resistivity log as an aid in determining some reservoir characteristics: *Transactions of the AIME,* **146(01)**, 54–62.

Ashi, J., Tokuyama, H., and Taira, A., 2002, Distribution of methane hydrate BSRs and its implication for the prism growth in the Nankai Trough: *Marine Geology*, **187**, 177–191. doi:10.1016/S0025-3227(02)00265-7

Baba, K., and Yamada, Y., 2004, BSRs and associated reflections as an indicator of gas hydrate and free gas accumulation: an example of accretionary prism and forearc basin system along the Nankai Trough, off central Japan: *Resource Geology*, **54**, 11–24. doi:10.1111/j.1751 3928.2004.tb00183.x

Collett, T. S., and Ladd, J., 2000, Detection of gas hydrate with downhole logs and assessment of gas hydrate concentrations (saturations) and gas volumes on the Blake Ridge with electrical resistivity data: *Proceedings of the Ocean Drilling Program: Scientific Results*, **164**, 179–191.

Dev, A. and McMechan, G.A., 2010, Interpreting structural controls on hydrate and free-gas accumulation using well and seismic information from the Gulf of Mexico: *Geophysics*, **75(1)**, B35–B46. doi:10.1190/1.3282680

Dix, C.H., 1955, Seismic velocities from surface measurements. *Geophysics*, ***20*(1)**, 68–86. doi: 10.1190/1.1438126

Dugan, B. and Sheahan, T.C., 2012, Offshore sediment overpressures of passive margins: Mechanisms, measurement, and models: *Reviews of Geophysics*, **50(3)**.

Dvorkin, J., Prasad, M., Sakai, A., and Lavoie, D., 1999, Elasticity of marine sediments: rock physics modeling: *Geophysical Research Letters*, **26**, 1781–1784. doi: 10.1029/1999GL900332

Ecker, C., Dvorkin, J., and Nur, A. M., 2000, Estimating the amount of gas hydrate and free gas from marine seismic data: *Geophysics*, **65**, 565–573. doi:10.1190/1.1444752

Expedition 314 Scientists, 2009*a*, Expedition 314 Site C0002, *in* M. Kinoshita, H. Tobin, J. Ashi, G. Kimura, S. Lallemant, E. J. Screaton, D. Curewitz, H. Masago, K. T. Moe, and the Expedition 314/315/316 Scientists, eds, *Proceedings of the Integrated Ocean Drilling*

Program, 314/315/316: Integrated Ocean Drilling Program Management International, Inc., 1–77.

Expedition 314 Scientists, 2009*b*, Expedition 314 methods, *in* M. Kinoshita, H. Tobin, J. Ashi, G. Kimura, S. Lallemant, E. J. Screaton, D. Curewitz, H. Masago, K. T. Moe, and the Expedition 314/315/316 Scientists, eds, *Proceedings of the Integrated Ocean Drilling Program, 314/315/316*: Integrated Ocean Drilling Program Management International, Inc., 1–33.

Expedition 315 Scientists, 2009, Expedition 315 Site C0002, *in* M. Kinoshita, H. Tobin, J. Ashi, G. Kimura, S. Lallemant, E. J. Screaton, D. Curewitz, H. Masago, K. T. Moe, and the Expedition 314/315/316 Scientists, eds, *Proceedings of the Integrated Ocean Drilling Program, 314/315/316*: Integrated Ocean Drilling Program Management International, Inc., 1–76.

Expedition 319 Scientists, 2010, Expedition 319 summary, *in* D. Saffer, L. McNeill, T. Byrne, E. Araki, S. Toczko, N. Eguchi, K. Takahashi, and the Expedition 319 Scientists, eds, *Proceedings of the Integrated Ocean Drilling Program 319*: Integrated Ocean Drilling Program Management International, Inc., 1–46.

Fomel, S., 2009, Velocity analysis using AB semblance: *Geophysical Prospecting*, **57(3)**, 311–321. doi:10.1111/j.1365-2478.2008.00741.x

Fomel, S. and Landa, E., 2014, Structural uncertainty of time-migrated seismic images: *Journal of Applied Geophysics*, **101**, 27–30. doi: 10.1016/j.jappgeo.2013.11.010

Fomel, S., Sava, P., Vlad, I., Liu, Y. and Bashkardin, V., 2013, Madagascar: Open-source software project for multidimensional data analysis and reproducible computational experiments: *Journal of Open Research Software*, **1(1)**.

Foucher, J. P., Nouze, H., and Henry, P., 2002, Observation and tentative interpretation of a double BSR on the Nankai Slope: *Marine Geology*, **187**, 161–175. doi:10.1016/S0025-3227(02)00264-5

Fujii, T., Saeki, T., Kobayashi, T., Inamori, T., Hayashi, M., Takano, O., Takayama, T., Kawasaki, T., Nagakubo, S., Nakamizu, M., and Yokoi, K., 2008, Resource assessment of methane hydrate in the eastern Nankai Trough, Japan: Offshore Technology Conference, 5–8 May, Houston, Texas, USA, 1–15.

Hammerschmidt, S.B., Wiersberg, T., Heuer, V.B., Wendt, J., Erzinger, J. and Kopf, A., 2014, Real-time drilling mud gas monitoring for qualitative evaluation of hydrocarbon gas composition during deep sea drilling in the Nankai Trough Kumano Basin: *Geochemical transactions*, **15(1)**, 15. doi: 10.1186/s12932-014-0015-8

Hardage, B.A. and Roberts, H. H., 2006, Gas hydrate in the Gulf of Mexico: What and where is the seismic target?: *The Leading Edge*, **25(5)**, 566–571. doi:10.1190/1.2202660

Helgerud, M. B., Dvorkin, J., Nur, A., Sakai, A., and Collett, T., 1999, Elastic wave velocity in marine sediments with gas hydrates: effective medium modelling: *Geophysical Research Letters*, **26**, 2021–2024. doi:10.1029/1999GL900421

Hovland, M., Orange, D., Bjorkum, P. A., and Gudmestad, O. T. 2001, January, Gas Hydrate And Seeps-Effects On Slope Stability: The" Hydraulic Model". The Eleventh International Offshore and Polar Engineering Conference. International Society of Offshore and Polar Engineers.

Hyndman, R.D. and Spence, G.D., 1992, A seismic study of methane hydrate marine bottom simulating reflectors: *Journal of Geophysical Research: Solid Earth*, **97(B5)**, 6683–6698. doi:10.1029/92JB00234

Ito, T., Komatsu, Y., Fujii, T., Suzuki, K., Egawa, K., Nakatsuka, Y., Konno, Y., Yoneda, J., Jin, Y., Kida, M. and Nagao, J., 2015, Lithological features of hydrate-bearing sediments and their relationship with gas hydrate saturation in the eastern Nankai Trough, Japan: *Marine and Petroleum Geology*, **66**, 368–378. doi: 10.1016/j.marpetgeo.2015.02.022

Jia, J., Tsuji, T. and Matsuoka, T., 2016, Gas hydrate saturation and distribution in the Kumano Forearc Basin of the Nankai Trough: *Exploration Geophysics*, **48(2)**, 137–150. doi:10.1071/EG15127

Jin, Y., Konno, Y., Yoneda, J., Kida, M. and Nagao, J., 2016, In situ Methane Hydrate Morphology Investigation: Natural Gas Hydrate-Bearing Sediment Recovered from the Eastern Nankai Trough Area: *Energy & Fuels*, **30(7)**, 5547–5554. doi: 10.1021/acs.energyfuels.6b00762

Kretschmer, K., Biastoch, A., Rüpke, L. and Burwicz, E., 2015, Modeling the fate of methane hydrates under global warming: *Global Biogeochemical Cycles*, **29(5)**, 610–625. doi: 10.1002/2014GB005011

Kuramoto, S., J. Ashi, J. Greinert, S. Gulick, T. Ishimura, S. Morita, K. Nakamura, M. Okada, T. Okamoto, D. Rickert, S. Saito, E. Suess, U. Tsunogai, and T. Tomosugi, 2001, Surface observations of subduction related mud volcanoes and large thrust sheets in the Nankai subduction margin; Report on YK00-10 and YK01-04 cruises, JAMSTEC Deep Sea Res., 19, 131–139.

Kvenvolden, K. A., 1993, Gas hydrates-geological perspective and global change: *Reviews of Geophysics*, **31**, 173–187. doi:10.1029/93RG00268

Loreto, M.F., Tinivella, U. and Ranero, C. R., 2007, Evidence for fluid circulation, overpressure and tectonic style along the Southern Chilean margin. *Tectonophysics*, **429(3)**, 183–200. doi:10.1016/j.tecto.2006.09.016

Lu, S. M., and McMechan, G. A., 2002, Estimation of gas hydrate and free gas saturation, concentration, and distribution from seismic data: *Geophysics*, **67**, 582–593. doi:10.1190/1.1468619

Martin, K.M., et al., 2010, Possible strain partitioning structure between the Kumano fore-arc basin and the slope of the Nankai Trough accretionary prism: *Geochem. Geophys. Geosyst*, **11**. doi: 10.1029/2009GC002668

Matsumoto, R., Tomaru, H., and Lu, H. L., 2004, Detection and evaluation of gas hydrates in the eastern Nankai Trough by integrated geochemical and geophysical methods: *Resource Geology*, **54**, 53–67. doi:10.1111/ j.1751-3928.2004.tb00187.x

Milkov, A.V., 2004, Global estimates of hydrate-bound gas in marine sediments: how much is really out there?: *Earth-Science Reviews*, **66(3)**, 183–197. doi:10.1016/j.earscirev.2003.11.002

Miyakawa, A., Saito, S., Yamada, Y., Tomaru, H., Kinoshita, M., and Tsuji, T., 2014, Gas hydrate saturation at Site C0002, IODP Expeditions 314 and 315, in the Kumano Basin, Nankai Trough: *The Island Arc*, **23**, 142–156. doi:10.1111/iar.12064

Moore, G.F., Boston, B.B., Strasser, M., Underwood, M.B. and Ratliff, R.A., 2015, Evolution of tectono-sedimentary systems in the Kumano Basin, Nankai Trough forearc: *Marine and Petroleum Geology,* **67**, 604–616. Doi:10.1016/j.marpetgeo.2015.05.032

Moore, G. F., Park, J. O., Bangs, N. L., Gulick, S. P., Tobin, H. J., Nakamura, Y., Sato, S., Tsuji, T., Yoro, T., Tanaka, H., Uraki, S., Kido, Y., Sanada, Y., Kuramoto, S., and Taira, A., 2009,

Structural and seismic stratigraphic framework of the NantroSEIZE Stage 1 transect, *in* M. Kinoshita, H. Tobin, J. Ashi, G. Kimura, S. Lallemant, E. J. Screaton, D. Curewitz, H. Masago, K. T. Moe, and the Expedition 314/315/316 Scientists, eds, *Proceedings of the Integrated Ocean Drilling Program 314/315/316*: Integrated Ocean Drilling Program Management International, Inc., 1–46.

Moore, J. C., Chang, C., McNeill, L., Thu, M.K., Yamada, Y. and Huftile, G., 2011, Growth of borehole breakouts with time after drilling: Implications for state of stress, NanTroSEIZE transect, SW Japan: *Geochemistry, Geophysics, Geosystems*, **12(4)**. doi: 10.1029/2010GC003417

Morita, S., J. Ashi, K. Aoike, and S. Kuramoto, 2004, Evolution of Kumano basin and sources of clastic ejecta and pore fluid in Kumano mud volcanoes, Eastern Nanaki Trough, In: Proceedings of the International Symposium on Methane Hydrates and Fluid Flow in Upper Accretionary Prisms, Engineering Geology Laboratory, Department of Civil & Earth Resources Engineering, Kyoto University, Kyoto, Japan, 92–99.

Murphy, W.F. Ill, 1982, Effects of Microstructure and Pore Fluids on the Acoustic Properties of Granular Sedimentary Materials, Ph.D. Dissertation, Stanford University.

Nur, A., Mavko, G., Dvorkin, J. and Galmudi, D., 1998, Critical porosity: A key to relating physical properties to porosity in rocks. *The Leading Edge*, **17(3)**, 357–362. doi: 10.1190/1.1437977

Pearson, C. F., Halleck, P. M., McGuire, P. L., Hermes, R., and Mathews, M., 1983, Natural gas hydrate: a review of in situ properties: *Journal of Physical Chemistry*, **87**, 4180–4185. doi: 10.1021/j100244a041

Pape, T., Geprags, P., Hammerschmidt, S., Wintersteller, P., Wei, J., Fleischmann, T., Bohrmann, G., and Kopf, A. J., 2014, Hydrocarbon seepage and its sources at mud volcanoes of the Kumano forearc basin, Nankai Trough subduction zone: *Geochemistry, Geophysics, Geosystems*, **15**, 2180–2194. doi:10.1002/2013GC005057

Ramirez, S. G., Gulick, S.P.S., Hayman, N.W., 2015, Early sedimentation and defor-mation in the Kumano forearc basin linked with Nankai accretionary prism evolution, southwest Japan: *Geochem. Geophys. Geosyst*, **16**, 1616–1633. doi: 10.1002/2014GC005643

Ruppel, C.D. and Kessler, J. D., 2017, The interaction of climate change and methane hydrates: *Reviews of Geophysics*. doi: 10.1002/2016RG000534

Saffer, D.M., Flemings, P.B., Boutt, D., Doan, M.L., Ito, T., McNeill, L., Byrne, T., Conin, M., Lin, W., Kano, Y. and Araki, E., 2013, In situ stress and pore pressure in the Kumano Forearc Basin, offshore SW Honshu from downhole measurements during riser drilling: *Geochemistry, Geophysics, Geosystems*, **14(5)**, 1454–1470. doi: 10.1002/ggge.20051

Saffer, D., McNeill, L., Araki, E., Byrne, T., Eguchi, N., Toczko, S., Takahashi, K., and the Expedition 319 Scientists, 2009, NanTroSEIZE Stage 2: NanTroSEIZE riser/riserless observatory: Integrated Ocean Drilling Program Expedition 319 Preliminary Report, 1–83.

Shipley, T. H., Houston, M. H., Buffler, R.T., Shaub, F. J., McMillen, K.J., Ladd, J.W. and Worzel, J.L., 1979, Seismic evidence for widespread possible gas hydrate horizons on continental slopes and rises. *AAPG bulletin*, **63(12)**, 2204–2213.

Sloan, E.D. Jr, and Koh, C., 2007, *Clathrate hydrates of natural gases* (3rd edition): CRC Press.

Strasser, M., Dugan, B., Kanagawa, K., Moore, G. F., Toczko, S., Maeda, L., Kido, Y., Moe, K. T., Sanada, Y., Esteban, L., Fabbri, O., Geersen, J., Hammerschmidt, S., Hayashi, H.,

Heirman, K., Hupers, A., Jurado Rodriguez, M. J., Kameo, K., Kanamatsu, T., Kitajima, H., Masuda, H., Milliken, K., Mishra, R., Motoyama, I., Olcott, K., Oohashi, K., Pickering, K. T., Ramirez, S. G., Rashid, H., Sawyer, D., Schleicher, A., Shan, Y., Skarbek, R., Song, I., Takeshita, T., Toki, T., Tudge, J., Webb, S., Wilson, D. J., Wu, H.-Y., and Yamagushi, A., 2014, Site C0002, *in* M. Strasser, B. Dugan, K. Kanagawa, G. F. Moore, S. Toczko, L. Maeda, and the Expedition 338 Scientists, eds, *Proceedings of the Integrated Ocean Drilling Program, 338*: Integrated Ocean Drilling Program, 1–248.

Taladay, K. B. and Moore, G. F., 2015, Concentrated gas hydrate deposits in the Kumano Forearc Basin, Nankai Trough, Japan. *Center for Natural Gas and Oil*, ***412***, 386–7614.

Toki, T., Uehara, Y., Kinjo, K., Ijiri, A., Tsunogai, U., Tomaru, H., and Ashi, J., 2012, Methane production and accumulation in the Nankai accretionary prism: results from IODP Expeditions 315 and 316: *Geochemical Journal*, **46**, 89–106. doi: 10.2343/geochemj.1.0155

Tsuji, Y., Namikawa, T., Fujii, T., Hayashi, M., Kitamura, R., Nakamizu, M., Ohbi, K., Saeki, T., Yamamoto, K., Inamori, T., Oikawa, N., Shimizu, S., Kawasaki, M., Nagakubo, S., Matsushima, J., Ochiai, K., and Okui, T., 2009, Methane-hydrate occurrence and distribution in the eastern Nankai Trough, Japan: findings of the Tokai-oki to Kumano-nada methane-hydrate drilling program: *AAPG Memoir*, **89**, 228–246.

Tsuji, T., Dvorkin, J., Mavko, G., Nakata, N., Matsuoka, T., Nakanishi, A., Kodaira, S., and Nishizawa, O., 2011, Vp/Vs ratio and shear-wave splitting in the Nankai Trough seismogenic zone: insights into effective stress, pore pressure and sediment consolidation: *Geophysics*, **76**, WA71–WA82. doi:10.1190/1.3560018

Tsuji, T., Kamei, R., and Pratt, R. G., 2014*a*, Pore pressure distribution of a mega-splay fault system in the Nankai Trough subduction zone: insight into up-dip extent of the seismogenic zone: *Earth and Planetary Science Letters*, **396**, 165–178. doi:10.1016/j.epsl.2014.04.011

Tsuji, T., Ashi, J., and Ikeda, Y., 2014*b*, Strike-slip motion of a mega-splay fault system in the Nankai oblique subduction zone: *Earth, Planets, and Space*, **66**, 1–14. doi:10.1186/1880-5981-66-120

Tsuji, T., Ashi, J., Strasser, M., and Kimura, G., 2015, Identification of the static backstop and its influence on the evolution of the accretionary prism in the Nankai Trough: *Earth and Planetary Science Letters*, **431**, 15–25. doi:10.1016/j.epsl.2015.09.011

Uchida, T., Lu, H. L., and Tomaru, H., the MITI Nankai Trough shipboard scientists 2004, Subsurface occurrence of natural gas hydrate in the Nankai Trough area: implication for gas hydrate concentration: *Resource Geology*, **54**, 35–44. doi:10.1111/j.1751-3928.2004.tb00185.x

Vargas-Cordero, I., Tinivella, U., Accaino, F., Loreto, M. F. and Fanucci, F., 2010, Thermal state and concentration of gas hydrate and free gas of Coyhaique, Chilean Margin (44 30′ S): *Marine and Petroleum Geology*, **27(5)**, 1148–1156. doi: 10.1016/j.marpetgeo.2010.02.011

Waite, W. F., Santamarina, J. C., Cortes, D. D., Dugan, B., Espinoza, D. N., Germaine, J., Jang, J., Jung, J. W., Kneafsey, T. J., Shin, H., Soga, K., Winters, W. J., and Yun, T. S., 2009, Physical properties of hydrate-bearing sediments: *Reviews of Geophysics*, **47**, RG4003. doi:10.1029/ 2008RG000279

Wang, X. J., Wu, S. G., Lee, M., Guo, Y. Q., Yang, S. X., and Liang, J. Q., 2011, Gas hydrate saturation from acoustic impedance and resistivity logs in the Shenhu area, South China

Sea: *Marine and Petroleum Geology*, **28**, 1625–1633. doi:10.1016/j.marpetgeo.2011.07.002

Waseda, A. and Uchida, T., 2004, Origin and migration of methane in gas hydrate-bearing sediments in the Nankai Trough: *The Geochemical Society Special Publications*, **9**, 377–387. doi: 10.1016/S1873-9881(04)80027-0

Xu, W. and Germanovich, L.N., 2006, Excess pore pressure resulting from methane hydrate dissociation in marine sediments: A theoretical approach: *Journal of Geophysical Research*, **111(B1)**. doi: 10.1029/2004JB003600

Chapter 3

Prediction of pore pressure and fluid saturation effects in the Kumano forearc basin, Nankai Trough, Japan

Abstract

An estimation of pore pressure was performed in the Kumano forearc basin of Nankai Trough area, Japan using high resolution and accurate seismic velocity inferred from automatic velocity analysis. Herein, the modified Eaton's equation for P- and S-wave velocity ratio to estimate pore pressure was implemented. For this basin, widely distributed hydrate and gas reservoirs were found, and the abnormal low velocity and seismic response due to change in pore pressure and fluid saturation were presented. Pore pressure buildup and fluid saturation effects were discriminated by estimating a high-resolution *S*-wave velocity (*Vs*) in addition to *P*-wave velocity (*Vp*) using

pre-stack waveform inversion. The result demonstrates that the pore pressure is remained in hydrostatic condition in the hydrate and gas layer, and the pore pressure increases with depth to maintain the hydrostatic condition in the deeper sediments. The various fluids effects and the pore pressure distribution observed both from *Vp* and *Vs* were discussed. Based on these results, I can elucidate pore pressure generation mechanisms and various factors contributed to maintain hydrostatic pore pressure within the widely hydrate and gas reservoirs in this study area. Intricate basin formation processes and the compressional subduction in the Nankai plate convergent margin do not influence or contribute to the overpressured pore fluids in the Kumano forearc basin.

Keywords: Automatic velocity analysis, seismic inversion, pore pressure, rock physics,

3.1 Introduction

Pore pressure prediction in the unconventional resources of deep water environment (i.e., gas hydrate) plays a critical role in exploration stage (Sayers et al., 2006). Gas hydrate exists in the condition of low temperature and high pressure environment in the deep water offshore and permafrost regions. Gas hydrate potentially traps underlying free gas (Kvenvolden, 1993; Sloan and Koh, 2007). The deep offshore reservoir exploration provides potential risks for the drilling program and operations. Knowledge of pore pressure is important for exploration of energy resources, in addition to prevention of drilling hazards as well as understanding their complex geological and deformation processes in the earth's crust (Kumar et al., 2014). High pore pressure decreases effective stress and enables fault slips or fault reactivation, information about pore pressure distribution is crucial for understanding the deformation and stress in the subsurface (Moore et al., 2012). Specifically, overpressure zone not only caused the drilling blowout, but also induced geological hazards such as mud volcano eruptions (Zhang, 2011). In addition, there are three main potential risks happening if occurrence of abnormally high pore pressure resulted from hydrate dissociation, such as 1) to trigger submarine landslides in shallow water environments; 2) to result in the formation of upward fluid flow and migration; 3) to cause the failure of a sediment layer confined by low permeability barriers in relatively deep water environments (Xu and Germanovich, 2006; Kumar et al., 2014).

Hydrate and gas reservoirs are widely distributed in Kumano forearc basin (Chhun et al., 2018). Kumano forearc basin is located to the southeast of the Kii Peninsula, Japan, overlying the accretionary prism in the Nankai Trough where the Philippine Sea plate is subducting beneath the Japanese islands (Figure 2.1). The basin initially formed during the uplift of mega splay fault filled

by sediments from Quaternary to recent age. Basin change configuration due to complex sedimentation, stratigraphy, high pore fluid pressure expulsion linked to compression stress of the Nankai subduction zone, the seismic imaging reveals the submarine slides, a dozens of mud volcanoes and widespread hydrate & gas throughout this basin (Expedition 314 Scientists, 2009a, Moore et al, 2012; Saffer et al., 2013; Tsuji et al., 2014; Jia et al., 2017; Chhun et al., 2018; Pape et al., 2014; Taladay et al, 2017). The basin was filled with rapid sedimentation rate (sand, silt, mud intercalations) about 2km overlying the accretionary prism which are cross-cut by a series of deep-cutting normal faults due to the intensive tectonic movement in this plate convergent margin (Expedition 314 Scientists, 2009a, Moore et al, 2012; Saffer et al., 2013; Tsuji et al., 2014; Jia et al., 2017; Chhun et al., 2018; Pape et al., 2014; Taladay et al, 2017). The seafloor is relatively flat at ~2000 m water depth with a bottom water temperature of 2 ◦C; sand/mud turbidite deposits were saturated partially from potential fluid expulsion from depth, which are favorable for the environment and condition of hydrate and gas formation in this basin (Taladay et al.,2017; Chhun et al., 2018; Jia et al., 2016). These geological settings in the Kumano forearc basin can generate compaction disequilibrium within this basin.

Pressure changes in combination with fluid-saturation changes create abnormal seismic responses. Abnormal pore pressure commonly occurs in the deep water environment when the sediments are under compacted (i.e., compaction disequilibrium). Therefore, the fluid cannot escape or expel deviating from normal compaction trend (Sayers, 2006; Zhang, 2011; Zhang, 2013). There are other several reasons for abnormal pore pressure in the subsurface formation such as hydrocarbon generation, gas cracking, aquathermal expansion, lateral stress/transfer, clay diagenesis, and hydrocarbon buoyancy. This is creating low velocity trend, which departs from normal compaction trend through depth (Sayers, 2006; Zhang, 2011; Zhang, 2013).

In this study I used high resolution 3D velocity model to estimate pore pressure. It is difficult to separate pore pressure and fluid saturation effects only from *Vp* data. Because *Vp/Vs* is sensitive to fluid saturation, I estimated *Vs* via pre-stack seismic waveform inversion (Landrø, 2014). Therefore, I can distinguish the high pore pressure and fluid saturation. In addition, I adapted the modified Eaton's (1972) method via *Vp/Vs*-to-pore-pressure transform to estimate pore pressure using seismic *Vp*-*Vs* velocities with reservoir pressure data calibration (Giao, 2015; Ebrom, 2006; Saleh et al., 2013). Due to the effect of gas contents in the rocks, *Vp* data were corrected in the gas zone, then applied to estimate pore pressure distribution. Furthermore, pore pressure analysis in this basin will be useful for predrill prediction in the foreseeable drillings, and this study will also elucidate the mechanisms of pore pressure generation related to widespread hydrate and gas formation and their connection to geological and deformation processes in this plate convergent margin.

3.2 Well and Seismic data

The IODP (Integrated Ocean Drilling Program) Expedition 314 provided a suite of logging while drilling (LWD) logs, including caliper, near bit resistivity, density, gamma ray (GR), sonic, density porosity, and neutron porosity log. Borehole sites at C0002 and C0009 of IODP drilling campaigns were operated in the Kumano forearc basin (Saffer et al., 2009; Expedition 314 Scientists, 2009a; Expedition319 Scientists, 2010; Strasser et al., 2014). The site C0002 was logged from seafloor to 1,401 meter below seafloor (mbsf) in the south-east side of the Kumano basin close to the outer ridge penetrated both in gas hydrate and free gas zones. Whereas, the site

C0009 at the landward side of the Kumano forearc basin penetrated in limited zones was logged only from 680 to 1,604 mbsf, but this log provides the *Vs* (Expedition 314 Scientists, 2009a; Expedition319 Scientists, 2010). The *Vs* log is needed for the estimate of *Vs* in the whole study area via pre-stack waveform inversion. Therefore, the logging data at Site C0009 were crucially used in this study to quantify parameters in the Vp/Vs-to-pore-pressure transform using seismic interval velocities correlated with pressure well data such as Modular Dynamic Test (MDT) and Mud Weight (MW) and their *Vp/Vs* for fluid saturation effects and pore pressure discussion. Due to the unlogged section in the shallower and deeper parts of this site, density calculation for the shallow and deep sections was interpolated using the Chapman's equation (Chapman, 1983) and used to estimate the overburden or total stress in the whole depth in this study area.

The seismic data acquisition and processing (i.e automatic velocity analysis) were described in details in the Chapter 2, and the study area is also specified in the Chapter 2 (Figure 2.1). In this study, I used the seismic inline 2528 close to the borehole sites of C0002 and C0009 and the high resolution *Vp* model processed by automatic velocity analysis (Chhun et al., 2018).

3.3 Methodology

This study used high-resolution and accurate 3D velocity data from automatic velocity analysis combined with IODP borehole data at sites C0002 and C0009 acquired in the Kumano forearc basin, off Kii Peninsula, Japan to predict pore pressure and fluid saturation effects in this basin. The *Vs* and pore pressure estimation results at IL2528 were presented in the following two

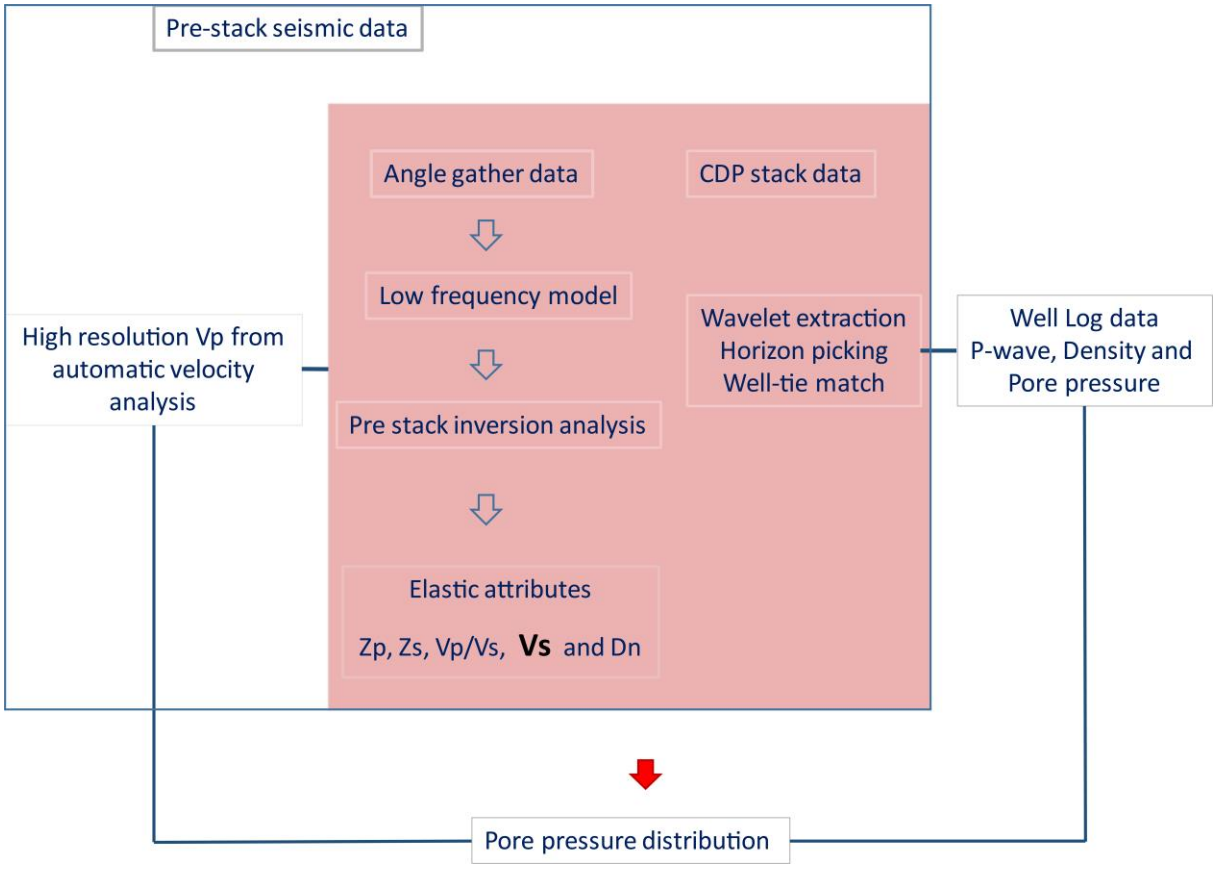

Figure 3.1 Methodological chart for pore pressure prediction and Vp/Vs estimation

steps (Figure 3.1); (1) Initial well analysis for Vp/Vs-to-pore pressure transform before and after gas-corrected effect Vp was made by using the well C00009A before applying with seismic velocity in the whole study area, and (2) estimation of S-wave velocity structure from pre-stack waveform inversion for discriminating pore pressure and fluid saturation effects.

3.3.1 Vp/Vs-to-pore pressure transform

Initial pressure analysis using well data

The drilling site C00002A were logged from the seafloor till 1,401 mbsf; however, it was not composed of *Vs* log. Instead, the drilling site C0009A's petrophysical measurement was logged in limited zone (680-1,601mbsf), but consisted of *Vs* data. Therefore, the C0009A well logs were used in the study area for well pressure calibration with the seismic data to predict pore pressure in the whole study area. The following approach shows a relationship of effective stress, overburden stress and pore pressure via modified Eaton's (1972) *Vp/Vs* equation, which were used to predict pore pressure from abnormal compaction trend (Zhang 2013; Zhang 2014). Especially, gas reservoirs are distributed in our study area (Chunn et al., 2018), and the *Vs* insensitive to gas saturation could be a key information for pore pressure prediction.

Pore pressure formation (fluid pressure in the pore) is function of total stress (or overburden stress) and effective stress based on Tarzaghi's and Biot's effective stress low (Biot, 1941; Terzaghi et al., 1996). This can be expressed as follows:

$$P_f = (\sigma_v - \sigma_e)/\alpha \quad (1)$$

where P_f is the pore pressure; σ_v is the overburden stress; σ_e is the vertical effective stress; α is the Biot effective stress coefficient which is assumed as 1 in low frequency seismic survey. *In situ* stress is influenced by three mutually orthogonal principal stresses such as vertical stress (σ_V), maximum horizontal stress (σ_H) and minimum horizontal stress (σ_h). It is commonly assumed that the formation compaction is mainly caused by the vertical/overburden stress and formation under-compaction is primarily connected to the vertical stress (Chapman, 1983; Osborne and Swarbrick, 1997; Zhang, 2013). Thus, the pore pressure in the formation can be calculated from

the vertical and effective stress by determining the abnormal compaction trend in the above equation.

Vertical stress estimation

Vertical stress is generated by the weight of the overlying formations; thus, vertical stress or overburden stress can be obtained mainly from density log by the following equation:

$$\sigma_v = g\rho_w z_w + g\int_{z_w}^{z} \rho_b(z)dz \tag{2}$$

where $\rho_b(z)$ is the formation bulk density as a function of depth; ρ_w is the average density of sea water; z is the depth from the sea level (or mudline); z_w is the water depth (1936 m in this study area). In most cases, the bulk density log is run through only a specific interval of interest, not representing the whole section. Therefore, the extrapolation of density data for overburden estimation in the unlogged section including shallower and deeper sections can be calculated by Chapman's (1983) function (Zhang, 2011; Zhang, 2013).

The density data at the Site C0009 is extrapolated using Chapman's (1983) equation given below:

$$\rho_b(z) = \rho_m - (\rho_m - \rho_{ml})e^{-cz} \tag{3}$$

where ρ_b is the bulk density; ρ_m is the matrix density or the grain density of the rock; ρ_{ml} is the density at mudline; c is the exponential decline; and z is the vertical depth below the mudline.

$\rho_m = 2.65\ g/cm^3$, $\rho_{ml} = 1.75\ g/cm^3$ were used and $c = 0.0036$ was determined from the depth and density log trend line in this study (Zhang 2011; Zhang 2013).

Hydrostatic pressure calculation

The hydrostatic pressure is the pressure exerted by the static fluid column at a particular depth. It relies on the density of fluid/water in the formation, which usually is brine and the vertical height of the fluid column (Sayers, 2006; Zhang, 2011; Zhang, 2013). Therefore, the hydrostatic pressure P_n can be expressed via the following equation:

$$P_n = g \int_0^h \rho_f(z) dz \tag{4}$$

where g is the acceleration due to gravity; ρ_f is the fluid density (1.024 g/cm^3 used in this study); and h is the vertical height of the fluid column.

Vp/Vs-to-Pore pressure transform

Compressional velocity *Vp* reduction geologically influenced by various factors such as fluid saturation, pore's geometry, lithology, anisotropy, fractures or fluid pressure itself, but *Vs* is not sensitive to fluid saturation and is sensitive to pore pressure (Tsuji et al 2008; Tsuji et al., 2014; Karthikenya et al., 2018). Therefore, to estimate the pore pressure distribution more effectively, the modified Eaton's *Vp/Vs* to predict pore pressure were used (Giao, 2015; Ebrom, 2006; Saleh et al., 2013; Karthikenya et al., 2018; Giao, 2015). The Eaton's method is commonly used in many

oil and gas fields (Zhang, 2011; Zhang, 2013; Kumar et al., 2014; Landrø, 2014). After I conducted well pressure calibration correlated with pore pressure estimation, I applied this relation in the whole study area based on Vp & Vs data.

The pore pressure was calculated by the modified Eaton's (1972) equation as follows:

$$P_f = \sigma_v - (\sigma_v - p_n) \times \left(\frac{Vp/Vs_{normal}}{Vp/Vs}\right)^n \quad (5)$$

Where P_f is pore pressure; n is the Eaton's coefficient which was estimated as 2.0 because it fitted with the well pressure calibration; Vp/Vs is P-wave and S-wave velocity ratio at the target location; and Vp/Vs_{normal} is Vp/Vs in the normally compacted sediments (i.e., no abnormal pressure). This Vp/Vs_{normal} were carefully estimated by considering filtered shale points from the shale base line of gamma ray to present the normally compacted trend in this study area (Figure 3.2, green line on GR log) as the following equation:

$$Vp/Vs_{normal} = -0.0004V_s + 2.9 \quad (6)$$

Vp log used to estimate pore pressure was influenced by amount of gas content (Tsuji et al., 2008) leading to an incorrect estimation of overpressure at the Site C0009 as shown in the red line of Figure 3.2a; therefore a trend line of *Vp/Vs* corrected gas effect (Figure 3.2a, blue log) was determined without considering hydrocarbon zone, and gas corrected *Vp* were defined via this equation:

$$V_p = 0.0004{V_s}^2 + 0.4295V_s + 1446 \quad (7)$$

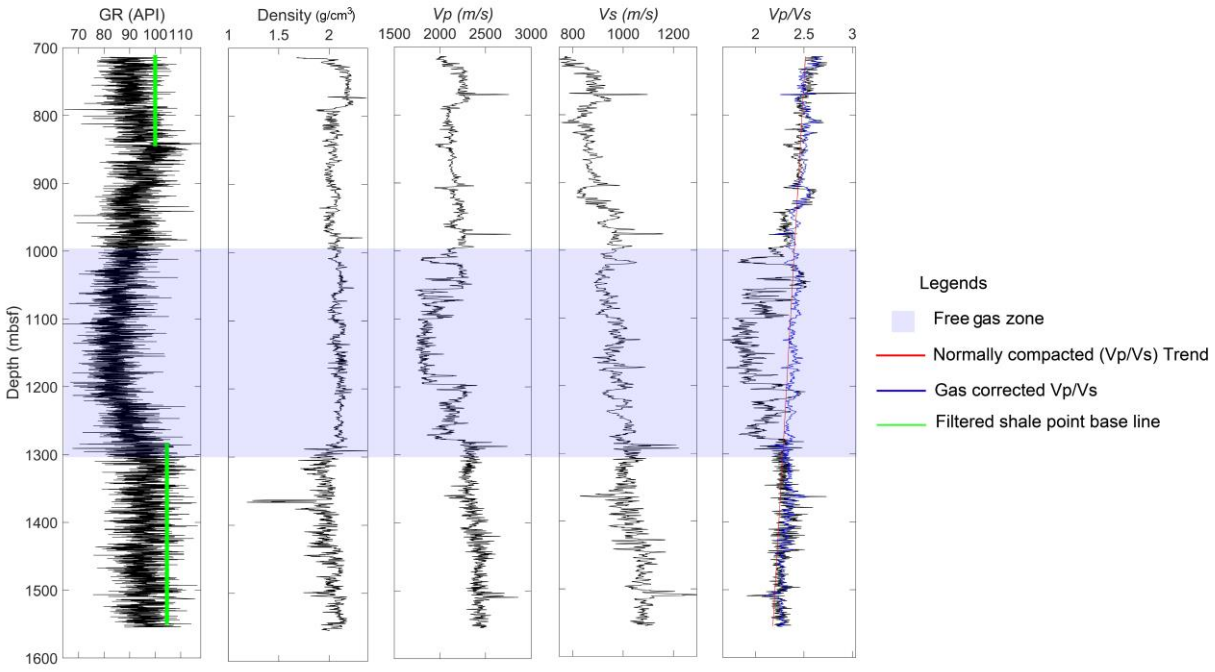

Figure 3.2 Logging data at IODP Site C0009 for Vp/Vs-to-pore pressure transform with pressure well calibrations.

3.3.2 Pre-stack waveform inversion to estimate a high-resolution *Vs* profile

Because *Vp* cannot separate pore pressure anomaly or gas saturation distribution in the reservoirs, *Vs* (or *Vp/Vs* ratio) is used to distinguish them. I estimated high resolution *Vs* from pre-stack inversion using fully-processed seismic profile at IL2528 and logging data at site C0009A.

Simultaneous pre-stack waveform inversion is a sophisticated technique for seismically-derived attributes using angle or offset gathers (Kenejad et al., 2017; Hampson et al., 2005). Using the seismic waveform inversion, *Vs* can be estimated and is in high-resolution, along with a series of elastic parameters (*Vp*, *Vs*, *Vp/Vs*, *P*-wave impedance *Zp*, *S*-wave impedance *Zs*, and Density (*Dn* or ρ), which are not posting inherently like post-stack inversion algorithm. The relationship

between the *Zp* and *Zs* and *Zp* and ρ are expressed by Aki-Richard's equations (Aki and Richards, 1980), and Gardner's equation (Hampson et al., 2005).

I described in the following section how the process performed in the pre-stack inversion using Hampsoon Russell software package (Figure 3.1). This inversion process requires a pre-stack seismic volume of fully processed common-mid point (CMP) gathers, logging data and a set of horizons to guide the interpolation of the initial guess model (Hampson et al., 2005, Kumar et al., 2014, Keynejad et al., 2017).

Initially, the CMP gathers were converted to angle gathers varying between 0 to 40 degree estimated from the velocity field using seismic velocity, and three interpreted stratigraphical horizon cut through the bottom simulating reflectors (BSRs) depth were picked. I selected the well C0009A to do seismic inversion because the *Vs*, *Vp*, and bulk density log were acquired in this well. Near-angle dependent wavelet (1^o-20^o) and far-angle dependent wavelet (20^o-39^o) were extracted to calculate a synthetic trace at this well. Then, a synthetic trace calculated from near-angle-dependent wavelets were used and correlated with composite traces extracted from angle gathers within the cross-correlation window from 3650 to 3850 TWTs in order to obtain the good matching of time-depth relationship (Figure 3.3). However, the synthetic seismogram may not reach the best fit due to the different frequency used in the seismic and borehole data acquisition, the borehole condition and angle measurement in the presence of anisotropy (Hampson et al., 2005, Kumar et al., 2014, Keynejad et al., 2017). In this study, the reflection characteristics of low and high amplitude in the synthetic seismogram generated from the well log data exhibit the matching with the troughs and peaks of the real seismic trace (Figure 3.3b). The synthetics was shifted approximately 10 msec to tie the seismic trace. As a result, the correlation coefficient was equal to about 60%.

a)

b)

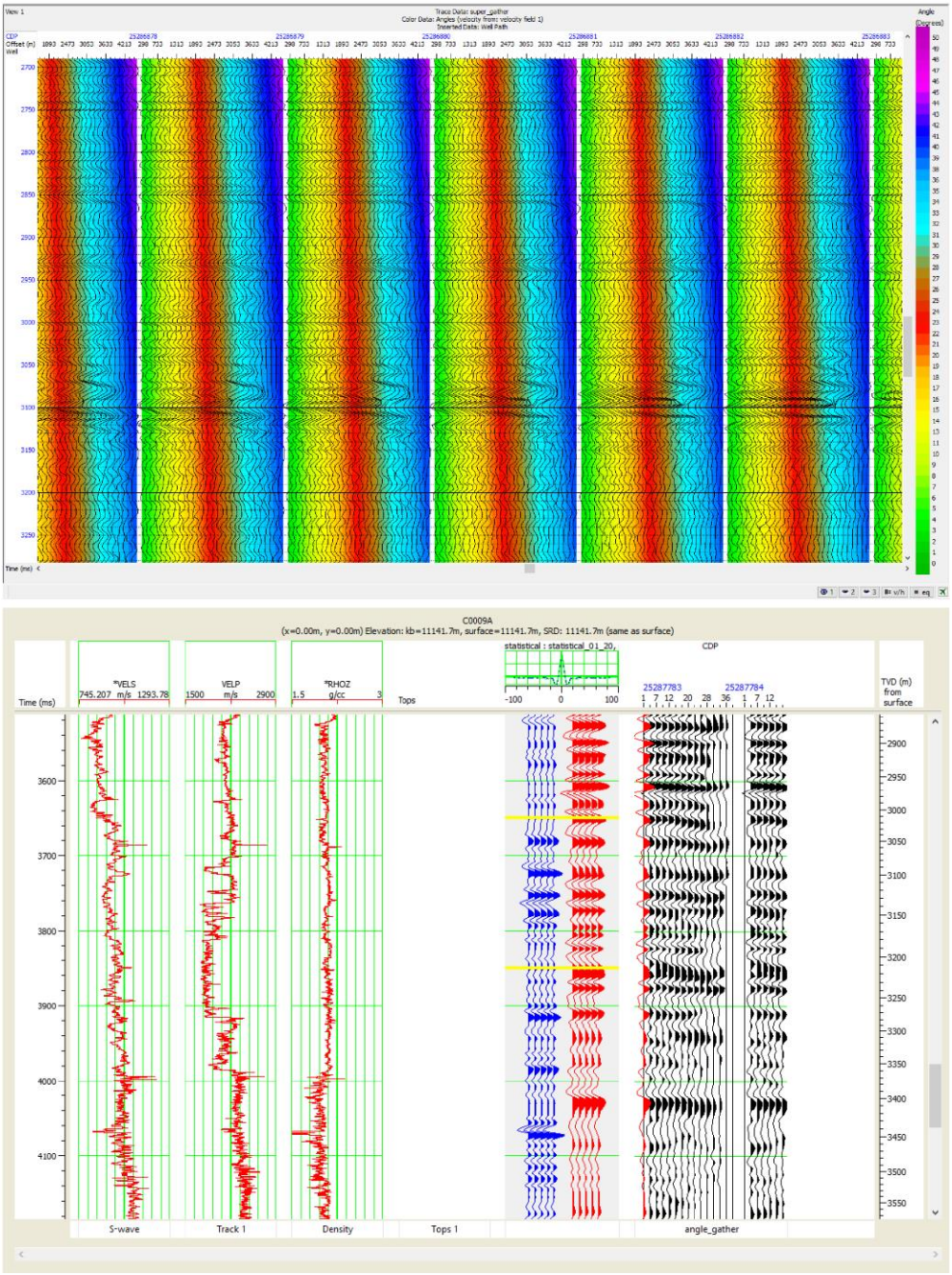

Figure 3.3 a). NMO-corrected CMP gathers whose effective angle range is from 0^o to 40^o (Gathers are colored based on the incident angles). b). Well-seismic tie for well at C0009A shows Vp, Vs, Rho log, synthetic trace (blue) calculated using near-angle-dependent wavelets, and composite traces (red) extracted from angle gathers (black)

The pre-stack waveform inversion depends on model-based inversion. The *Vp, Vs,* and density log were required as an input for initial model (IM) in which initial model values for *Zp, Zs* and ρ as a first guess from which it iterates to a better solution by reducing the misfit. In this regard, the logs were interpolated between wells by interpreted structural horizons and a root mean square (RMS) velocity model as the constraint using squared inverse of distance. After interpolating the well log curves, a low-pass frequency filter was applied to the model which passed all frequencies between 10 Hz and 15 Hz and interpolated the filter between those limits. This process also made IMs for *Zp, Zs and Vp/Vs*. This workflow created *P*-impedance IMs served as the initial guess and the low frequency component added to the band-limited seismic data volume. Algorithm relations of *Zp, Zs* and ρ derived from well logs provided the background trend which were used for the inversion process to reduce the non-uniqueness and detect deviation of variable *Zp, Zs* and ρ from the trend (Hampson et al., 2006; Kumar et al., 2014; Keynejad et al., 2017). After the assigned model and parameters were optimized at the well location, the last step is to apply the inversion process to the entire volume from 2600 to 5000 TWTs. The most wanted attribute is *Vs*. Then it will be used to calculate *Vp/Vs* or Poisson's ratio with the high resolution *Vp* from automatic velocity analysis.

3.4 Results and Discussions

3.4.1 Initial well pressure analysis at the well C0002A and C0009A

As indicated in the Expedition 314 and 319, there is no overpressure zone in the drilling site C0002 and C0009 (Figure 3.4; Expedition 314 Scientists, 2009a, Expedition 319 Scientists, 2010;

Moore et al, 2012; Saffer et al., 2013). Lithofacies, sedimentary facies, stratigraphy and depositional environment between these well correlations as well as overall stratigraphic successions of this forearc basin were dominated by mud with intercalated sand and mud turbidite sediments, underlain by accretionary prism sediments. Hydrate and gas reservoirs were found in sandy areas (Expedition 314 Scientists, 2009a, Expedition 319 Scientists, 2010; Moore et al, 2012; Saffer et al., 2013). The well C0002A penetrated in the gas hydrate zone (218.1 – 400.4m Logging While Drilling depth below seafloor, LSF) and thin gas zone (481.6 – 547.1 m LSF) (detailed petrophysical log analysis in the Chapter 2). Measuring pore pressure in the borehole annulus while drilling was conducted, so called APRS-MWD (Average annular pressure MWD) (Expedition 314 Scientists, 2009a, Moore et al, 2012). Well pressure data such as APRS-MWD, Mud weight (MW), formation fracture pressure (i.e drilling fluids induce fracture in the rock formation at well bore) were presented in this site (Figure 3.4b). APRS-MWD agrees well and parallels with the MW (Figure 3.4b). MW is equal to the hydrostatic pressure condition in the site C0002 (Expedition 314 Scientists, 2009a, Moore et al, 2012). On the other hand, this drilling site was near the outer ridge, and Chhun et al., (2018) found that hydrate was highly concentrated in this area. However, *in situ* pore pressure measurement in gas hydrate bearing and gas zone presented in this well is equal to hydrostatic pressure or quite lower than hydrostatic pressure as measured by APRS-MWD (Figure 3.4b).

The borehole site C0009, 20 km distance from the outer ridge of the 3D seismic area, penetrated in gas zone bearing tourbidite sediments (~1000 – 1300 mbsf). Based on petrophysical log analysis of GR, density, *Vp*, *Vs* and *Vp/Vs* logs, I can identify the distinct zone by observing the low GR (i.e more sand richness), low *Vp* (< 1750 m/s) and particularly low *Vp/Vs* (< 2.2) (thus low Poisson's ratio). These properties suggested the gas saturation zone. The gas zone in the well

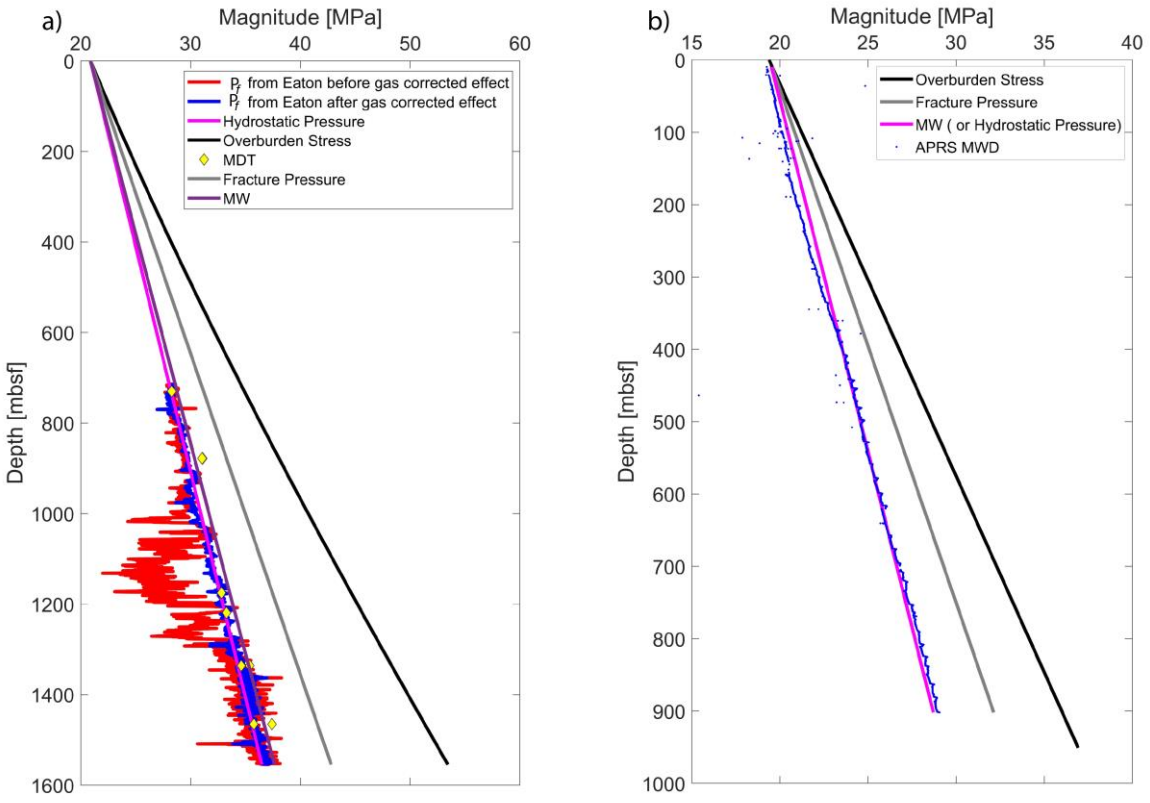

Figure 3.4 Pressure well at the drilling site C0009 and C0002, a) Well pressure data, and pore pressure estimation before and after gas–corrected Vp were estimated at a well C0009A via modified Eaton's Vp/Vs equation, b) Well pressure data at the well C00002A

interval were also confirmed by the core and cutting drilling data of IODP Expedition 319 (Expedition 319 Scientists, 2010; Strasser et al., 2014).

Hydrate and gas are widely distributed in the entire basin (Chhun et al., 2018; Jia et al., 2016; Taladay et al., 2017). Fluid saturation and pore pressure are difficult to estimate separately from only *Vp* when these two mechanical rock properties are acting to minimize *Vp* at the same time. Due to low *Vp/Vs* and low *Vp* trend analyzed in the well C0009 (Figure 3.4), it can suggest the presence of gas saturation, and no overpressured fluids/zones which were also confirmed by the IODP Expedition 319. Conversely excess pore pressure results to the high *Vp/Vs*, and low *Vp* trend

because increase in pore pressure decreases effective stress and also reduces compressional velocity (Tsuji et al., 2008, Tsuji et al., 2014; Maleki et al., 2018). In this regard, *Vs* plays a major role for pore pressure buildup and fluid saturation separation and pore pressure estimation in this well. Hence estimation of pore pressure on this log were adopted with Vp/Vs-to-pore pressure transform calibrated to reservoir pressure data and other well data (i.e Modular Dynamic Test, MDT, and MW) before applying for seismic pore pressure estimation. Mud weight, MDT, and fracture pressure were presented in Figure 3.4a. MDT-single probe test was run to measure *in situ* pore pressure, and fluid mobility, and formation permeability while drilling. According to the IODP Expedition 319, the MW and MDT points of *in situ* pore pressure test are slightly higher than hydrostatic pore pressure and almost fits to hydrostatic pressure gradient (Figure 3.4a).

By Vp/Vs-to-pore pressure transform, I calculated pore pressure before and after gas corrected effect because *Vp* was really influenced by fluid content, pore geometry, pore volume, lithology, anisotropy and fluid pressure itself (Tsuji et al., 2008; Tsuji et al., 2014; Zhang 2011), therefore *Vp* and *Vs* empirical relation were used to correct the *Vp* from gas effect (Equation 7). As a result, before gas correction effect, the pore pressure result was really influenced by gas saturation zone as shown in the red line in Figure 3.4a in which it was significantly underestimated and lower than hydrostatic pressure or MW. After gas corrected *Vp*, the pore pressure estimated by the modified Eaton's *Vp/Vs* equation are corrected and correlated with the *in situ* pore pressure measured by MDT and MW (Figure 3.4a, blue line). Therefore from this relationship I can use this approach to estimate the pore pressure distribution from seismic *Vp* -*Vs* data.

On the other hand, Kumano forearc basin is affected by compressional stress regime. Lateral or tectonic stresses can induce the increase in pore pressure within the sedimentary basin (Kethikenya et al., 2018, Tsuji et al., 2008; Tsuji et al., 2014). On the site C0009A, Leak of Test

(LOT) showed that the least principal stress ($\sigma_3 = \sigma_h$) is lower than vertical stress (σ_V), displayed result with correspondent value to an effective stress ratio (σ'_h/σ'_V=0.44), and the leak-off pressure are 30.22 - 30.25 MPa at the depth of 708.6 mbsf). This implied as an evidence that the overpressure is not able to be generated in this area because overburden load is higher than horizontal compaction where no low permeability barrier, and pore fluids can escape via interconnected column of pore fluid maintaining hydrostatic pressure gradient from the surface to the depth (Expedition 319 Scientists, 2010; Tsuji et al., 2008; Tsuji et al., 2014, Zhang 2011, Karthikeyan et al., 2018). This is also correspondent with seismic profiles showing a series of normal faulting structures. They were caused by the extension normal stress within the basin off the Nankai subduction margin resulted from $\sigma_v > \sigma_H > \sigma_h$ (Tsuji et al., 2014; Jia et al., 2016; Chhun et al., 2018; Taladay et al., 2017).

3.4.2 Fluid saturation effects and pore pressure prediction

I obtained *Vs* profile from pre-stack seismic inversion (Figure 3.5c). Because of a high resolution and accurate *Vp* and fully-processed (normal-moveout-corrected) CMP gathers from automatic velocity analysis, and logging data including *Vp, Vs*, and density, the obtained *Vs* profile via waveform inversion is in high resolution (Figure 3.5c). The presence of gas significantly influenced *Vp*, while *Vs* is insensitive to it, which marks the ratio *Vp/Vs* effective indicators of hydrocarbon reservoir characteristics which was applied to estimate seismic pore pressure in this study area (Figure 3.6) (Keynejad et al., 2018; Landrø, 2014). As a result, *Vp/Vs*-to-pore pressure

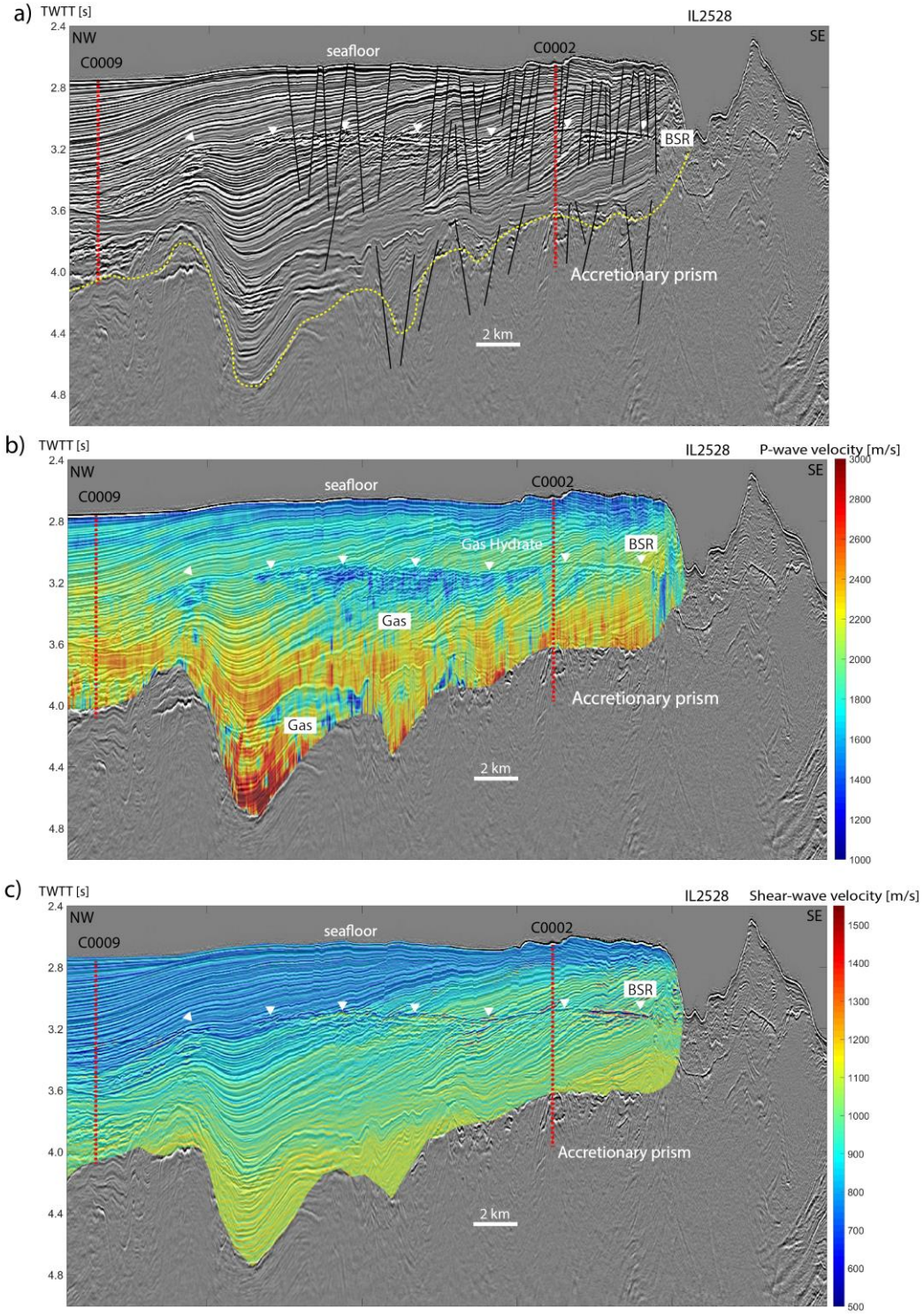

Figure 3.5 Example of Inline 2528 processed from automatic velocity analysis shows structure, BSR, and accumulations of hydrate and gas reservoirs, a). seismic image, b). seismic velocity with low trend (blue) and high trend (yellow), c). Shear-wave velocity (Vs) was estimated from pre-stack waveform inversion

calculation applied in seismic data shows that, before gas-corrected seismic *Vp* profile, the seismic pore pressure distribution is influenced by gas saturated areas which cause the pore pressure is lower than hydrostatic pore pressure (Figure 3.7). After gas-corrected *Vp*, the seismic pore pressure gradient is almost equivalent with the hydrostatic pore pressure gradient from the surface to the depth including hydrate and gas reservoirs, except that pore pressure areas around the Well C0009 and at the BSR depth are slightly greater 1 MPa than hydrostatic pore pressure (Figure 3.8).

In the results of velocity (*Vp* and *Vs*), I interpreted variation of changes in the pore pressure and fluid saturation based on their *Vp/Vs* and *Vp* trend with three location points (Figures 3.6 and 3.9) in this basin filled by dominated mudstone with varying sand and silt turbidite abundance overlying accretionary prism sediments:

1) Location "X" in the landward side (Figure 3.6) shows an increase in *Vp/Vs* and *Vp* trend and the pore pressure also remains in the hydrostatic condition (pore pressure results in the Figure 3.9). This vertical area was interpreted in the normally pressured zone and full-saturated conditions. However, there are some data points in this area with low *Vp/Vs* and *Vp* trend which can indicate the presence of gas content (Figures 3.6-3.9);

2) Location "Y" in Figure 3-6 is situated on the middle study area along the hydrate layer. A lower part of "Y" is correspondent with low *Vp/Vs* and high *Vp* trend in the hydrate zone. Noticeably, the low trend of *Vp/Vs* is dominant toward the outer ridge where it is placed on the highly saturated hydrate area (Chhun et al., 2018). However, an upper part of "Y" shows an increase in *Vp/Vs* and *Vp* trend which can indicate the presence of water-filled sediments rather than hydrate bearing sediments above the BSR (Figures 3.6-3.9);

3) Location "Z" below the BSR (Figure 3.6) is taken along the gas layer which dominantly presents the low trend of *Vp/Vs* and *Vp*. These fluid saturation effects and high pore pressure zone separation can be clearly seen on the clustering plots (Figures 3.9). Qualitatively, *Vp* and *Vp/Vs* profile can tell us different hydrate, gas and overpressured zones in this study area (Figure 3.6 and Figure 3.9).

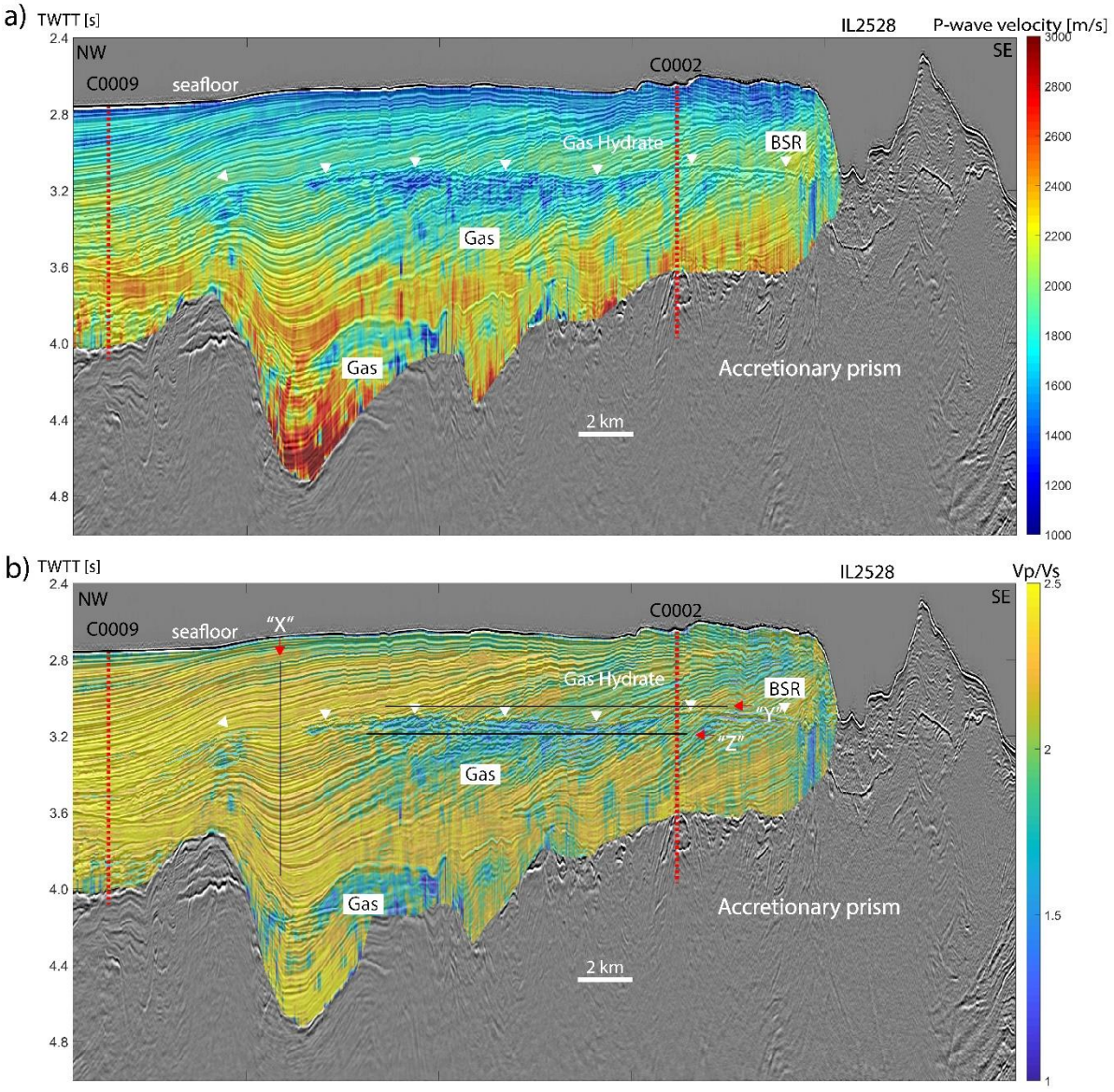

Figure 3.6 a) Seismic interval velocities Vp, b) the result of Vp/Vs ratio was used to determine the effect of saturation and pore pressure change separately. Locations "X", "Y" and "Z" were presented for cluster plots of Figure 3.9

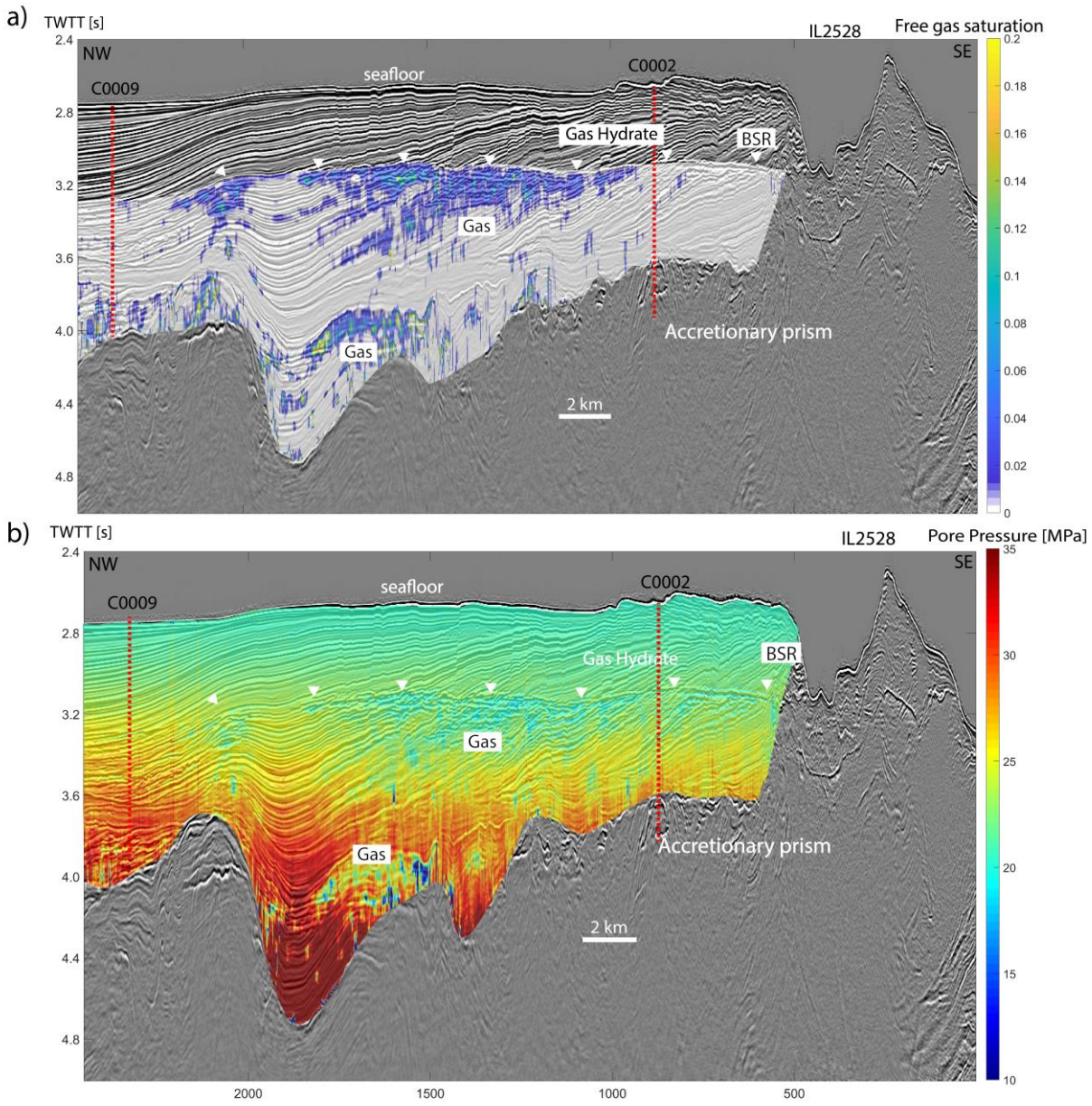

Figure 3.7. Comparison of fluid-saturation and pore pressure change at IL2528, a) free gas saturation profile, b) pore pressure distribution before gas-corrected Vp were underestimated in the gas layers

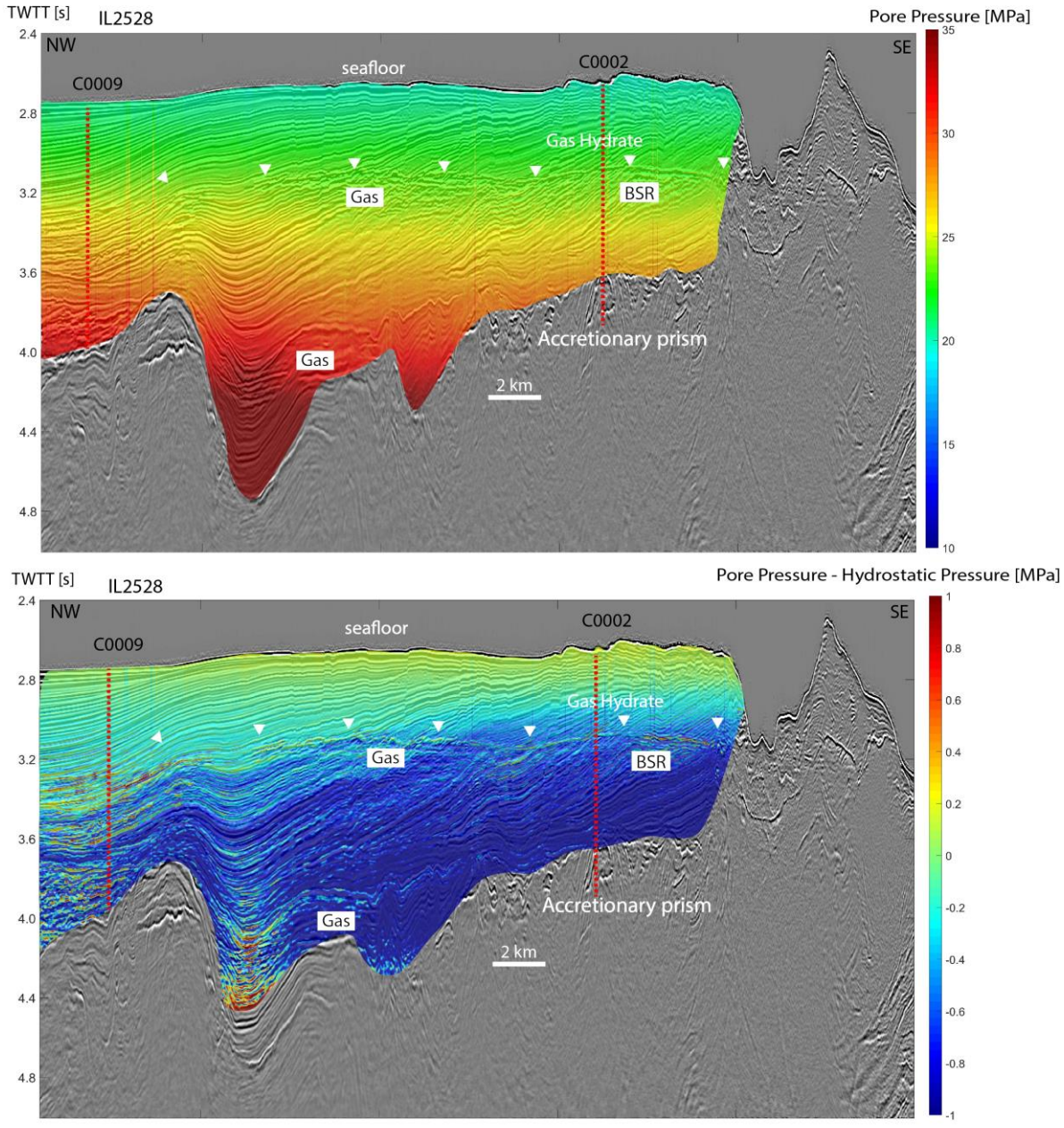

Figure 3.8. a) pore pressure distribution were correctly estimated after removing gas saturation effect, b) a minor pressure difference (0-1MPa) of pore pressure after gas–correct Vp minus from hydrostatic pore pressure

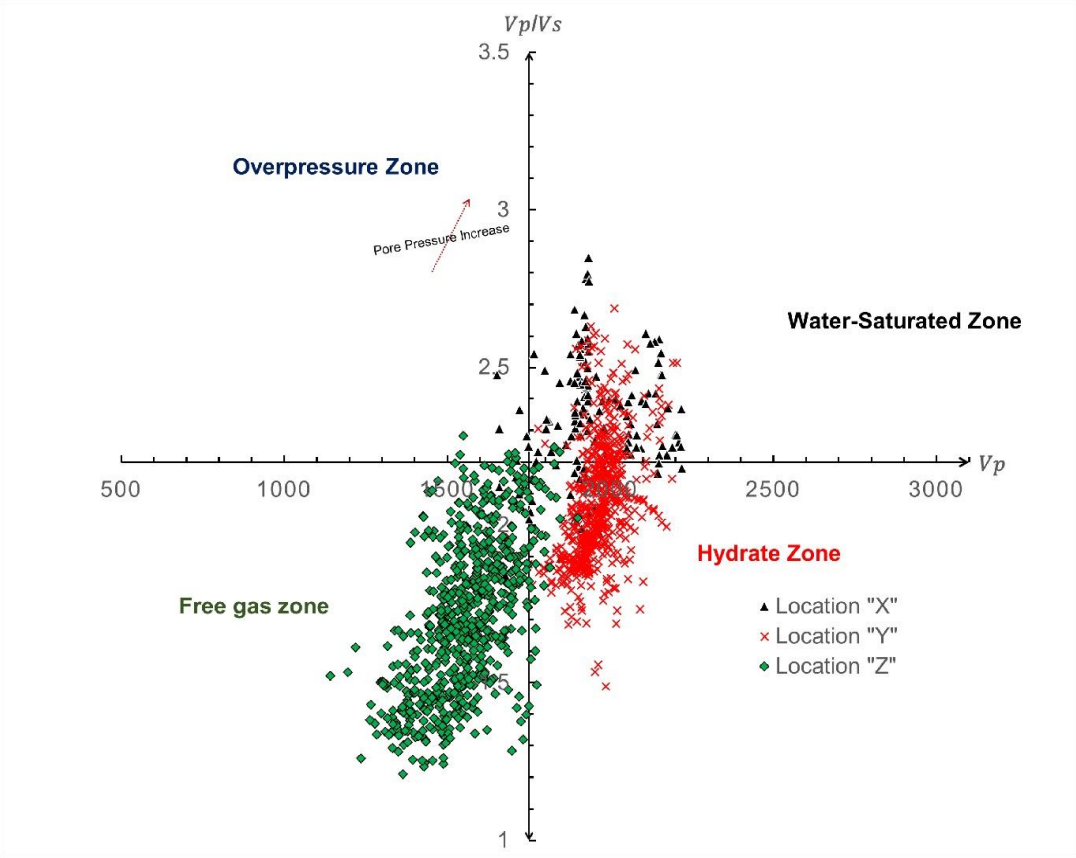

Figure 3.9 Cluster plots of overpressured zone and fluid saturation change zones (original axis: 2.2, 1750m/s). Locations "X", "Y", and "Z" were shown in Figure 3.6

High resolution seismic velocity from automatic velocity analysis (Figure 3.5) shows that widespread hydrate and gas reservoir in this study area. In addition, Chhun et al. (2018) found that in this study area, gas saturation is reached to 20% in the pore volume. However, based on the pore pressure analysis, I presented the gas-uncorrected *Vp/Vs* derived pore pressure result which is lower than hydrostatic pressure or underestimated in the gas saturation zone below hydrate layer and near the base of basin (Figure 3.7). Whereas, after gas-corrected effect *Vp/Vs*, the pore pressure estimation resulted in following with hydrostatic pressure gradient with depth in the whole study area. However, I found a very minor pore pressure increase around the site C0009 which is up to

1 MPa greater than hydrostatic pore pressure or this can be an error in the calculation due to the fitting curves. Moreover, this site was also evidenced by very slightly increased pore pressure test by MDT and MW. The pore pressure seems to be a bit increase as it can be correlated with a higher trend of *Vp/Vs* around this site (Figure 3.6 and 3.9). Interestingly, the pore pressure along the BSR depth has also a subtle increase (0-1MPa higher than hydrostatic pore pressure). The BSRs is a boundary of hydrate and gas layers where temperature and pressure change is at a critical condition for either hydrate formation or dissociation (Chhun et al., 2018; Jia et al., 2016). If gas hydrates are in the dissociation and dissolution phenomena, they generate excess pore pressure and induce the geological hazards (i.e submarine landslides) (Zhang 2011, Kumar et al., 2014; Xu and Germanovich, 2006).

Overall, no overpressure zone or disequilibrium compaction exists in this study and pore pressure distribution in this basin is not affected by compressional tectonic stress in this basin. From the LOT, the horizontal compaction stress is less than vertical compaction stress where this phenomena may not contribute to pore pressure increase (Tsuji et al., 2008; Karthikeyan 2018) even if the sedimentation, stratigraphy and geological settings in this basin is in complex and the presence of high concentrated hydrate and gas distribution. In addition, no excess pore pressure generation may possibly due to the young sedimentation (~1.95 Ma) and low thickness of sediments (1-2km) in the Kumano forearc basin (Taladay et al., 2017), therefore overlying loading stress and horizontal compaction of this compressional tectonic stress in this subduction convergent margins do allow low permeable barriers and fluids can escape and migrate through the connected pore media maintaining the hydrostatic pressure gradient through depth in this basin. Gas dominantly supplied at depth from high pore pressure fluids beneath the basin in accretionary prism released and migrated upward to gas reservoirs where they were trapped and confined by

the hydrate layer (Figures 3.6, 3.8, and 3.9) (Chhun et al., 2018). This implies gas saturation content, lithofacies (i.e mud, silt, and sand intercalations) and sedimentary facies (i.e turbidite deposits), stratigraphic architecture connected to their regional tectonics of this plate convergence do not cause the disequilibrium compaction or generate overpressure fluids in this whole study area (Figures 3.6, 3.8 and 3.9).

3.5 Conclusions

From results of pore pressure prediction, the pore pressure distribution in hydrate and gas layers are remain in hydrostatic pressure condition, and the pore pressure distribution from the surface to the greater depth maintains hydrostatic pressure gradient in the Kumano forearc basin. High pore pressure and fluids were clearly distinguished from the approach via integrating automatic velocity analysis, pre-stack wave form inversion and rock physics. This approach provides new insights into better qualitatively and quantitatively mapping pore pressure distribution in the deep and complex hydrocarbon reservoirs. Outcomes from this research is important for drilling programs of hydrate and gas exploration and extraction in the future as well as understanding the geological processes and deformation processes connected to the sedimentary architecture and evolution of the basin, and its relationship with the intensive tectonic movement in this active subduction margin.

3.6 References

Chhun, C., Kioka, A., Jia, J., Tsuji, T., 2018. Characterization of hydrate and gas reservoirs in plate convergent margin by applying rock physics to high-resolution seismic velocity model. Mar. Pet. Geol. 92, 719–732. https://doi.org/10.1016/j.marpetgeo.2017.12.002

Chapman, R., 1983, Petroleum Geology: Amsterdam, Elsevier, 415 p.

Ebrom, D., Heppard, P., & Albertin, M. (2006, January). Travel-time methods of VP/VS determination for pore-pressure prediction using look-ahead VSPs. In *Offshore Technology Conference*. Offshore Technology Conference. https://doi.org/10.4043/18399-MS

Expedition 314 Scientists, 2009a. Expedition 314 Site C0002. In: Kinoshita, M., Tobin, H., Ashi, J., Kimura, G., Lallemant, S., Screaton, E.J., Curewitz, D., Masago, H., Moe, K.T., the Expedition 314/315/316 Scientists (Eds.), Proceedings of the Integrated Ocean Drilling Program, 314/315/316. Integrated Ocean Drilling Program Management International, Inc., pp. 1–77.

Expedition 314 Scientists, 2009b. Expedition 314 methods. In: Kinoshita, M., Tobin, H., Ashi, J., Kimura, G., Lallemant, S., Screaton, E.J., Curewitz, D., Masago, H., Moe, K.T., the Expedition 314/315/316 Scientists (Eds.), Proceedings of the Integrated Ocean Drilling Program, 314/315/316. Integrated Ocean Drilling Program Management International, Inc., pp. 1–33.

Expedition 315 Scientists, 2009. Expedition 315 Site C0002. In: Kinoshita, M., Tobin, H., Ashi, J., Kimura, G., Lallemant, S., Screaton, E.J., Curewitz, D., Masago, H., Moe, K.T., the Expedition 314/315/316 Scientists (Eds.), Proceedings of the Integrated Ocean Drilling

Program, 314/315/316. Integrated Ocean Drilling Program Management International, Inc., pp. 1–76.

Expedition 319 Scientists, 2010. Expedition 319 summary. In: Saffer, D., McNeill, L., Byrne, T., Araki, E., Toczko, S., Eguchi, N., Takahashi, K., the Expedition 319 Scientists (Eds.), Proceedings of the Integrated Ocean Drilling Program 319. Integrated Ocean Drilling Program Management International, Inc., pp. 1–46.

Giao, P. H., & Anh, T. N. (2015, June). Prediction of Geopressure for a New Exploration Well Site in the Cuu Long Basin, Vietnam. In *77th EAGE Conference and Exhibition 2015*. DOI: 10.3997/2214-4609.201413298

Hampson, D.P., Russell, B.H., Bankhead, B., 2005. Simultaneous inversion of pre-stack seismic data 1633–1637. https://doi.org/10.1190/1.2148008

Ito, T., Komatsu, Y., Fujii, T., Suzuki, K., Egawa, K., Nakatsuka, Y., Konno, Y., Yoneda, J., Jin, Y., Kida, M., Nagao, J., 2015. Lithological features of hydrate-bearing sediments and their relationship with gas hydrate saturation in the eastern Nankai Trough, Japan. Mar. Pet. Geol. 66, 368–378. http://dx.doi.org/10.1016/j.marpetgeo.2015.02.022.

Jia, J., Tsuji, T., Matsuoka, T., 2017. Gas hydrate saturation and distribution in the Kumano Forearc Basin of the Nankai Trough. Explor. Geophys. 48, 137–150. https://doi.org/10.1071/EG15127

Karthikeyan, G., Kumar, A., Shrivastava, A., Srivastava, M. 2018. Overpressure estimation and productivity analysis for a Marcellus Shale gas reservoir, southwest Pennsylvania: A case study. The Leading Edge, 37(5), 344-349. https://doi.org/10.1190/tle37050344.1

Keynejad, S., Sbar, M.L., Johnson, R.A., 2017. Comparison of model-based generalized regression

neural network and prestack inversion in predicting Poisson's ratio in Heidrun Field, North Sea. Lead. Edge 36, 938–946. https://doi.org/10.1190/tle36110938.1

Kumar, D., Chatterjee, R., Sen, M.K., Sain, K., 2014. Pore pressure prediction in gas-hydrate bearing sediments of Krishna – Godavari basin , India Pore pressure prediction in gas-hydrate bearing sediments of Krishna – Godavari basin , India. https://doi.org/10.1016/j.margeo.2014.07.003

Landrø, M., 2014. Discrimination between pressure and fluid saturation changes from time lapse data Discrimination between pressure and fluid saturation changes from time-lapse seismic data. https://doi.org/10.1190/1.1444973

Moore, G.F., Boston, B.B., Strasser, M., Underwood, M.B., Ratliff, R.A., 2015. Evolution of tectono-sedimentary systems in the Kumano basin, Nankai Trough forearc. Mar. Pet. Geol. 67, 604–616. http://dx.doi.org/10.1016/j.marpetgeo.2015.05.032.

Moore, G.F., Park, J.O., Bangs, N.L., Gulick, S.P., Tobin, H.J., Nakamura, Y., Sato, S., Tsuji, T., Yoro, T., Tanaka, H., Uraki, S., Kido, Y., Sanada, Y., Kuramoto, S., Taira, A., 2009. Structural and seismic stratigraphic framework of the NantroSEIZE Stage 1 transect. In: Kinoshita, M., Tobin, H., Ashi, J., Kimura, G., Lallemant, S., Screaton, E.J., Curewitz, D., Masago, H., Moe, K.T., the Expedition 314/315/316 Scientists (Eds.), Proceedings of the Integrated Ocean Drilling Program 314/315/316. Integrated Ocean Drilling Program Management International, Inc., pp. 1–46.

Moore, J.C., Chang, C., McNeill, L., Thu, M.K., Yamada, Y., Huftile, G., 2011. Growth of borehole breakouts with time after drilling: implications for state of stress, NanTroSEIZE transect, SW Japan. Geochem. Geophys. Geosystems 12 (4).

http://dx.doi.org/10.1029/2010GC003417.

Pape, T., Geprags, P., Hammerschmidt, S., Wintersteller, P., Wei, J., Fleischmann, T., Bohrmann, G., Kopf, A.J., 2014. Hydrocarbon seepage and its sources at mud volcanoes of the Kumano forearc basin, Nankai Trough subduction zone. Geochem. Geophys. Geosystems 15, 2180–2194. http://dx.doi.org/10.1002/2013GC005057.

Saleh, S., Williams, K., & Rizvi, A. (2013, May). Predicting subsalt pore pressure with Vp/Vs. In *Offshore Technology Conference*. Offshore Technology Conference. https://doi.org/10.4043/24157-MS

Sayers, C.M., Johnson, G.M., Denyer, G., 2002. Predrill pore-pressure prediction using seismic data. Geophysics 67, 1286–1292. https://doi.org/10.1190/1.1500391

Saffer, D., McNeill, L., Araki, E., Byrne, T., Eguchi, N., Toczko, S., Takahashi, K., the Expedition 319 Scientists, 2009. NanTroSEIZE Stage 2: NanTroSEIZE Riser/riserless Observatory. Integrated Ocean Drilling Program Expedition 319 Preliminary Report. pp. 1–83.

Sloan Jr., E.D., Koh, C., 2007. Clathrate Hydrates of Natural Gases, third ed. CRC Press.

Strasser, M., Dugan, B., Kanagawa, K., Moore, G.F., Toczko, S., Maeda, L., Kido, Y., Moe, K.T., Sanada, Y., Esteban, L., Fabbri, O., Geersen, J., Hammerschmidt, S., Hayashi, H., Heirman, K., Hupers, A., Jurado Rodriguez, M.J., Kameo, K., Kanamatsu, T., Kitajima, H., Masuda, H., Milliken, K., Mishra, R., Motoyama, I., Olcott, K., Oohashi, K., Pickering, K.T., Ramirez, S.G., Rashid, H., Sawyer, D., Schleicher, A., Shan, Y., Skarbek, R., Song, I., Takeshita, T., Toki, T., Tudge, J., Webb, S., Wilson, D.J., Wu, H.- Y., Yamagushi, A., 2014. Site C0002. In: Strasser, M., Dugan, B., Kanagawa, K., Moore, G.F., Toczko, S., Maeda, L., the

Expedition 338 Scientists (Eds.), Proceedings of the Integrated Ocean Drilling Program, 338. Integrated Ocean Drilling Program, pp. 1–248.

Taladay, K., Boston, B. and Moore, G., 2017. Gas-in-place estimate for potential gas hydrate concentrated zone in the Kumano Basin, Nankai Trough Forearc, Japan. *Energies*, *10*(10), p.1552. https://doi.org/10.3390/en10101552

Tsuji, T., Tokuyama, H., Costa Pisani, P., Moore, G. 2008. Effective stress and pore pressure in the Nankai accretionary prism off the Muroto Peninsula, southwestern Japan. Journal of Geophysical Research: Solid Earth, 113(B11). doi:10.1029/2007JB005002

Tsuji, T., Kamei, R., Pratt, R.G., 2014. Pore pressure distribution of a mega-splay fault system in the Nankai trough subduction zone: Insight into up-dip extent of the seismogenic zone. Earth Planet. Sci. Lett. 396, 165–178. https://doi.org/10.1016/j.epsl.2014.04.011

Xu, W., Germanovich, L.N., 2006. Excess pore pressure resulting from methane hydrate dissociation in marine sediments: A theoretical approach. J. Geophys. Res. Solid Earth 111, 1–12. https://doi.org/10.1029/2004JB003600

Zhang, J., 2013. Effective stress, porosity, velocity and abnormal pore pressure prediction accounting for compaction disequilibrium and unloading. Mar. Pet. Geol. 45, 2–11. https://doi.org/10.1016/j.marpetgeo.2013.04.007

Chapter 4

Sound speed of thermohaline fine structure in the Kuroshio Current inferred from automatic sound speed analysis

Abstract

Fine-scale thermohaline structure within ocean column can be mapped seismically in the Kuroshio Current, off the Muroto Peninsula of Shikoku Island, Japan. In this paper I present the application of automatic sound speed picking analysis to the MCS (Multi-Channel Seismic) reflection data acquired in different period to estimate time-lapse sound speed distribution across the Kuroshio Current. This method is based on an optimal velocity trajectory solving by the eikonal equation with a finite difference algorithm. In contrast to seismic inversion technique, this automatic analysis enables us to obtain contrast sound speed profiles without heavily dependency on sound speed or temperature data directly measured at discrete locations. As a result, this method

can visualize sound speed profiles of fine-scale thermohaline structure developed at interleaving or diapycnal mixing processes of different water masses in the Kuroshio Current. The images of all profiles distinguish water masses and their fine-scale internal structure such as cold and warm water eddies, thermohaline staircases, and internal waves mapped from automatic sound speed analysis revealing acoustic contrasts at interfaces across where sound speed and temperature change. Applying our approach for individual seismic line acquired in different time-steps for 3D seismic data can provide time-space variant images of fine-scale thermohaline structure for studies of oceanographic processes as well as large-scale ocean current and climate systems.

KEYWORDS: fine structure, automatic sound speed picking, thermohaline, oceanographic processes, time-space variant images, Kuroshio Current

4.1 Introduction

Physical oceanographic processes strongly affect the global ocean and climate systems. Ocean at present time has uptaken heat more than previously estimated according to a new finding research conducted by Resplandy et al. (2018). They also found that ocean heating (i.e., climate change) outgassing O_2 and CO_2 is naturally indirect from cause of anthropogenic emissions. When ocean gets warmers, there are many potential implications involved physically and biologically such as sea level rising due to thermal expansion in ocean, more coral reef dying, changes in storm patterns (more powerful and frequent storms), increased melting of sea ice, altered ocean currents, decreasing surface oxygen concentrations, and fishery problems (National Ocean Service, 2018; Bijma et al. 2013; Marshall and Zanna 2014). The ocean and atmosphere are close-related due to their carry of heat capacity, therefore physical oceanographic processes in the ocean circulation play a very important role in accountability of change in climate systems (Buffett and Carbonell, 2011; Resplandy et al. 2018).

Contrasting temperature and salinity in the ocean due to lateral intrusions or double-diffusive processes of different water masses produce fine-scale thermohaline structure (Holbrook et al. 2019; Sheen et al. 2012; Nakamura et al. 2006; Holbrook and Fer 2005; Tsuji et al. 2005; Buffett et al. 2017; Nandi et al. 2004; Holbrook et al. 2012; Lee and Richards 2004; Biescas et al. 2010; Sallares et al. 2013; Gorman et al. 2018). This form of double diffusion (salt-fingering) occurs where a warm saline water mass lies above a fresh cold water mass in which this process results to horizontal layers like staircase shapes at the interface where strong thermohaline gradient of temperature and salinity contrasts (Buffett et al. 2017; Holbrook et al. 2012; Tsuji et al. 2005; Nakamura et al. 2006; Gorman et al. 2018). Fine-scale thermohaline structure is commonly

mapped by instruments that measure depth profiles of temperature and salinity at discrete locations, e.g., CTD (Conductivity, Temperature, and Depth). However, such technique has a limitation. To better understand over large-scale processes of thermohaline circulation in the ocean, MCS reflection data have been coupled with hydrographic data (Nakamura et al. 2006; Buffett et al. 2017; Gorman et al. 2018; Papenberg et al. 2010; Páramo and Holbrook 2005; Holbrook, Fer, and Schmitt 2009; Nandi et al. 2004; Dagnino et al. 2016; Sheen et al. 2012; Stranne et al. 2017).

Due to the enormous time involved in oceanographic processes, seismic oceanography has taken the most attention in study of oceanographic processes in the wide range scale, providing the detail horizontal resolution compared to in situ probes, and the screen shot of ocean flow visualization, and their internal structures in space and time. It is therefore important for ocean-climate research (Buffett and Carbonell, 2011; Holbrook et al. 2012; Tsuji et al. 2005; Buffett et al. 2017; Gorman et al. 2018). Seismic oceanography using low-frequency acoustic reflection method was developed and investigated in ocean fine structure based on laterally coherent reflectance occurrence as a result of relatively abrupt change in acoustic impedance defined as the product of sound speed and water density with depth (Wood et al. 2008; Gorman et al. 2018; Fortin and Holbrook 2009; Holbrook et al. 2012; Buffett et al. 2017). This controls the amplitudes of seismic reflection of thermohaline fine structure. Impedance changes due to thermohaline contrast from the lateral isopycnal advection giving the nature of horizontal or subhorizontal reflection of ocean fine layer geometry, which is not required for the application of seismic migration methods, and out-of-plane reflectivity consideration (Gorman et al. 2018).

The Kuroshio Current is one of the major currents in the western Pacific Ocean, which flows to east of Taiwan and extends northeastward along the coast of southern Japan (Figure 4.1) (Tsuji et al. 2005; Nagai et al. 2019; Nakamura et al. 2006). This current has been named as a “black

current" in Japan due to its carry of a large amount of nutrient in dark subsurface water layer along the southern coast of Japan compared to other surrounding current (Nagai et al. 2019). Regional hydroclimate in East Asia and upper ocean thermal structure are strongly affected by warm Kuroshio Current (Li et al. 2017). In addition, a recent study found that Kuroshio Current flows induces forceful turbulent dissipation rate and diffusivity in subsurface water layers (Nagai et al. 2019). The Kuroshio Current has drawn a lot of attentions and researches due to its dynamical oceanographic processes which affect ocean current and climate system (Li et al. 2017). Therefore, there have been many previous studies in the Kuroshio Current using *in situ* intermittent probe tools, satellite images, and numerical model (Tsuji et al. 2005; Nakamura et al. 2006; Minato et al. 2009; Zhu et al. 2019; Nagai et al. 2009, 2012, 2015, 2019). Seismic Oceanography has been recently an advanced tool to study physical oceanographic processes over a large scale providing the detailed horizontal resolution 100 times better than *in situ* probes (Holbrook et al. 2012; Buffett et al. 2017; Lee and Richards 2004; Biescas et al. 2010; Gorman et al. 2018). There are a few studies of Kuroshio Current using seismic oceanography technique. For example, Tsuji et al. (2005) presented the oceanographic seismic images of thermohaline fine structure in time variation of the Kuroshio Current. Nakamura et al. (2006) studies thermohaline fine structure in the Kuroshio Current extension front using simultaneous seismic oceanography and physical hydrophobic data. Minato et al. (2009) studied a 2D detail temperature distribution in the Kuroshio Current using an inversion method to multi-channel seismic reflection data. Therefore, it is important to investigate and reveal ocean fine structure sound speed of Kuroshio Current in time-space variation to visualize ocean flow model or physical oceanographic processes through time. This study can furthermore allow us to better understand this influential current in more detail.

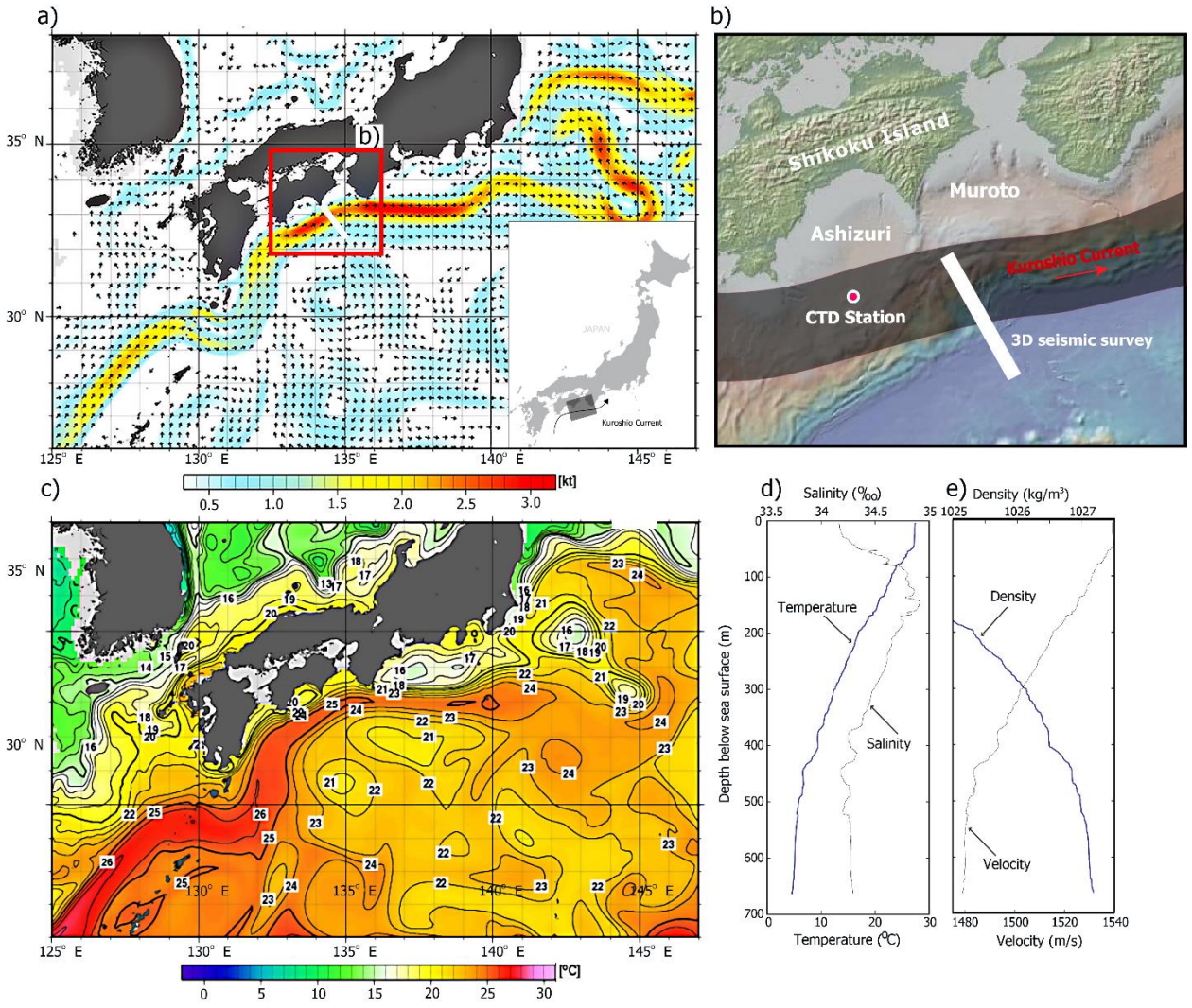

Figure 4.1. Study area a) surface flow map in the Kuroshio Current by 10-day mean currents for 21-30 June, 1999 (unit: 1 knot ≈ 0.5 m / s, which is described as kt), b) A large section from a red box in a) shows a bathymetric map of the Nankai Trough area including Shikoku Island and southwestern Japan. White rectangular box represents 3D seismic survey, and white red circle is the location of CTD station, c) Seawater temperature distribution of 50m in depth from sea surface by 10-day mean temperature for 21-30 June, 1999, d) Temperature and salinity obtained from CTD data off the Ashizuri Peninsula on September 17, 1994 (Tsuji et al. 2005), e) acoustic velocity and density calculated from temperature and salinity in d) (Tsuji et al. 2005).

Ocean current is in motion due to dynamic mixing processes of small-scale and short-lived water mass variation, which gives uncertainty for seismic oceanography (Buffett et al. 2017; Tsuji et al. 2005; Nakamura et al. 2006; Yamashita et al. 2016). Eighty-one individual pre-stack seismic data for 3D data analysis acquired in different days (from 20 June to 15 August 1999) can give us insights to understand extensive thermohaline internal structure as a time-space variation in the Kuroshio Current (Figure 4.1). Here I used the same data as Tsuji et al. (2005) which studied two-dimensional mapping of fine structures in the Kuroshio Current using seismic reflection data. In this study I will emphasize the methods of automatic sound speed analysis in this same study area to reveal the thermohaline fine structure sound-speed in variation of space-time. Because of this analysis, I can quantify sound speed in the ocean without time-intensive processes and relying on oceanographic data which is normally widely spaced and temporally isolated probes. In addition, based on our results, I can interpret/discuss/provide insights of the unique characteristics of reflectivity within ocean and their internal structure corresponding to time-space sound speed variation across the Kuroshio Current. The automatic sound speed analysis has been applied to investigate seismic velocity anomalies of small-scale geological structure, such as gas pockets and reservoirs, which directly inferred from amplitude reflection processing (e.g., Chhun et al. 2018).

4.2 Data and Methods

Eighty-one lines of MCS reflection data designed for 3D coverage was acquired by RV Maurice Ewing in 1999 (Moore et al. 2001). These data, which were originally collected and configured for the subsurface geologic structure, produced detailed characteristics of the thermohaline fine structure in the Kuroshio Current of Japan (Figure 4.1). All individual lines with a cross-track spacing of 100 m were surveyed over an 80 km x 8 km area. All of lines with their

strike of 314^{o} are almost perpendicular to the Kuroshio Current flow direction. The MCS acquisition was configured with towed impulsive airgun sources which total 70 liters cabled with arrays of 14 airguns. The hydrophone cable is 6000 m long hosted by arrays of 240 channels at an interval of 25 m. The acoustic velocity in seawater is ~1500 m/s and the dominant frequency in this time-lapse seismic survey is ~35 Hz. Therefore, the dominant wavelength is equal to 43 m in which the vertical seismic resolution of fine structure layers can be detected >~ 10 m in thickness (Tsuji et al. 2005). The Kuroshio Current had a strong flow speed from 0.5 to 1.5 m/s, which travelled across the entire survey area (8 km) between 1.5 and 4.5 hours, and less than the acquisition time of each line (Figure 4.1a) (Tsuji et al. 2005). All MCS reflection lines in this study area along the Muroto Transect were surveyed over the water depth ranging from 1.5 to 5.5 km, and showed the subsurface complex structure of out-of-thrust faults, bottom-simulating reflectors (i.e. hydrate bottom layer), accretionary prism, and deep plate boundary décollement (Moore et al. 2001). For this study, I presented only results from seismic profiling within an water layer interval of 1 km depth from sea surface at lines 140, 142, 164, and 143 in 200 m, 2200 m, 2100 m, apart acquired in 26th, 28th June, and 09th, 12th July 1999, respectively.

Seismic data processing includes 20-100 Hz band-pass filtering, deconvolution, automatic sound speed analysis, and stacking, which reveals structure in the water column. The speed of sound varying between about 1470 m/s and 1530 m/s in the ocean allows the seismic method to detect the small changes of ocean internal structures (Holbrook et al. 2012). Automatic sound speed analysis is the foremost implementation presented in this paper (Figure 4.2). I applied NMO (normal move-out) based sound speed analysis via AB semblance within 0-2 s time window and 1 km near-offset data of our time lapse MCS seismic data where ocean acoustic reflectivity

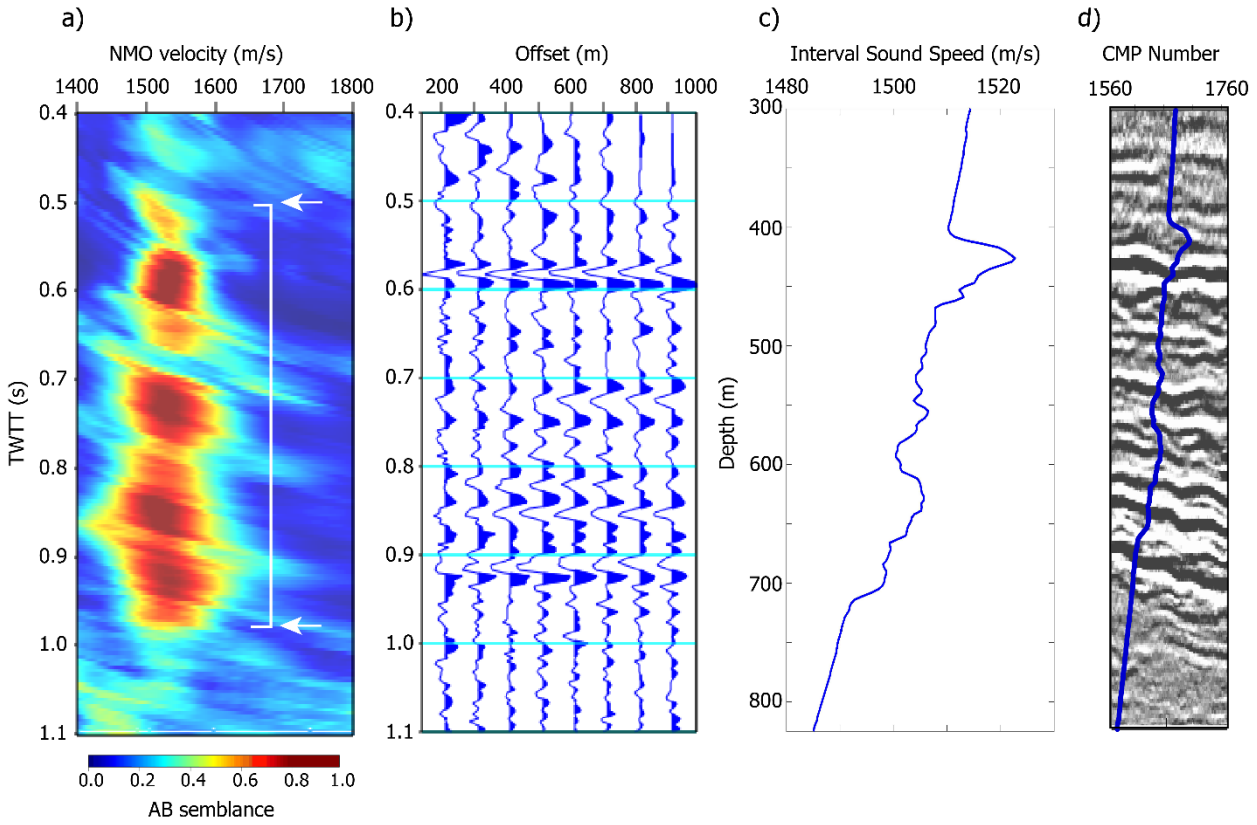

Figure 4.2. NMO-based sound speed analysis, a) AB semblance map via automatic sound speed analysis, b) NMO-corrected CMP gather 1660 of line 142 via AB semblance analysis located in Figure 4.3b (red inverted triangle), c) vertical profile of interval sound speed at CMP gather 1660, d) vertical sound speed profile of CMP gather 1660 overlaps with the MCS reflection image.

existed. AB semblance (=Amplitude Versus Offset (AVO) semblance) is defined as a correlation with a trend of CMP gathers in the velocity analysis (Fomel 2009; Deng et al. 2016). This semblance method is applicable in the presence of strong amplitude variations, polarity reversals (i.e. identify AVO class II sand), and also used for the enhancement of signal-to-noise ratio (SNR) in seismic data processing and imaging to capture the true locations of weak reflections (Fomel 2009; Deng et al. 2016). After I applied this semblance analysis, I carried out automatically picking optimum sound speeds at the peak semblance panel produced by the known surface sound speed of 1530 m/s with the sound speed step in detailed picking of 1 m/s (i.e. normally picking velocity

of 10 m/s in subsurface formations). Every picked CMP (common-midpoint) (trace spacing of 12.5 m) was executed without applying lateral and vertical smoothening. The application of automatically picking velocity algorithm is effective and refrained from time-consuming process, the false errors and larger velocity uncertainties compared to conventional seismic velocity analysis (Fomel and Landa 2014). In addition, I did not apply migration as our interval of interest is within ocean column from 0.0-2.0 s TWT (two-way travel time). To avoid strong Kuroshio surface current (so-called "feathering effects"), I used a near-offset streamer data (~1 km). A far-offset data (> 1 km) or overall offset data (6 km) was strongly deviated from the true reflection locations and influenced by the strong current of Kuroshio Current, flowing perpendicular to this seismic survey area (Tsuji et al. 2005). In addition, selection of this 1 km near-offset data was also because of its high-quality and better preservation of useful energy, which resulted to improvement of velocity analysis as well as random noise attenuation (Deng et al. 2016). Therefore, 1 km near-offset streamer data is thus considered as the optimum one for this analysis. Though 0-0.4s reflection layer (0-300 m below sea surface) is dominant of artifact of direct wave, and no strong reflectors at greater depth in the seawater (>1.1 s, equivalent to >825 m), automatic analysis is sensitive to pick those sound speeds leading to inaccuracy of sound speed analysis (Figure 4.2). Therefore, I focused on 0.4-1.1 s in this study.

I obtained accurate RMS sound speed in the interval of 0.4-1.1 s from automatic seismic sound speed analysis. The extracted RMS sound speed was filtered by high semblance value greater than 0.75 (Figure 4.2a) and disregarded by low semblance value. Then low semblance areas within the ocean fine structure interval, the overlying, and underlying layers of this interval of interest were used to obtain reliable RMS sound speed in the entire water column based on linear interpolation algorithm, which were then calculated into interval sound speed profile via Dix's

equation (Dix 2002) (Figure 4.2c). In this regard, I also implemented smoothening by triangle filtering to our interval sound speed profiles (Fomel, 2009). The triangle filtering is one of the most useful tools in seismic data processing and imaging, and it is based on the filter of equation giving a moving average under a rectangular window done twice similar to Gaussian filtering approach (Claerbout and Fomel 2004). In this case, I applied this smoothing application operated over a radius of 5 vertical traces (4 ms time interval), and 150 horizontal traces (12.5 m trace spacing). Because of the accurate extracted sound speed for stacking, interpolation algorithm and triangle smoothing, the reflection and sound speed images are also enhanced (Figure 4.3).

4.3 Results and Discussions

4.3.1 Internal structure in the Kuroshio Current

Nagai et al. (2019) found that Kuroshio Current flows induced dynamic turbulent dissipation rate and diffusivity in subsurface water layers. Kuroshio Current has carried warm and strong current flow in the western Pacific Ocean resulted to diapycnal mixing processes of different water masses giving acoustic contrasts of water reflectivity. This acoustic contrast created ocean thermohaline fine structure in the seawater which can be mapped by seismic reflection (Figure 4.1) (Tsuji et al. 2005; Nakamura et al. 2006; Minato et al. 2009). Previous studies also confirmed that the ocean thermohaline fine structure caused by double diffusive convection of different water mass mixing using seismic oceanography and in situ probe data (Tsuji et al. 2005; Nakamura et al. 2006; Minato et al. 2009). Therefore, it is essential to investigate time-space variation sound speed without relying on *in situ* probe data which I can see a whole view of water dynamics mixing

processes over the large scale, and understand ocean thermohaline circulation across the Kuroshio Current.

This study presents the first application of automatic sound speed analysis across the Kuroshio Current to acquire sound speed models. This method implies the ability of advanced seismic reflection processing via automatic picking algorithm to remotely estimate sound speed profiles over a large scale of the ocean without using hydrographic data in the process. The analysis of CMP gather 1660 (Figure 4.2, located at a red inverted triangle in Figure 4.3b) at the interval of 0.4-1.1 s exhibits high semblance value and primary reflections in the upper part of seawater (white arrows, Figure 4.2a,b). In addition, the NMO corrected CMP gather 1660 using AB semblance map via automatic sound speed analysis displays high correlation reflections (Figure 4.2a,b) with variation of interval sound speed (Figure 4.2c,d). This high correlation of reflectance in the water column can be due to changes in temperatures and salinity contrast in density and/or sound speed which allows us to detect seismic reflection of fine structure in this seawater (Figure 4.2c,d) (Holbrook et al. 2012; Tsuji et al. 2005; Nakamura et al. 2006; Papenberg et al. 2010; Buffett et al. 2017). Deeper than 1.1s TWT (~825 m), strong reflection no longer exists and internal reflectance progressively become weaker at greater depth, which indicates minor contrasting water masses owing to inconsiderable thermohaline gradients of temperature and salinity change (Figure 4.3).

Herein time lapse seismic profiling of Lines 140, 142, 164, and 143 depicts interesting features of the Kuroshio current's thermohaline internal structure in Figure 4.3 such as thermohaline staircases or layering fine structure (white arrows), water core eddy (black arrows), and internal waves (blue arrows) interpreted in details hereafter. By automatically dense picking processing (1 m/s) for all CMP gathers, I obtained seismic images of Kuroshio thermohaline

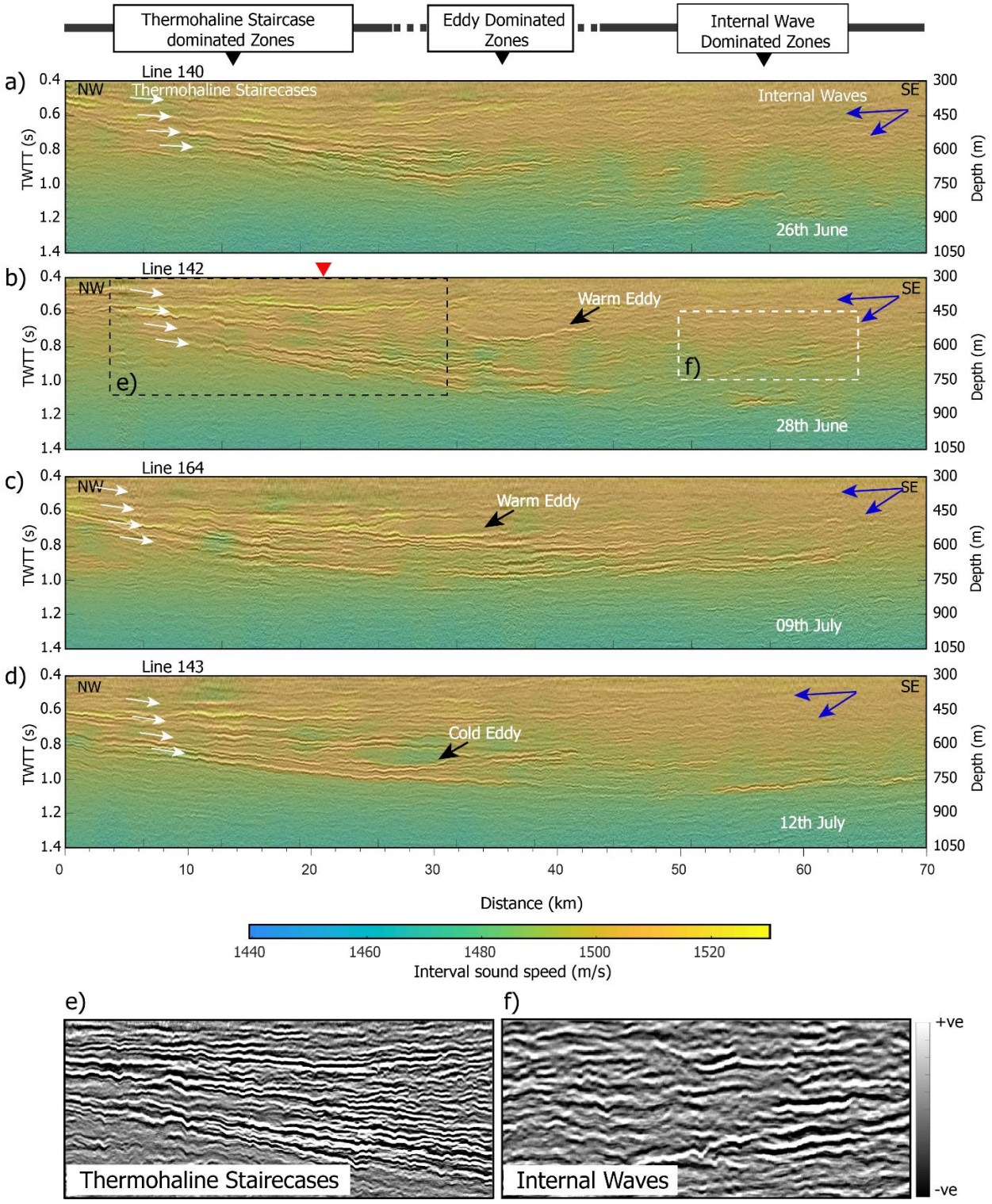

Figure caption was described in next page.

Figure 4.3. Interval sound speed models superimposed with seismic images display fine-scale thermohaline internal structure across the Kuroshio Current such as thermohaline staircases (white arrows), water eddies (black arrows), internal waves (blue arrows), and water mass boundaries, a) Line 140 exhibits no eddy, b) Line 142 contents a warm water core at 0.7s (~525m below sea surface), c) Line 164 also presents a warm water core at 0.6s (~450m below sea surface), d) Line 143 displays a cold water core at 0.9s (~625m below sea surface), e) An enlarged section from black dashed box in b) shows a reflection image of thermohaline staircases, f) An enlarged section from white dashed box in b) shows a reflection image of internal waves. A red inverted triangle in b) indicates the location of automatic sound speed analysis shown in Figure 4.2. The representative depth on the right side of the panels was calculated by assuming the uniform sound speed of 1500 m/s.

internal structure (Figure 4.3). On the other hand, with this quick processing, I processed these four individual pre-stack seismic data revealing sound speed variation through time in each line (Figure 4.3). High sound speed dominantly co-varies with the strong magnitude of seismic reflection amplitudes (Figure 4.3). Fine-scale thermohaline structure is clearly seen on the reflection profile in the northwestern and central part, which apparently dips to the southeastern part (Figure 4.3). Tsuji et al. (2005) presented this dipping fine structure by analysing the synthetic seismogram derived from *in situ* temperature and salinity measurement compared with seismic images to confirm fine structure reflectivity caused by salt-fingering double diffusion processes in the Kuroshio Current. This fine structure from our automatic sound speed analysis also presents continuous reflections over 40km, and in someplace, sub-horizontal, discontinuous reflections or undulations across the seismic profile in the Kuroshio Current as a result of lateral intrusion or double diffusive processes of different water masses between the warm Kuroshio Current in the uppermost part of seawater and colder water mass at greater depth (Figure 4.1 and 4.3). In addition, these continuous fine structure layers (white arrows, Figure 4.3) are dominant in the northwestern

and central sections of seismic survey lines perpendicular to Kuroshio Current whose current flow speed was fast within 1.0 - 1.5 m/s and also carried the warm water flows (Figure 4.1a,b,c, Japan Meteorological Agency, 2018). Southeastern section of seismic survey lines affected by slow flow speed of 0.5 – 1.0 m/s and less warm water current (less influenced by Kuroshio Current flow, white rectangular box in Figure 4.1). Accordingly, the internal fine structure across the southeastern sound speed profiles was dominant with low/discontinuous water reflectivity in the Kuroshio Current (blue arrows, Figure 4.3a,b,c,d,f). This implied that the water turbulent mixing process in the northwestern and central parts of seismic survey lines across the Kuroshio Current was more significant than the other area, and interestingly the water core ring reflective features dominantly occurred in this central part (black arrows, Figure 4.3b,c,d). The four profiles presented here (Figure 4.3) were recorded in proximity within 2.5 km and in four different times (Figure 4.3). A comparison of these seismic images reveals time-space variable characteristics, differencing internal structure, water core rings, and water mass boundaries. They also reflect non-identical core ring feature, and thermohaline staircases confined in the uppermost ocean layer 1000m which possesses different apparent dipping angle, continuity, and reflectivity corresponding to their energy reflected from strong thermohaline gradients (Figure 4.3). Although, all the profiles presented here were recorded in close locations with each other. They showed ocean fine structure differences of internal characteristics across Kuroshio Current, which were regarded as temporal rather than spatial variations (Tsuji et al. 2005).

However, undulating reflections are widespread in the profiles across the southeastern section of survey lines, which display low reflectance of amplitude and horizontally vary across the section (blue arrows, Figure 4.3a,b,c,d,f). Such features could be described due to the displacement of isopycnals by internal wave motion (Gorman et al. 2018; Holbrook and Fer 2005; Holbrook, Fer,

and Schmitt 2009). Vertical stacks of reflections with or without relatively apparent dip display laterally continuous reflections, and in someplace, sub-horizontal layers (white arrows, Figure 4.3a,b,c,e), which are so-called thermohaline staircases. These staircase layers were generated by double diffusive processes, salt fingering of adjacent water masses with temperature-salinity contrasts to form the dynamics of layer formation up to tens of kilometers (Holbrook et al. 2012; Tsuji et al. 2005; Gorman et al. 2018; Buffett et al. 2017; Radko 2003).

In three profiles (Lines 142, 164 and 143), I found the water core features of ocean reflection at different depths (black arrows, Figure 4.3). The water reflection vortex at line 142 represents the warm water core reflection within 29-42 km in the horizontal axis at 0.7 s (~525 m below sea surface) (black arrow, Figure 4.3b). Another warm core reflection existed in the line 164 within 25-35 km in the horizontal axis at 0.6 s (~450 m below sea surface) (black arrow, Figure 4.3c). Line 143 exhibits cold water vortex within 22-32 km in the horizontal axis at 0.9 s (~625 m below sea surface) (black arrow, Figure 4.3d). These results demonstrate the distinctive features in this region. The three eddy cores do not exhibit the typical eddy of strong circular reflection caused by strong acoustic impedance contrast. In addition, they display no internally strong reflectance regions (Gorman et al. 2018; Buffett et al. 2017; Papenberg et al. 2010). They are like bow-shaped reflective features. I can possibly interpret these bowl shaped structures due to the strong temperature/salinity gradient which caused the abrupt change of water mass movement between the warm water of eddy core and the underlying cold layer in Figure 4.3b,c, and between the cold water of eddy core and the underlying warm layer in Figure 4.3d (Buffett et al. 2017; Gorman et al. 2018; Yamashita et al. 2016). These eddies vary smaller in size and seismic characters compared to large eddies in other regions (Gorman et al. 2018; Buffett et al. 2017; Papenberg et al. 2010). The characteristics of their smaller size may be a result of their formation due to the

narrowing and constricted flow of the Kuroshio Current along the coast of southern Japan (Figure 4.1).

Remarkably, these distinctive oceanographic reflectors were acquired in close time in which the first two profiles in Figure 4.3a,b were in 2 days apart, and the last two profiles in Figure 4.3c,d were in 3 days apart, manifesting quite related reflective features in their close time acquisition, respectively. However, the first and the last two profiles were in time difference about two weeks apart which displayed much significant change of thermohaline internal structure.

4.3.2 Implications of oceanographic seismic and sound speed images

Corresponding to our extracted sound speed profiles from strong reflectance by automatic sound speed picking approach (Figure 4.3), I can clearly observe double diffusive processes or lateral intrusion or diapycnal mixing processes from sound speed variation (1480-1530 m/s), especially within our evidenced fine-scale thermohaline staircases at 0.4-1.1 s (300-825 m below sea surface). These variations of sound speed images in the Kuroshio Current provide implication of oceanic mixing and exchange processes and seismically mapped boundaries of deep water masses (Figure 4.3). The sound speed models presented here can be comparable to vertical variation sound speed profile converted from CTD (Conductivity, Temperature, and Depth) data acquired off the Ashizuri peninsula on 17 September 1994 (Tsuji et al. 2005). Dominantly, the strong reflection of fine structure co-varies with the high sound speed variation decreasing with depth (Figure 4.3). However, in relatively small scale, I observed the lateral variations of sound speed. This relatively small scale of fine structure in some areas varying with high/low or low/high sound speed contrasts (Figure 4.3) can be interpreted due to salt-fingering double diffusion where

two different water masses were strongly mixing in turbulent and diapycnal processes or possibly due to scattering phenomena of plankton blooms in the Kuroshio Current (Nakamura et al. 2006). Therefore, these processes caused the change in acoustic impedance contrasts (i.e. density x acoustic sound speed) resulted to low/high or high/low water reflectivity varying with sound speed contrasts in small scale area within our study intervals (Figure 4.3) (Nakamura et al. 2006; Papenberg et al. 2010; Dagnino et al. 2016; Buffett et al. 2017). These all results can represent how the seismic oceanography is considered as a sophisticated tool for the snapshot of oceanographic mixing processes or visualization of ocean flow model in approximate real time with high lateral variations (Gorman et al. 2018; Holbrook and Fer 2005; Holbrook, Fer, and Schmitt 2009). However, without *in situ* measurements, some local variation could include error (explanation in the next sub-title).

The closely spaced dense sampling (12.5m spacing) of seismic data in automatic sound speed analysis can provide us with high sensitivity and high lateral resolution compared to discrete data from hydrographic observations such as CTD or XBT (Expendable Bathythermograph) probes. The hydrographic observations are typically acquired over several hundred meters or kilometers apart, which can result to the loss of lateral resolution in details within the intermediate scales. The ability to create detailed images of fine-scale thermohaline structure, especially obtain time-space variant sound speed profile in the ocean using automatic sound speed analysis, represents a promising tool for studies of meso-scale oceanographic processes.

These seismic profiles were acquired in 1999. To improve our understanding of the Kuroshio Current system, further analyses or new measurements for validation of diapycnal mixing processes and transient heat uptake in the ocean are also required. It is essential to reproduce and compare these 1999 thermohaline fine structures profiles to the available seismic data acquired

over the years (till present time). Since 1993, there have been many seismic surveys acquired surrounding Japanese island to explore gas hydrate resources, researches in earthquake and volcanoes, and tectonic setting in Japan (Oyama and Masutani 2017). Therefore, one can benefit with these data to study internal fine structure of Kuroshio Current through years. This will help us understand in more comprehensive approach about Kuroshio Current thermohaline fine structure as well as visualization of ocean flow model which drastically changes in upstream/downstream current. In addition, I can observe how it has changed and influenced to ocean current in other regions and affect climate systems over the past time or possibly understand its current flow cycle. More importantly, it is possible if these investigations and understandings can be used to predict ocean circulation pattern in the future (Buffett and Carbonell, 2011), therefore, it is also important for ocean-climate model investigation.

4.3.3 Difficulty in accurate sound speed estimation

Seismic oceanography using the low-frequency acoustic reflection gives the result of relative changes in acoustic impedance, therefore it is difficult to estimate absolute value of physical with our inverse methods (Papenberg et al. 2010; Tang et al. 2016; Gorman et al. 2018). The small changes of sound speed of 15m/s and 2m/s is sensitive to the temperature changes of 3^{o}C and 0.4^{o}C, respectively (Holbrook et al. 2012). The obtained sound speed was produced from the automatic analysis of every picked 12.5 m spacing over 80 km laterally. Estimating the sound speed in accuracy of a few meters per second over the large scale in the ocean with the detail horizontal resolution can be difficult because of non-stationary aspect in ocean dynamics current and the chemical, physical, biological, and geological complexity of oceanographic processes (Holbrook et al. 2012). Even with the speedy processing of this analysis, I also struggle with some constraints

in this low-resolution reflection data in the water column such as applying smoothing in automatic sound speed analysis, non-uniqueness of deconvolution process, non-reflection above and below ocean fine structure layers, which produced inaccurate results of sound speed estimation. Another parameter is to set the optimum, sensitive and flexible picking in automatic velocity analysis in order to achieve the highest resolution for sound speed. Consequently, the resulting sound speed gives anomaly variation across the ocean which can be leading to an uninterpretable result. However, sound-speed variation of fine structure estimated here are concurrently with reflection amplitude magnitude of thermohaline staircases. Therefore, our results presented here can be used for semi-quantitatively investigating time-space variant thermohaline fine structure in the Kuroshio Current.

4.4 Conclusions

The seismic reflection technique using automatic sound speed analysis images variation of thermohaline fine structure within layers at least 10m thick and laterally continuous over several kilometers. Our seismic images present a whole view of different thermohaline features variation through time and space directly derived from advanced seismic velocity processing to reveal the ocean sound speed. Sound speed profiles vary concurrently, and seismic images present turbulent mixing, the presence of internal waves, thermohaline staircases, warm and cold water vortex, and the features of deep water mass boundaries across the Kuroshio Current. This automated technique of sound speed analysis with the dense lateral sampling of seismic data allows us a better understanding of numerous ocean processes through the entire water column with high lateral resolution. Therefore, mapping variant sound speed profiles in the Kuroshio Current simultaneously images over large sections of the ocean and time-lapse imaging without relying on

discrete data, which is a great interest of probing oceanographic processes with their space-time resolution.

4.5 References

Biescas, B., L. Armi, V. Sallarès, and E. Gràcia. 2010. Seismic Imaging of Staircase Layers below the Mediterranean Undercurrent. *Deep-Sea Research Part I: Oceanographic Research Papers* 57, no. 10: 1345–1353.

Bijma, J., H. O. Pörtner, C. Yesson, and A. D. Rogers. 2013. Climate Change and the Oceans - What Does the Future Hold?. *Marine Pollution Bulletin* 74, no. 2: 495-505.

Buffet, G. G., and R. Carbonell. 2011. Seismic Oceanography as a tool to monitor climate change. *EGU newsletter* 35.

Buffett, G. G., G. Krahmann, D. Klaeschen, K. Schroeder, V. Sallarès, C. Papenberg, C. R. Ranero, and N. Zitellini. 2017. Seismic Oceanography in the Tyrrhenian Sea: Thermohaline Staircases, Eddies, and Internal Waves. *Journal of Geophysical Research: Oceans* 122, no. 11:8503-8523.

Chhun, C., A. Kioka, J. Jia, and T. Tsuji. 2018. Characterization of Hydrate and Gas Reservoirs in Plate Convergent Margin by Applying Rock Physics to High-Resolution Seismic Velocity Model. *Marine and Petroleum Geology* 92: 719–732.

Claerbout, J. Jf, and S. Fomel. 2004. *Image Estimation by Example: Geophysical Soundings Image Construction: Multidimensional Autoregression*. Stanford University.

Dagnino, D., V. Sallarès, B. Biescas, and C. R. Ranero. 2016. Fine-Scale Thermohaline Ocean Structure Retrieved with 2-D Prestack Full-Waveform Inversion of Multichannel Seismic

Data: Application to the Gulf of Cadiz (SW Iberia). *Journal of Geophysical Research: Oceans* 121, no. 8: 5452-5469.

Deng, P., Y. Chen, Y. Zhang, and H. W. Zhou. 2016. Weighted Stacking of Seismic AVO Data Using Hybrid AB Semblance and Local Similarity. *Journal of Geophysics and Engineering* 13, no. 2: 152-163.

Dix, C. H. 2002. Seismic Velocities From Surface Measurements. *Geophysics* 20, no. 1: 68–86.

Fomel, S. 2009. Velocity Analysis Using AB Semblance. *Geophysical Prospecting* 57, no. 3: 311–321.

Fomel, S., and E. Landa. 2014. Structural Uncertainty of Time-Migrated Seismic Images. *Journal of Applied Geophysics* 101: 27–30.

Fortin, W. F. J., and W. S. Holbrook. 2009. Sound Speed Requirements for Optimal Imaging of Seismic Oceanography Data. *Geophysical Research Letters* 36, no. 24.

Gorman, A. R., M. W. Smillie, J. K. Cooper, M. H. Bowman, R. Vennell, W. S. Holbrook, and R. Frew. 2018. Seismic Characterization of Oceanic Water Masses, Water Mass Boundaries, and Mesoscale Eddies SE of New Zealand. *Journal of Geophysical Research: Oceans* 123, no. 2: 1519–1532.

Holbrook, W. S., and I. Fer. 2005. Ocean Internal Wave Spectra Inferred from Seismic Reflection Transects. *Geophysical Research Letters* 32, no. 15.

Holbrook, W. S., I. Fer, and R. W. Schmitt. 2009. Images of Internal Tides near the Norwegian Continental Slope. *Geophysical Research Letters* 36, no. 24.

Holbrook, W. S., V. Marcon, A. R. Bacon, S. L. Brantley, B. J. Carr, B. A. Flinch, D. D. Richter, and C. S. Riebe. 2019. Links between Physical and Chemical Weathering Inferred from a 65-m-Deep Borehole through Earth ' s Critical Zone. *Scientific reports* 9, no. 1: 4495.

Holbrook, W. S., P. Páramo, S. Pearse, R. W. Schmitt, and P. Paramo. 2012. Thermohatine an Fine Structure Front from in Oceanographic Seismic Reflection Profiling. *Science* 301, no. 5634: 821–824.

Japan Meteorological Agency, (2018). The speed of current flow in the Kuroshio Region, Japan. Retrieved 20 September 2018, from https://www.data.jma.go.jp/gmd/kaiyou/data/db/kaikyo/jun/current_HQ.html?areano=2

Lee, J. H., and K. J. Richards. 2004. The Three-Dimensional Structure of the Interleaving Layers in the Western Equatorial Pacific Ocean. *Geophysical Research Letters* 31, no. 7.

Li, X., Y. Liu, Y. C. Hsin, W. Liu, Z. Shi, H. C. Chiang, and C. C. Shen. 2017. Coral Record of Variability in the Upstream Kuroshio Current during 1953–2004. *Journal of Geophysical Research: Oceans* 122, no. 8: 6936–6946.

Marshall, D. P., and L. Zanna. 2014. A Conceptual Model of Ocean Heat Uptake under Climate Change. *Journal of Climate* 27, no. 22: 8444–8465.

Minato, S., T. Tsuji, T. Noguchi, K. Shiraishi, T. Matsuoka, Y. Fukao, and Gregory M. 2009. Estimation of Detailed Temperature Distribution of Sea Water Using Seismic Oceanography. *Butsuri-tansa* 62, no. 5: 509–520.

Moore, G. F., et al. 2001. *Proceedings of the Ocean Drilling Program*, Initial Reports, 190, [CD-ROM], Ocean Drill. Program, College Station, Tex.

Nagai, T., G. S. Durán, D. A. Otero, Y. Mori, N. Yoshie, K. Ohgi, D. Hasegawa, A. Nishina, and T. Kobari. 2019. How the Kuroshio Current Delivers Nutrients to Sunlit Layers on the Continental Shelves with Aid of Near-inertial Waves and Turbulence. *Geophysical Research Letters*.

Nagai, T., A. Tandon, E. Kunze, and A. Mahadevan. 2015. Spontaneous Generation of Near-

Inertial Waves by the Kuroshio Front. *Journal of Physical Oceanography* 45, no. 9: 2381–2406.

Nagai, T., A. Tandon, H. Yamazaki, and M. J. Doubell. 2009. Evidence of Enhanced Turbulent Dissipation in the Frontogenetic Kuroshio Front Thermocline. *Geophysical Research Letters* 36, no. 12.

Nagai, T., A. Tandon, H. Yamazaki, M. J. Doubell, and S. Gallager. 2012. Direct Observations of Microscale Turbulence and Thermohaline Structure in the Kuroshio Front. *Journal of Geophysical Research: Oceans* 117, no. C8.

Nakamura, Y., T. Noguchi, T. Tsuji, S. Itoh, H. Niino, and T. Matsuoka. 2006. Simultaneous Seismic Reflection and Physical Oceanographic Observations of Oceanic Fine Structure in the Kuroshio Extension Front. *Geophysical Research Letters* 33, no. 23.

Nandi, P., W. S. Holbrook, S. Pearse, P. Páramo, and R. W. Schmitt. 2004. Seismic Reflection Imaging of Water Mass Boundaries in the Norwegian Sea. *Geophysical Research Letters* 31, no. 23.

National Ocean Service, (2018). How does climate change affect coral reefs? Retrieved 09 February 2019, from https://oceanservice.noaa.gov/facts/coralreef-climate.html

Oyama, A., and S. Masutani. 2017. A Review of the Methane Hydrate Program in Japan. *Energies* 10, no. 10: 1447.

Papenberg, C., D. Klaeschen, G. Krahmann, and R. W. Hobbs. 2010. Ocean Temperature and Salinity Inverted from Combined Hydrographic and Seismic Data. *Geophysical Research Letters* 37, no. 4.

Páramo, P., and W. S. Holbrook. 2005. Temperature Contrasts in the Water Column Inferred from Amplitude- versus-Offset Analysis of Acoustic Reflections. *Geophysical Research Letters*

32, no. 24.

Radko, T. 2003. A Mechanism for Layer Formation in a Double-Diffusive Fluid. *Journal of Fluid Mechanics* 497, no. 497: 365–380.

Resplandy, L., R. F. Keeling, Y. Eddebbar, M. K. Brooks, R. Wang, L. Bopp, M. C. Long, J. P. Dunne, W. Koeve, and A. Oschlies. 2018. Quantification of Ocean Heat Uptake from Changes in Atmospheric O_2 and CO_2 Composition. *Nature* 563, no. 7729: 105.

Sallares, V., R. W. Hobbs, D. Klaeschen, C. Ranero, C. Hurich, E. Vsemirnova, and G. G. Buffett. 2013. Characterization of Thermohaline Staircases in the Tyrrhenian Sea Using Stochastic Heterogeneity Mapping. *The Journal of the Acoustical Society of America* 133, no. 5: 3313–3313.

Sheen, K. L., N. J. White, C. P. Caulfield, and R. W. Hobbs. 2012. Seismic Imaging of a Large Horizontal Vortex at Abyssal Depths beneath the Sub-Antarctic Front. *Nature Geoscience* 5, no. 8: 542.

Stranne, C., L. Mayer, T. C. Weber, B. R. Ruddick, M. Jakobsson, K. Jerram, E. Weidner, J. Nilsson, and K. Gårdfeldt. 2017. Acoustic Mapping of Thermohaline Staircases in the Arctic Ocean. *Scientific Reports* 7, no. 1: 15192.

Tang, Q., R. Hobbs, C. Zheng, B. Biescas, and C. Caiado. 2016. Markov Chain Monte Carlo Inversion of Temperature and Salinity Structure of an Internal Solitary Wave Packet from Marine Seismic Data. *Journal of Geophysical Research: Oceans* 121, no. 6: 3692-3709.

Tsuji, T., T. Noguchi, H. Niino, T. Matsuoka, Y. Nakamura, H. Tokuyama, S. Kuramoto, and N. Bangs. 2005. Two-Dimensional Mapping of Fine Structures in the Kuroshio Current Using Seismic Reflection Data. *Geophysical Research Letters* 32, no. 14.

Wood, W. T., W. S. Holbrook, M. K. Sen, and P. L. Stoffa. 2008. Full Waveform Inversion of

Reflection Seismic Data for Ocean Temperature Profiles. *Geophysical Research Letters* 35, no. 4.

Yamashita, M., Y. Fukao, K. Hasumi, S. Miura, and S. Kodaira. 2016. Reflection Imaging of Oceanic Fine Structure under Strong Ocean Current in the Izu-Ogasawara Region. Paper presented at the 12th SEGJ International Symposium, November 18-20, in Tokyo, Japan.

Zhu, K. L., X. Chen, K. F. Mao, D. Hu, S. Hong, and Y. Li. 2019. Mixing Characteristics of the Subarctic Front in the Kuroshio-Oyashio Confluence Region. *Oceanologia* 61, no. 1: 103–13.

Chapter 5

Conclusions

5.1 Conclusions

The combination technique of advanced seismic data processing (i.e automatic velocity analysis), simultaneous waveform analysis (i.e pre-stack seismic inversion), and rock physics approach provides the new approach and innovative technique to overcome the exploration technical challenges for successfully and effectively mapping complex gas hydrocarbon system and complicated structure & stratigraphy change in Kumano forearc basin formation and configuration. Key findings and research outcomes in this PhD dissertation are recapped as follows.

Chapter 2 provides new insights of geological processes and intensive tectonism which influences to hydrate and gas reservoir in the Kumano forearc basin. Integration of automatic velocity analysis and rock physics approach advances effective and accurate resource quantification, which is beneficial for exploration techniques as well as minimizing uncertainties

and risks related to upstream Oil&Gas activities. On the other hand, these techniques can be considered a potential solution for hydrocarbon gas quantification in the deep water reservoirs and, additionally applicable to other plate convergent margins. This research is significant for future energy supply, climate change (i.e methane hydrate dissolved and leaked to the seafloor), and prospective & safe reservoirs for CO_2 storage in the future.

Chapter 3 using integrated automatic velocity analysis, pre-stack wave form inversion and rock physics provide an innovative exploration approach to estimate pore pressure distribution and separate pore pressure and fluid saturation effects in the complicated gas hydrocarbon accumulations of the deep water basin. In addition, pore pressure prediction in this study can allow us to elucidate the hydrate and gas formation, deformation mechanism, and their geological process in this basin controlled by the intensive tectonic movement in this plate convergent.

Chapter 4 using the innovative technique of automatic seismic velocity analysis, I can map ocean thermohaline internal structure and sound speed variation in the Kuroshio Current. Therefore, mapping variant sound speed profiles in the Kuroshio Current simultaneously images over large sections of the ocean and time-lapse imaging without relying on discrete data, which is a great interest of probing oceanographic processes with their space-time resolution over large-scale ocean current as well as investigation of ocean-climate systems.

Overall, the strategies and approaches presented in this dissertation provide a wide range of analytical, effective, and faster tools and solutions to deal with the technical challenges for better characterization and imaging of the earth's resources and their geological processes as well as application for the study of oceanographic processes which strongly influence to ocean current and climate systems.

Acknowledgments

Three year PhD study and life at Kyushu University, Japan, have been a prestigious period in my life and a truly life-changing experience for me. Words cannot be expressed enough or in details here to people who earn my gratitude for their contribution to my PhD time. However, I would like to express my gratitude to the following incredible people.

First and foremost, I would like to express my sincere and heartfelt gratitude to my advisor, Prof. Takeshi Tsuji, for being an excellent advisor and a role model for students/scientists. Under his supervision, I have enormously benefited from his comprehensive & wide-ranging research, skills & research projects, new & innovative research ideas and insightful discussions, and I also greatly appreciate his encouragement, kindness, endless support and help. Prof. Tsuji has also inspired me by his hardworking, close supervision, and research passionate attitude which leads me to become the kind of research scientist I am today. I am more than lucky to have a such outstanding advisor.

Besides my advisor, I would like to deeply thank Assistant Prof. Tatsunori Ikeda, Assistant Prof. Jihui Jia, and Assistant Prof. Arata Kioka for their scientific advice, knowledge and many insightful discussions, ideas, and suggestions during my PhD study. Their contribution really improved and helped my research skills and achievements. I really enjoyed, gained knowledge, and solved my research problems during discussion with them.

Especially, I gratefully acknowledge for the scholarship program of ASEAN University Network/Southeast Asia Engineering Education Development Network (AUN/SEED-Net) for supporting my three-year PhD study at Kyushu University. I am also indebted to all lecturers and Dr. Nallis Kry, a head of the Faculty of Geo-resources and Geotechnical Engineering, Institute of Technology of Cambodia, Cambodia, who have given me the constant support and guidance for my PhD at Kyushu University. A special appreciation also goes to Prof. Koichiro Watanabe who gave me support, guidance and discussion about my future PhD direction which led me to have Prof. Tsuji as my PhD advisor at Kyushu University. *Many thanks again, Prof. Watanabe!*

I am greatly thankful to the research support staff, Ms. Tomomi Yamaguchi for her support, assistance, English-Japanese translation and her speedy working to process any of my related documents. It is really joyful and fun to work with her.

My deep appreciation also goes out to my all foreign and Japanese fellow labmates who have been very good for me. It is really exciting and fun to work and around them. They support and provide me with the happy, helpful, hard-working, friendly, warm and comfortable environment in the lab.

In chapter 2 and 3, I would like to thank the Japan Agency for Marine-Earth Science and Technology (JAMSTEC) for providing 3D seismic data. The chapter 2 research was supported by the Japan Society for the Promotion of Science (JSPS) through a Grant-in-Aid for Scientific Research on Innovative Areas (no. JP17H05318), a Grant-in-Aid for Scientific Research (S) (no. JP15H05717), and a Grant-in-Aid for Science Research B (No. JP15H02988). In chapter 4, I am grateful to N. Bangs, T. Shipley, S. Gulick, G. Moore and S. Kuramoto for their efforts with the acquisition of seismic data, and M. Kawabe for Conductivity, Temperature and Density (CTD)

data. I also fully acknowledge Marine Geoscience Data System (MGDS) for open access data (http://wwwudc.ig.utexas.edu/sdc/).

Truly and wholeheartedly, I would like to dedicate this PhD dissertation to my late grandparents and my late father who gave me strength, happiness, and made me a happy and good person to live in this world. I also would like to devote all of my PhD achievements to my beloved mother, sisters and brothers who have given me unconditional love, countless support, and spiritual motivation. They are always with me and stand by me throughout my life ups and downs.

CHHUN CHANMALY

(ឈុន ចាន់ម៉ាលី)